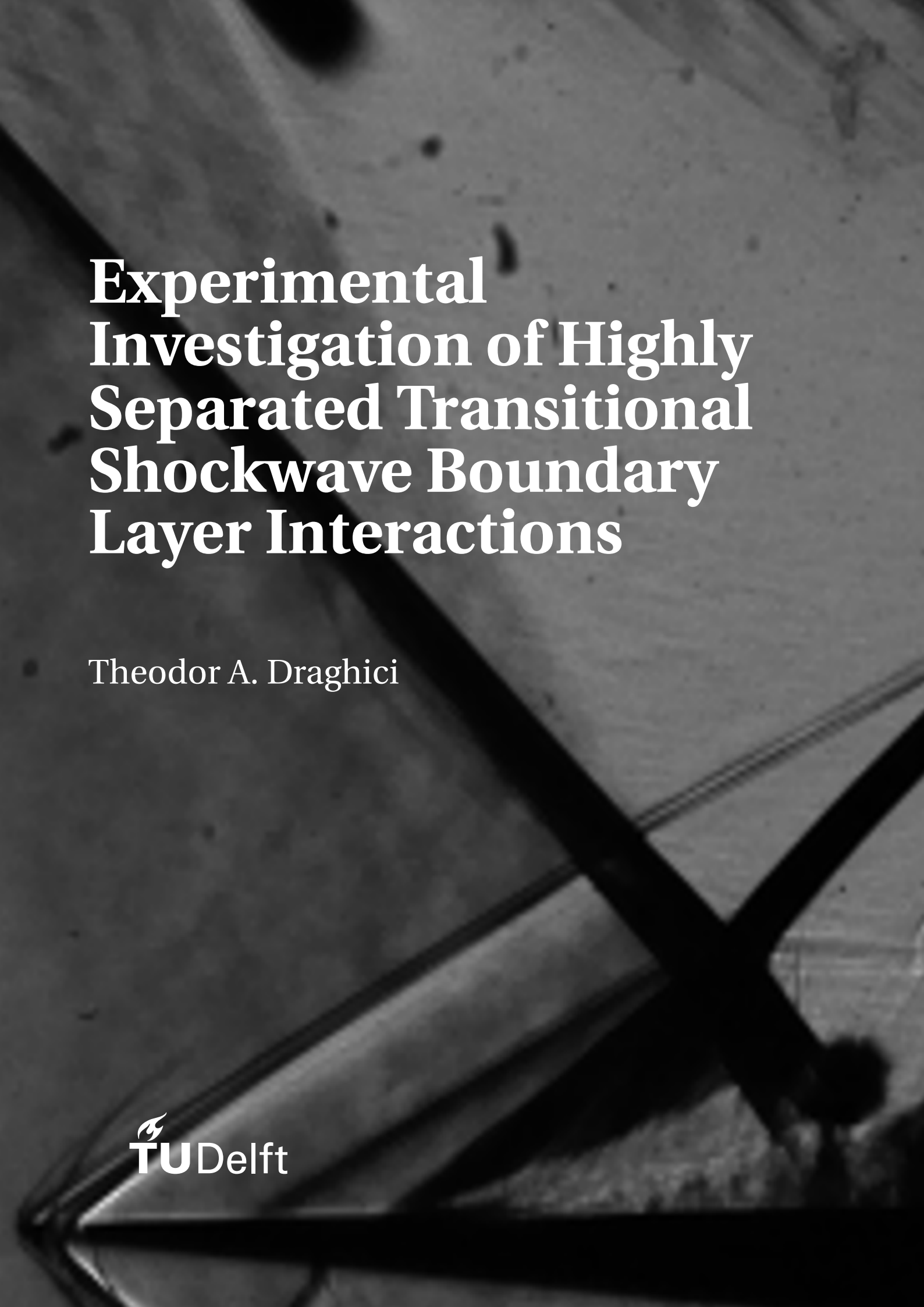

Experimental Investigation of Highly Separated Transitional Shockwave Boundary Layer Interactions

Theodor A. Draghici

TU Delft

DELFT UNIVERSITY OF TECHNOLOGY

MASTER OF SCIENCE THESIS

Experimental Investigation of Highly Separated Transitional Shockwave Boundary Layer Interactions

by

Theodor A. Draghici

to obtain the degree of Master of Science
at the Delft University of Technology,
to be defended publicly on the 3rd of June 2025 at 09:00

Student number:	5686318	
Project duration:	15 January 2024 - 03 June 2025	
Assessment Committee:	Dr. ir. B.W. van Oudheusden	TU Delft, chair
	Dr. ir. F.F.J. Schrijer	TU Delft, daily supervisor
	Prof. Dr. S. Hickel	TU Delft, external examiner
	Dr. S.J. Hulshoff	TU Delft, external member
Faculty:	Aerospace Engineering	

TU Delft Delft University of Technology

Preface

"If you're the smartest person in your class, then you're in the wrong class." I can't precisely recall where I first heard this quote or from whom, but it has stuck with me ever since and has remained a guiding principle throughout my life.

When I arrived at TU Delft in 2022, coming from the Polytechnic University of Bucharest where I graduated as valedictorian, I sought a challenging new environment that would push my boundaries. Delft presented exactly that: a demanding, competitive atmosphere known worldwide for its academic rigor, but equally celebrated for its excellence and innovation. The journey has not been without its challenges, yet every step has been profoundly rewarding and deeply enriching.

Throughout this experience, I have had the privilege of working alongside professional, kind, and incredibly supportive individuals. From my fellow students and Professors to the faculty administration, everyone I encountered has shown patience, clarity in their explanations, and genuine care for my learning and personal growth. Their guidance has been both humbling and inspiring, and I leave Delft equipped not only with invaluable academic knowledge, but also life lessons that will stay with me forever.

I would like to express my deepest gratitude to Dr. ir. F.F.J. Schrijer and Dr. ir. B.W. van Oudheusden (Ferry and Bas!) for their unwavering support throughout the months of my thesis work, as well as the months when we collaborated during our faculty courses. Although the path was occasionally challenging and required more patience than expected, their understanding, encouragement, and constant availability to help ensured that I could complete my research successfully and without any pressure. I sincerely hope our paths cross again in future collaborations. My gratitude is also extended to Philipp Nel, the doctoral student who helped me with the experiments and who also gave me a starting point for the thesis.

To my friends, both from home and those I've met here (Georgia and Pin), you have made this journey a much better experience. Special thanks go to my best friend, Dan, who has always been there to lift my spirits, encourage me, and help me overcome every obstacle with a smile.

Lastly, and most importantly, to my mom, dad, and sister, you are my greatest strength. Your unwavering support and love throughout my time not just at Delft, but always, have carried me through every challenge. I hope that the outcome of this journey has brought you not only pride but also joy, satisfaction, and the fulfillment of knowing that your trust and encouragement have made all the difference.

Theodor A. Draghici
Delft, June 2025

Abstract

The present Master's thesis investigated the low-frequency unsteadiness characteristic of highly separated transitional oblique shock wave-boundary layer interactions (hereinafter "OSBLIs"). Such phenomena, encountered notably in engine components operating at transitional Reynolds numbers, are relevant due to their impact on aerodynamic efficiency, structural integrity, and system reliability. The primary research question examined how variations in different parameters such as Mach number, Reynolds number (Re_x), and inviscid pressure jump influence a low-frequency shock oscillation mechanism which was previously identified in literature. To this end, experimental studies were conducted in the TST-27 transonic-supersonic wind tunnel at TU Delft, using high-speed and spark-light Schlieren visualizations capture the relevant flow phenomena. These recordings were processed using digital and spectral analysis.

The findings from this study revealed that the investigated transitional OSBLIs exhibited low-frequency shock oscillations strongly correlated with the periodic formation and disappearance of a Mach stem, which was denoted as the "dual domain" phenomenon. Through carefully chosen variations in Mach number and Reynolds number, it was shown that slight adjustments significantly impacted both the presence of the dual domain and the characteristics of the shock oscillations. Moreover, the Reynolds number regime identified as transitional for the natural flat plate boundary layer in previous research was validated.

Another aspect of this thesis involved the implementation of passive flow control techniques, specifically the introduction of thin two-dimensional steps (in height increments of 60 microns) designed to artificially trip the boundary layer. The experimental results demonstrated that even minimal boundary layer tripping significantly dampened the shock oscillations and modified the interaction dynamics of cases where the oscillation mechanism had previously clearly been identified. The frequency analysis confirmed this, as none of the oscillation peaks which had previously been identified were observed when tripping the boundary layer.

A non-dimensional analysis of the dominant oscillation frequencies indicated a consistent Strouhal number convergence around St = 0.33, particularly in cases where the "dual-domain" behavior and high oscillation amplitudes were observed. An increase in the Reynolds number consistently resulted in reduced laminar separation amplitudes and increased oscillation frequencies, which aligned with the theoretical expectations of accelerated boundary-layer transition dynamics.

In conclusion, this study was successful in identifying the main parameters that cause unsteadiness in transitional OSBLIs. It confirmed the existing transitional Reynolds number ranges which had previously been analyzed in the context of weak OSBLIs and the natural boundary layer of the flat plate which was used, and showed that even simple flow control methods with low 2D step heights can effectively reduce shock oscillations. Additionally, a meaningful non-dimensional scaling was done, which can aid in further research and comparison of the phenomena which were investigated in the present thesis. These findings provide a solid basis for future studies aiming to apply this knowledge to more general cases and improve the prediction and design of aerospace components affected by transitional shock-induced boundary-layer interactions.

Contents

List of Figures

List of Tables

Nomenclature

Abbreviations

Abbreviation	Definition
CFD	Computational Fluid Dynamics
FFT	Fast Fourier Transform
LE	Leading Edge
PIV	Particle Image Velocimetry
PSD	Power Spectral Density
OSBLI	Oblique Shockwave Boundary Layer Interaction
S(W)BLI	Shock(wave) Boundary Layer Interaction
TE	Trailing Edge
UHF	Ultra-high Frequency

Symbols

Symbol	Definition	Unit
K	Gladstone–Dale constant	[m^3/kg], [-]
L_{int}/L_i	Interaction length	[m]
Ma	Mach number	[-]
Re_x/Re	Reynolds number	[-]
St	Strouhal number	[-]
T/T_t	Static temperature / Total temperature	[K]
a	Speed of sound	[m/s]
f	Frequency	[Hz], [s^{-1}]
n	Refractive index	[-]
p/p_t	Static pressure / Total pressure	[Pa]
U/U_∞	Streamwise velocity / Freestream velocity	[m/s]
x	Streamwise direction	[m]
y	Wall-normal direction	[m]
Δ	Difference between two quantities	[m]
β	Shockwave angle	[°]
γ	Specific heats ratio	[-]
δ	Boundary layer thickness	[m]
θ	Flow deflection angle	[°]
μ	Dynamic viscosity	[Pa·s]
ν	Kinematic viscosity	[m^2/s]
ρ	Density	[kg/m^3]
σ	Standard deviation	[-]

Chapter 1

Introduction

1.1 Motivation

Shock wave-boundary layer interactions (commonly abbreviated as "SBLIs") are critical aerodynamics phenomena common across various high-speed flows in aerospace engineering. As described by Babinsky & Harvey [1], these interactions take place when a shock wave—a flow discontinuity marked by an abrupt rise in pressure, temperature, and density—encounters the boundary layer of a component (such as a flight surface) in a high-speed flow. SBLIs can lead to complex flow behaviors, including flow separation, shock oscillations, and significant changes in aerodynamic performance. SBLIs become particularly interesting in aerodynamic studies when they lead to the separation of the boundary layer. This separation can lead to loss of control authority; furthermore, the unsteadiness of the interactions can couple into the resonant frequencies of the aircraft panels (i.e., the panels may exhibit a higher vibratory response to the forcing caused by the unsteady motions), ultimately leading to their structural fatigue. A reference example of how SBLIs can severely affect the structural integrity of aircraft components is the North American X-15. During the 1960s, a "dummy scramjet" installation was tested in flight at Ma = 6.7 (Figure 1.1).

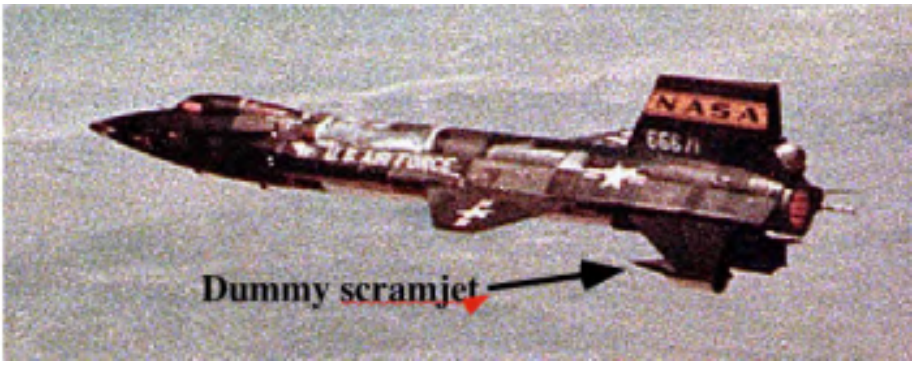

Figure 1.1: North American X-15A-2 with Ramjet [1]

Due to the shockwave boundary layer interactions occurring at the corner of the supporting pylon, extreme heat fluxes led to structural failure of the panel holding the ramjet (Figure 1.2a), with the ramjet itself falling off in flight. So-called "blunt fin SBLIs" such as around ultra-high frequency (UHF) antennas of aircraft in supersonic flight can also lead to their aerothermal heating and damage (Figure 1.2b) (NB: the aerothermal heating which is visible in this figure is not just due to the "mean" heating produced by the flow, but also because of the unsteadiness of the SBLI). It becomes apparent that SBLIs play an essential role in aircraft design in transonic and supersonic flow regimes.

[1] https://space.skyrocket.de/doc_lau_det/x15a2.htm

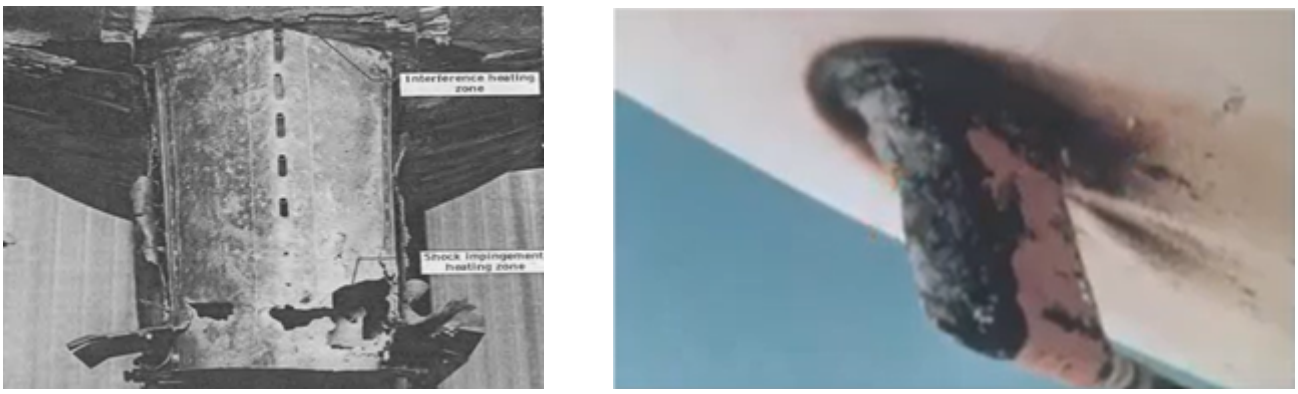

(a) front view of the panel holding the dummy pylon **(b)** aerothermal heating of UHF Antenna (blunt fin SBLI)

Figure 1.2: Outcome of the SBLI for components of the X-15 during flight at M = 6.7 (Watts [2])

While these striking examples of damage on the X-15 underscore the severe consequences of unmitigated shock wave-boundary layer interactions, this thesis specifically addresses the transitional form of SBLIs that occur at lower Reynolds numbers—conditions frequently encountered in engine compressors, turbines, and fans operating at higher altitude (and thus at lower Reynolds numbers). Such an example of SBLI occurring within a compressor cascade is depicted in Figure 1.3.

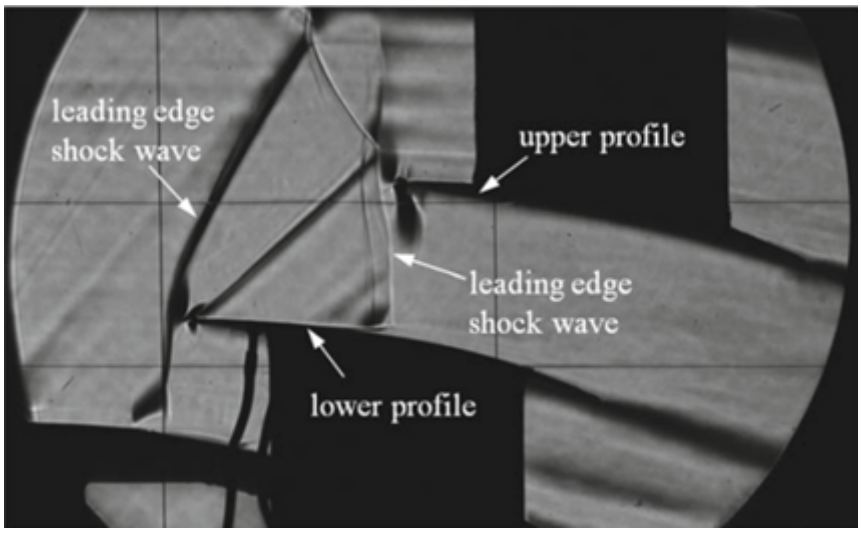

Figure 1.3: SBLI occurring in an engine compressor/fan flow (Doerffer et al. [3])

In these conditions, the boundary layer may transition from laminar to turbulent within the region of the shock interaction, generating a host of unique flow features not seen in "purely" turbulent or laminar SBLIs. Although less visually dramatic than the panel disintegration of the X-15 at Mach 6.7 presented before, these transitional SBLIs can critically affect performance and durability by inducing flow separation, unsteadiness, and significant losses in aerodynamic efficiency; the research supporting these arguments will represent the objective of the Literature Review.

According to Babinsky & Harvey [1], the general importance of understanding SBLIs lies in their impact on the aerodynamic efficiency and stability of these systems. Apart from potentially leading to structural damage, as seen before, the authors also mention that SBLIs can induce substantial drag increase, lift reduction, and flow unsteadiness. They are, therefore, critical in the design and operation of components such as engine fans, turbines, and compressors, where maintaining stable flow is a priority.

The authors distinguish five basic SBLIs that can occur in two-dimensional flows: impinging oblique-shock reflection (also called OSBLI), ramp flow, standard shock, imposed pressure jump, and oblique shock induced by a forward-facing step. Each type has distinct characteristics and effects on the boundary layer. As their name suggests, oblique shockwave boundary layer interactions (OSBLIs) occur when an oblique

shock wave impinges on the boundary layer of a surface. This interaction is expected in supersonic inlets and around aerodynamic surfaces like wings and turbine blades (Babinsky &Harvey [1]).

The scope of this Master's thesis will include the first case, namely impinging oblique-shock boundary layer interactions (or oblique shockwave-boundary layer Interactions). In their book, Babinsky & Harvey explain that, when an oblique shock wave interacts with the boundary layer, it can cause the boundary layer to thicken or even separate from the surface. If the flow reattaches further downstream, it creates a so-called "separation bubble"; however, if the interaction is strong enough, the impinging shock can cause total boundary layer separation. OSBLIs can induce low-frequency oscillations in the shock wave, commonly called "shock breathing" or "shock oscillation."

Figure 1.4 illustrates a schematic for a typical OSBLI scenario where an oblique shock impinges on a boundary layer, causing the separation bubble mentioned before. This figure highlights that the boundary layer separates ahead of the impinging shock C1 (what will later be referred to as the "upstream influence"). The separation generates compression waves which "smear out" the reflected shockwave C2 as it enters the shear layer; these smeared-out compression waves emanate from the "sonic line" (the dash-dotted line denoted by M=1 in Figure 1.4). A fan of expansion waves forms when the separated region height starts to lower, and the separation bubble terminates with a "reattachment shockwave" which forms due to the flow being compressed once more.

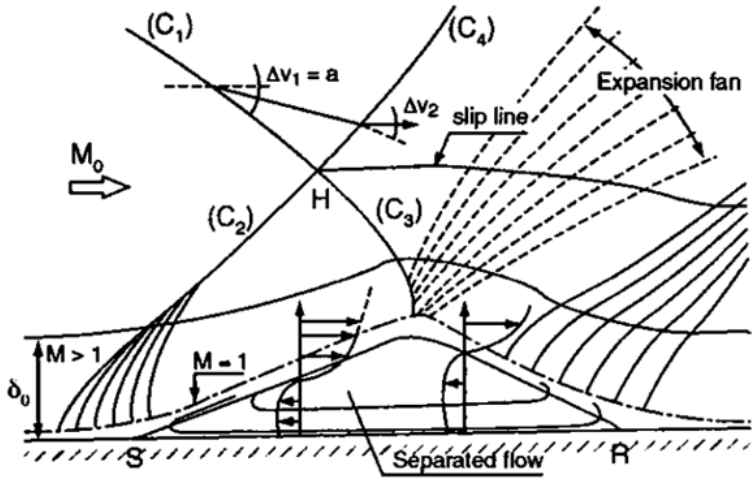

Figure 1.4: Schematic of an Oblique SBLI (Babinsky & Harvey [1])

Because OSBLIs require these impinging shockwaves to appear from "above" the surface with the developing boundary layer (as seen in Figure 1.4), transonic and supersonic flows which involve aerodynamic elements positioned one above the other appear of interest; engine compressors, supersonic engine intakes, engine turbines, and engine fans all fit these criteria. If the interactions are not adequately managed, they can lead to flow separation, increased drag, loss of efficiency, and even mechanical failure. For example, in compressors, OSBLIs can cause surge and stall, leading to catastrophic engine failure. In turbine blades, improper handling of SBLIs can result in blade flutter, fatigue, and damage (Babinsky & Harvey [1]).

Moving the discussion towards a more practical application, it is known that supersonic air-breathing propulsion systems rely on efficient inlet designs that achieve rapid flow deceleration and compression with minimal total pressure loss. One effective approach, known as mixed-compression inlets, combines internal and external compression by employing multiple oblique shocks to compress the oncoming supersonic flow. In doing so, the inlet can capture the necessary airflow "with the least possible loss in total pressure or head, with the best attainable flow distribution, and with the least amount of aircraft drag" (Surber & Tinapple [4]). However, these internal shock reflections inevitably impinge on the internal inlet walls, creating multiple OSBLIs. If unmanaged, such interactions can provoke large flow separation regions,

unsteady shock behavior, and high thermal loads. A similar example to this is found in Babinsky & Harvey [1], where an internal compression inlet with oblique shockwaves forming within it, Figure 1.5.

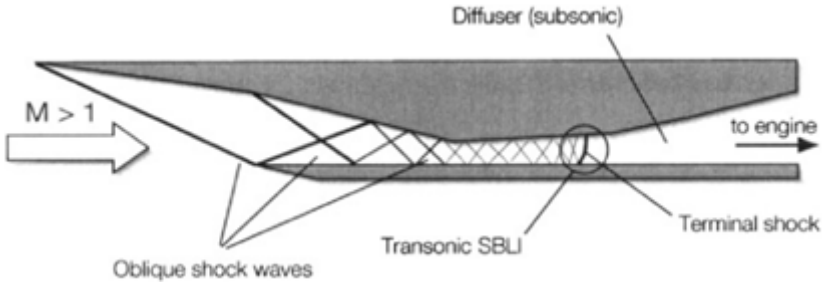

Figure 1.5: Internal compression inlet with OSBLIs (Babinsky & Harvey [1])

In practical aerospace applications, OSBLIs occur notably in systems with supersonic or hypersonic airflow. Examples include supersonic engine intakes, where OSBLIs help decelerate and compress the air before it enters the engine, or in missile systems where shock-induced separation is controlled using techniques such as plasma actuators (Webb et al. [5]). The main difficulties of OSBLIs at supersonic or hypersonic conditions are associated with the unstart of the engines due to aerodynamic blockage, and the intense mean heating (in hypersonic cases) coupled with the unsteadiness of SBLIs which in turn may result in component failure (recall the X-15 experiment depicted in Figure 1.2).

However, the purpose of studying OSBLIs in this thesis is not solely to focus on these high-speed applications. Instead, the aim is to also link the physical phenomena observed in oblique SBLIs to those occurring in transonic compressor cascades, where passage shocks interact with boundary layers at transonic speeds. For this reason, an introduction of transonic SBLIs and their characteristics will serve as the foundation for the following sections.

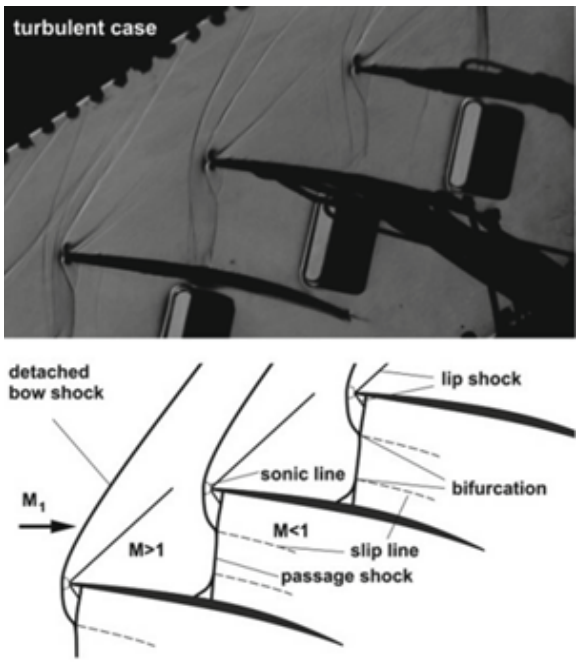

Figure 1.6: Supersonic flow over compressor cascades illustrating the OSBLI (Doerffer et al. [3])

The situation depicted in Figure 1.6 represents a particular case of compressor cascade flow with a transonic SBLI caused by the passage shock. Notice the lambda shock-foot configuration, which is similar to the close-up drawing of the interaction from Figure 1.5. This “passage shock” forms due to the acceleration of airflow within the blade passages to supersonic speeds (Doerffer et al. [3]), much like the mechanism on the suction side of airfoils described by Babinsky and Harvey [1]. They add that the strength of the passage shock is influenced by factors such as blade geometry, inlet Mach number, and blade loading; greater

curvature, higher Mach numbers, and increased loading expand the supersonic region and intensify the shock wave.

The bow shock formed at the leading edge of the blade influences this mechanism by altering the upstream flow conditions, potentially strengthening the passage shock and intensifying its interaction with the boundary layer. This compounded effect can lead to increased total pressure losses and affect the overall efficiency of the compressor system, as explained by Cumpsty [6].

In engine flows, whether it be fans, compressors or turbines, there are typically three scenarios involving supersonic flow over cascades, descrbied by Doerffer et al [3] and Nel et al. [7]:

- Detached shock with subsonic flow: a bow shock forms ahead of the leading edge, creating directly subsonic flow after the shock. This leads to minimal flow separation. The bow shock will likely oscillate around the leading edge, indicating an unsteady behavior.
- Lambda passage shock: by reducing the back pressure, a supersonic leading edge shockwave forms, which remains steady. This scenario is characterized by significant flow separation and is the primary case of interest.
- Swallowed passage shock: a further reduction in back pressure results in a smaller separation compared to the lambda passage shock case.

Denton [8] illustrates this mechanism in Figure 1.7, which shows shock patterns near the tip of a typical transonic compressor.

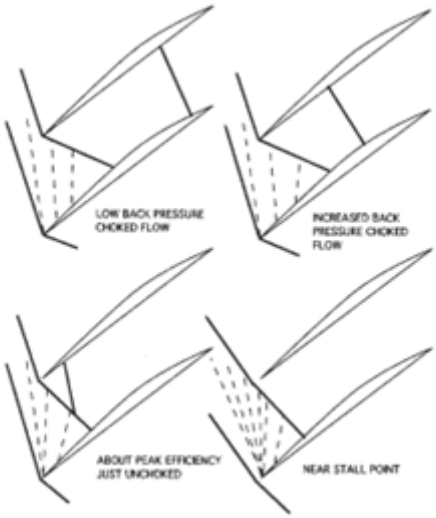

Figure 1.7: Common shock structures for transonic compressors (Denton [8])

Business jets and defense aircraft tend to fly at higher altitudes with lower air density, as explained in the research of Nel et al. [9]. These conditions often lead to the persistence of a laminar boundary layer on the suction side of fan blades up to the point of shock interaction. The motivation for this thesis includes the investigation of shock oscillation mechanisms in such scenarios to mitigate issues related to structural vibrations and potential cracks in fan blades.

Recent studies by Nel et al. [7][9][10] have simplified the complex problem of shock oscillations in low Reynolds number transonic fans by drawing an analogy to laminar oblique shock wave/boundary layer interactions (OSBLIs) on flat plates. They demonstrated that the passage shock in a transonic compressor behaves similarly to the reflected shock in a laminar OSBLI. The oscillation of the passage shock is primarily driven by the breathing of the separation bubble—the upstream growth and collapse of the separated flow region—which alters the flow blockage and causes the shock to move upstream and downstream. This mechanism is similar to the shock movement observed in OSBLIs on flat plates, where the separation

bubble dynamics similarly drive shock oscillations. Although compressor blades have curved surfaces resulting in larger average separation bubbles, the fundamental oscillation mechanism (i.e., on a flat plate) remains comparable if the interaction is strong enough.

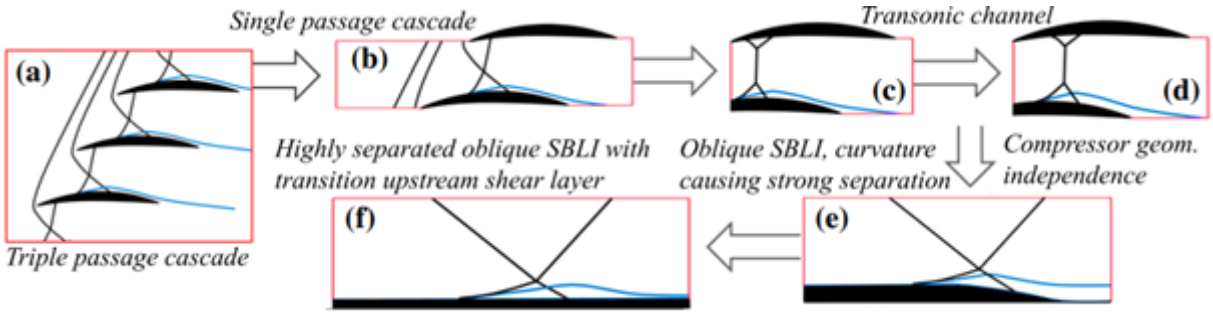

Figure 1.8: Simplification of low Reynolds transonic fan shock oscillation problem to most fundamental form (Nel et al. [7])

In the paper, it is explained that the interaction leads to a significant shock-induced separation, where the shock oscillation mechanism is characterized by the periodic growth and collapse of a separation bubble. This bubble grows upstream, pulling Kelvin-Helmholtz instabilities with it. At a certain point, the generated turbulence is sufficient to suppress the bubble, allowing it to collapse and the process to repeat [7]. Another feature observed was the appearance and the disappearance of a Mach stem during the oscillation, which could represent an additional source of unsteadiness.

The results thus showed a prominent low-frequency content in the shock motion, attributed to a periodic growth and collapse of the separation bubble indicative of a so-called “breathing” shock system. While the experiments confirmed that such transitional SBLIs lead to low-frequency unsteadiness and breathing of the separation bubble, the precise mechanisms responsible for triggering and sustaining these oscillations were not precisely identified.

In conclusion, understanding and managing OSBLIs is important for the performance and safety of high-speed aerospace systems. Through comprehensive experimental and numerical studies, engineers can develop effective strategies to mitigate the adverse effects of SBLIs, ensuring stable and efficient operation of important aerospace components. The present thesis aims to clarify which parameters of the interaction—such as the appearance/disappearance of the Mach stem, the upstream boundary-layer state, or the strength of the impinging shock—are essential in driving this low-frequency behavior.

1.2 Thesis Outline

Chapter 2 begins with an overview of the theoretical background necessary to understand the rest of the report. It provides a comprehensive review of the fundamental principles of shock wave-boundary layer interactions, highlighting the different types of interactions with a focus on oblique shockwave boundary layer interactions (OSBLIs). The chapter also reviews the central relevant literature to place the current project within its appropriate research context. Finally, the research questions this thesis aims to address, which arise from the literature study, are stated.

Chapter 3 presents the design process to address the research questions posed in Chapter 2 by performing an experimental campaign. This includes a discussion of the facilities available for the experiments, the wind tunnel model, the measurement conditions and a description of the test matrix. This chapter will also discuss the main design challenges that had to be overcome, and it concludes with the experimental procedure followed during the project.

In Chapter 4, the flow measurement and post-processing techniques are presented. The test cases mainly consist of high speed and spark light Schlieren visualization. The outputs from these tests consist of large sets of image sequences, capturing the flow dynamics at high acquisition rates. To make sense of this extensive data, various processing techniques are applied to identify key features of the flow and its interactions, such as characteristic frequencies and time-averaged patterns. This chapter introduces and explains the data and signal processing methods employed, detailing how they help extract and interpret the important aspects of the flow behavior.

The experimental results are discussed in Chapter 5. This includes the characterization of the physical phenomenon, frequency analyses, investigation of the relevant length scales, and shock polar comparisons for the cases with regular- or Mach reflections. The chapter begins by presenting the results from the Schlieren visualizations and aims to compare the different flow conditions, using the data processing methods defined in Chapter 4. The main point is to verify the degree to which the research questions have been answered, and to be able to draw meaningful conclusions which future work can build upon.

The report concludes with Chapter 6, which summarizes the findings and makes recommendations for future work. Based on the conclusions drawn from Chapter 5, potential areas for further research will be identified to enhance the understanding and control of SBLIs in practical applications.

Chapter 2

Literature Review

The purpose of this section is to provide context for the upcoming research by reviewing the current state of the art on oblique shock wave–boundary layer interactions (OSBLIs). The chapter begins with an explanation of the boundary layer concept and the boundary layer transition. This gives more insight into how the boundary layer behaves under adverse pressure gradients and why an impinging shock affects its behaviour. The discussion continues with a general overview of SBLIs, highlighting important theoretical and mathematical considerations.

Furthermore, the issues of "shock oscillation", "shock unsteadiness", and "length of the interaction" are recurring throughout this topic. It is essential also to address the research done on the analysis of (un)steady OSBLIs; the relationship between the separation of the boundary layer and the reflected shockwave oscillation remains a topic of interest in OSBLI research. For instance, Poggie et al. [11] emphasized two main mechanisms: forcing by the upstream boundary layer (amplifier model) or global instabilities, which are intrinsic to the separated flow (oscillator model). Other phenomena are analyzed, such as shock-induced separation, shock oscillation mechanisms, and the effects of flow and geometry conditions (Mach number and shock impingement angles). Additionally, the impact of upstream boundary layer conditions, the dynamics of the separation bubble, and the implications of flow unsteadiness are examined. Waindim et al.

Waindim et al. [12] highlight that uncovering the causes of low-frequency unsteadiness in shock wave boundary layer interactions (SWBLI) has significant practical implications in aerodynamics. If this unsteadiness is attributed to large-scale (turbulent) structures upstream (i.e., the so-called "forcing of the upstream boundary layer"), then control strategies could aim to disrupt or prevent these formations. On the other hand, if the unsteadiness originates within the interaction itself (i.e., the global instabilities intrinsic to the interaction itself), effective control methods might focus on the separation bubble that influences shock movement or on altering the entrainment characteristics of the shear layer. Thus, more targeted and efficient aerodynamic control techniques can be developed by pinpointing the exact source of the unsteadiness.

Based on this literature review, knowledge gaps are investigated, and several research questions are formulated, which could benefit from more analysis. This chapter will address these points and provide a comprehensive theoretical framework and an overview of current research, setting the stage for this thesis's subsequent experimental and analytical investigations.

2.1 Definitions and general overview

2.1.1 The boundary layer concept

Before addressing the phenomenon of shockwave boundary layer interactions, it is essential first to establish a clear understanding of the boundary layer itself, how it develops and responds under various flow conditions, particularly under adverse pressure gradients (which are directly relevant to this thesis given the inherent pressure rises associated with shockwaves). The concept of the boundary layer was initially proposed by Ludwig Prandtl in 1904 at the Third International Congress of Mathematicians in Heidelberg, fundamentally changing the understanding of fluid flow near solid surfaces.

In their foundational text, "Boundary-Layer Theory", building on Prandtl's work, Schlichting and Gersten [13] elaborate that in high Reynolds number flows, the viscosity effects become significant mainly in a thin region near the surface known conceptually as the boundary layer. Physically, this arises because of the no-slip condition, which states that fluid molecules directly at a solid boundary adhere to it, causing their velocity to be zero relative to the surface. This phenomenon results from molecular viscosity and intermolecular forces, creating velocity gradients within a thin fluid layer adjacent to the surface. Away from this layer, the fluid velocity rapidly approaches the free-stream value, resulting in a distinct shear layer where frictional (shear) stresses occur.

Furthermore, in their explanation of the boundary layer concept, Schlichting and Gersten [13] illustrate the development of the boundary layer using the example of fluid flow along a thin flat plate moving through water. They demonstrated this experimentally by using aluminum particles scattered on the water's surface to visualize flow velocities, where the particle streak lengths indicate flow speed. At the plate surface, the velocity of fluid particles is significantly lower than "further away" (i.e., in the direction perpendicular to the surface). As the fluid moves downstream along the plate, increasingly more fluid particles are slowed down by friction, causing the thickness of the boundary layer to grow continuously. The representation of this phenomenon is depicted in Figure 2.1 and is commonly recognized in engineering fluid mechanics applications. Although the boundary layer has a physically continuous transition into the outer flow region, the concept of boundary-layer thickness (δ) is introduced as a practical simplification. This thickness is typically defined as the point where the local fluid velocity reaches a specific fraction (commonly 99%) of the external free-stream velocity, denoted as δ_{99}.

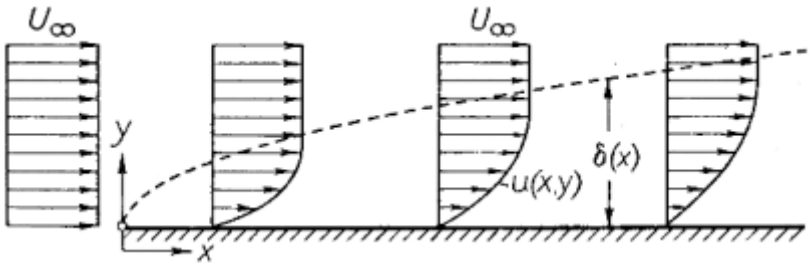

Figure 2.1: Schematic of the boundary layer development on a flat plate (Schlichting and Gersten [13])

The transition from a laminar to a turbulent boundary layer involves a complex yet clearly defined sequence of physical phenomena, thoroughly described by White [14], as well as Vos & Farokhi [15]. Initially, the boundary layer experiences disturbances—small perturbations that eventually amplify downstream. These disturbances evolve into two-dimensional wave-like oscillations, known as Tollmien-Schlichting waves, which represent the primary instabilities within the boundary layer. As these waves propagate further along the surface, nonlinear interactions cause their wavefronts to deform, forming characteristic three-dimensional lambda-structures. These secondary instabilities rapidly grow, eventually breaking down into distinct regions of turbulent flow known as turbulent spots. Finally, as these spots increase in number and expand, they coalesce, ultimately transforming the entire boundary layer into a fully turbulent state (see Figure 2.2).

The flat plate model which will be used in the present thesis was also used in the PhD thesis of Giepman [16]. To accurately determine the transition location on the plate, Giepman utilized several experimental techniques including oil-flow visualization (Figure 2.3), spark-light Schlieren visualization, Particle Image Velocimetry (PIV), and infrared thermography. His oil-flow visualizations indicated an average transition to turbulence around 70 mm downstream from the leading edge, with initial turbulent streaks appearing slightly upstream, suggesting a transition onset between 55 and 60 mm. Occasionally observed turbulent wedges, resulting from localized particle accumulations in the oil layer, clearly delineated the boundary between laminar and turbulent flow. The spark-light Schlieren visualization method, providing instantaneous snapshots of the flow, revealed fluctuating transition onset points between 55 and 65 mm due to the inherently intermittent nature of boundary layer transition. The lower

limit of this range, 55 mm, should be interpreted as the initial onset of transition, consistent with the fluctuating and intermittent characteristics observed in boundary layer transitions.

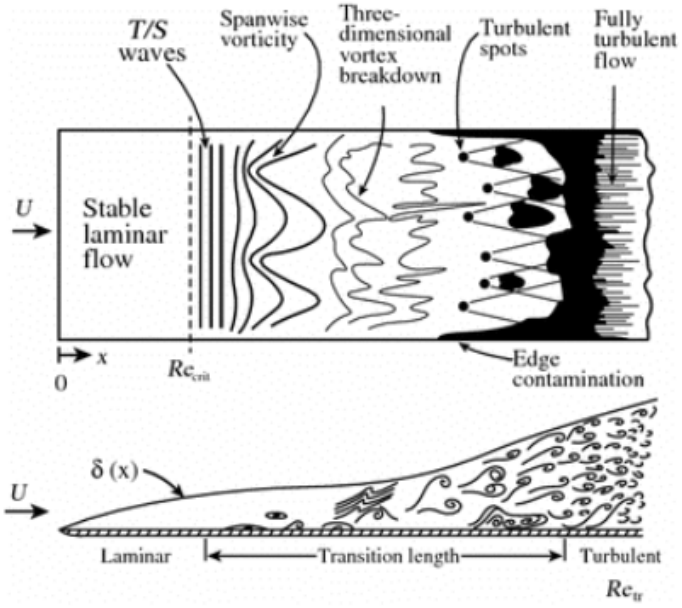

Figure 2.2: Schematic of transition on a flat plate (Vos & Farokhi [15])

It is worth noting that the tests performed by Giepman were done on the flat plate at Ma = 1.7. Even though the test cases for the present thesis will involve higher Mach numbers, it will be considered that the effect of this change in Mach number is negligible. With that being said, these are the Reynolds identified for the natural flat plate transition by Giepman [16]:

- Re_x in the interval 1.4 – 1.8 million: laminar;
- Re_x in the interval 2.1 – 3.2 million: transitional;
- Re_x > 3.5 million: turbulent.

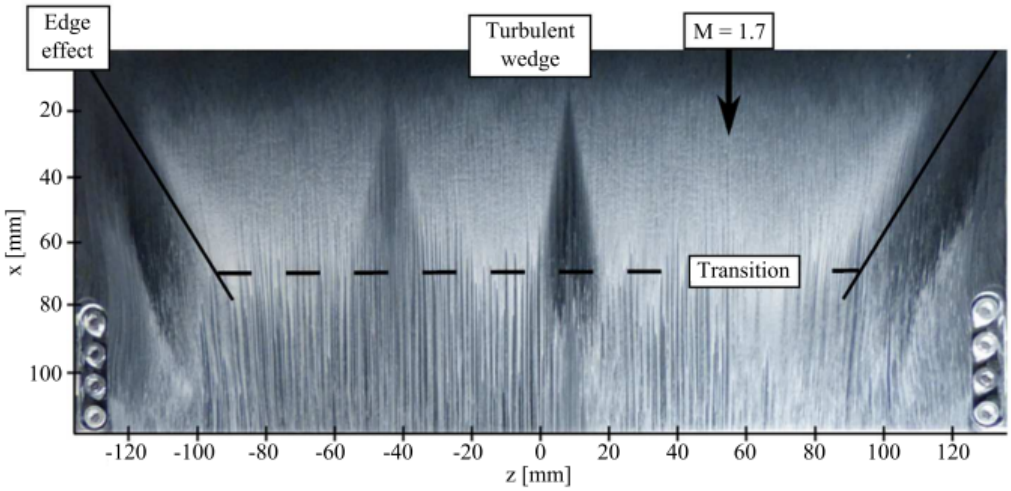

Figure 2.3: Oil flow visualization of the flat plate used in the current thesis (Giepman [16])

It is important to be sensible when processing this information. As noted by Giepman [16], "stronger shocks promote boundary layer transition, which promotes reattachment (...)". Therefore, it is expected that computing the Re_x based on the theoretical shock impingement location might yield values that would fall within the transitional range, but due to the OSBLI, the interaction could be turbulent. This can be verified when doing tests for values close to the upper limit for the laminar/transitional theoretical values. Nevertheless, these results will be used in the current analysis to identify the relevant Reynolds numbers that correspond to transitional shockwave boundary layer interactions.

2.1.2 Overall description of SBLIs

The brief introduction on the boundary layer concept and transition allows the step towards discussing SBLIs. When a boundary layer encounters an adverse pressure gradient, the near-wall fluid decelerates and loses momentum, the wall shear can even reverse, and the layer detaches from the surface, leading to separation.

As detailed in Babinsky & Harvey [1] and briefly presented in the introduction, SBLIs are relevant because they can lead to substantial increases in drag, potential flow separation, and unsteadiness, which can adversely affect vehicle performance and structural integrity.]

The authors explain that, in the context of transonic and supersonic flows, SBLIs are particularly significant due to the intense adverse pressure gradients imposed by shock waves: when a shock wave impinges on a boundary layer, it creates a complex flow structure where the boundary layer thickens and may even separate. This separation can generate large-scale unsteadiness, such as buffeting in wings, buzz in air-intakes, and unsteady side loads in nozzles. These phenomena can limit the performance of aerospace vehicles and, in severe cases, cause structural damage. The interaction between the shock wave and the boundary layer involves a viscous-inviscid coupling, where the boundary layer's distortion influences the neighboring inviscid flow, exacerbating the flow's overall complexity.

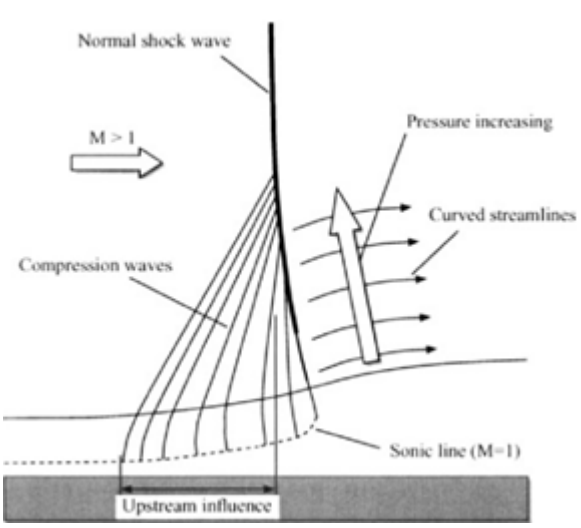

(a) sketch - unseparated interaction

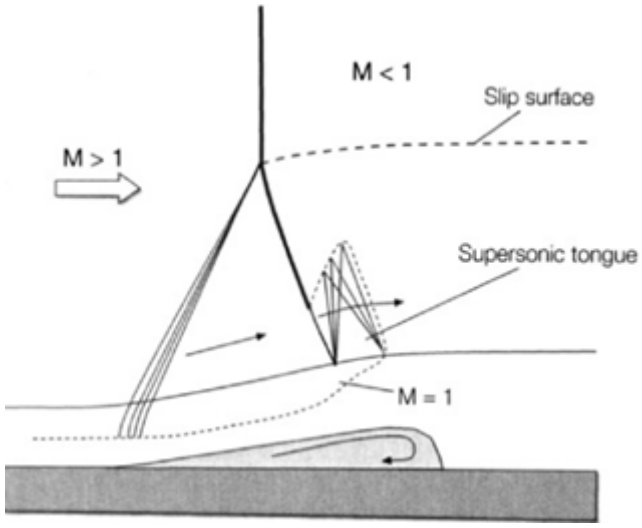

(b) sketch - separated interaction

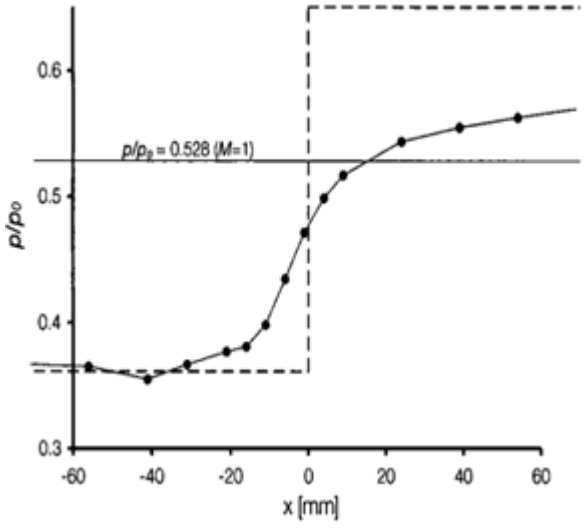

(c) pressure jump across the interaction, unseparated SBLI

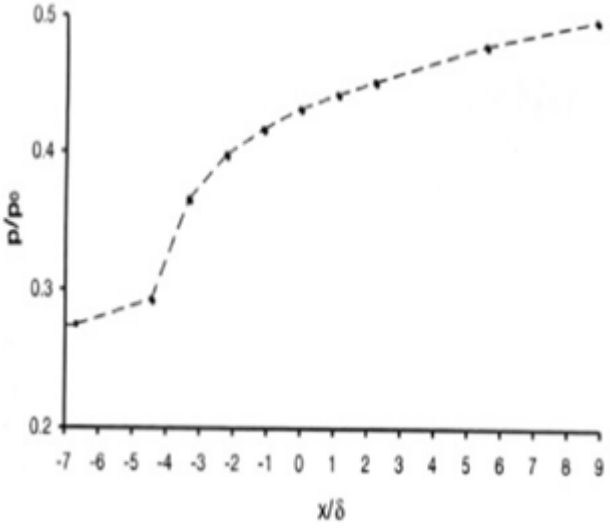

(d) pressure jump across the interaction, separated SBLI

Figure 2.4: Transonic SBLI - separated and unseparated interactions (Babinsky & Harvey [1]

Babinsky & Harvey [1] first begin with an introduction of transonic SBLIs – a case often considered for commercial aircraft and in transonic fans and compressors. They present two situations which are illustrated in Figure 2.4 – an unseparated and a separated interaction. Although the present thesis focuses more on supersonic interactions and oblique shockwaves, the physical mechanisms of interest bear similarities. Thus, in transonic shock-boundary layer interactions (SBLIs), the interaction between the shock and the boundary layer causes the shock to smear into compression waves rather than producing a sharp pressure jump (Figure 2.4a, Figure 2.4b). In the attached flow case, the pressure spreads upstream due to subsonic flow near the wall, weakening the shock and leading to a smoother pressure rise (Figure 2.4c). The streamlines are deflected "away" from the wall, contributing to this effect. In separated flows, the interaction forms a lambda-shock structure (Figure 2.4b), with a so-called "separation bubble" forming. This phenomenon is characterized by a two-step pressure rise with smoother transitions. These phenomena result from the boundary layer's response to the adverse pressure gradient imposed by the shock, as presented by Babinsky & Harvey [1].

2.1.3 Boundary-Layer-Shock-Pressure-Jump Competition

In what Babinsky & Harvey [1] refer to as the "Boundary-Layer-Shock-Pressure-Jump Competition", a convenient starting point for describing an SBLI is the steady, two-dimensional boundary-layer equation for the streamwise momentum:

$$\rho u \frac{\partial u}{\partial x} + \rho v \frac{\partial u}{\partial y} = -\frac{dp}{dx} + \frac{\partial \tau}{\partial y} \tag{2.1}$$

Wherein ρ represents the density, u and v represent the velocity components in the x- and y- directions respectively, p the pressure in the flow, and τ denotes the shear stress. Equation 2.1 is useful because it shows two key components: the convective acceleration of the flow inside the boundary layer on the left, and the effects of the imposed pressure gradient (dp/dx) and the momentum exchange by shear on the right. The impinging shockwave produces a sudden additional adverse pressure gradient, the momentum of the low-speed boundary layer flow is retarded and, if the shear stress near the wall cannot counteract the pressure rise, the flow can separate.

Babinsky & Harvey [1] illustrate this phenomenon in Figure 2.5, where the boundary-layer flow is noticeably slowed at the onset of the interaction by the combined influence of the shock-induced pressure gradient and the flow's shear forces. The momentum is effectively transferred from the higher-speed outer layer to the slower-speed inner layer, allowing the shear stress there to counter the pressure increase.

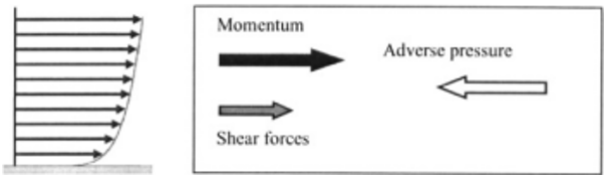

Figure 2.5: Acting forces in an SBLI (Babinsky & Harvey [1])

A more streamlined (yet still illustrative) way to see this "competition" between shock-induced pressure rise and boundary-layer momentum is to neglect the normal velocity v. Treating the boundary layer as a parallel flow, one obtains:

$$\rho u \frac{\partial u}{\partial x} = \frac{\partial}{\partial x}\left(\rho u^2\right) = -\frac{dp}{dx} + \frac{\partial \tau}{\partial y} \tag{2.2}$$

And, integrating Equation 2.2 across the boundary layer from the wall (y=0) to its outer edge (y=δ) yields:

$$\frac{d}{dx}\int_{\delta_i}^{\delta} \rho u^2 \, dy \approx -\frac{dp}{dx}(\delta - \delta_i) + \left(\tau_\delta - \tau_{\delta_i}\right) \approx -\frac{dp}{dx}\delta \tag{2.3}$$

Where δ_i is an "inner" boundary layer thickness. The simplified Equation 2.3 shows the relationship between the flow momentum and the pressure gradient. Laminar and transitional (within the scope of the present thesis) boundary layers have profiles and characteristics that may not withstand a strong pressure gradient coming from a shockwave, making boundary-layer separation – and hence unsteadiness – more pronounced.

Babinsky & Harvey [1] also mention that the response of the boundary layer to the shock-induced pressure gradient involves complex interactions between viscous and inviscid forces, leading to phenomena such as flow separation and shock-induced unsteadiness. These interactions are further complicated by factors such as boundary layer transition, the presence of turbulence, and the influence of wall temperature.

2.1.4 The Free Interaction Theory

The free interaction theory of Chapman [17] provides a unifying way to analyze the onset region of a shock wave–boundary layer interaction without requiring detailed knowledge of the downstream flow conditions. Building on the original hypothesis that everything which occurs upstream of the shock impingement should be largely independent of the shock strength, the free-interaction theory is used as a tool that allows us not to focus on the specifics of how the shock is generated; thus, for example, using different shock generator angles that yield the same inviscid pressure jump should produce broadly similar upstream flow modifications, so long as the overall Mach number and boundary-layer state remain comparable.

This theory and a practical application of it is very well described in the PhD thesis of Giepman [16], where the correlation function $F(\bar{x})$ is presented, which captures the developing pressure rise in the early (upstream) portion of the interaction. A commonly cited form of this relationship, adapted from Erdos and Pallone [18] for laminar (or transitional) SBLIs, is:

$$C_p(\bar{x}) = F(\bar{x}) \sqrt{\frac{2\,C_{f_0}}{\sqrt{Ma^2-1}}} \tag{2.4}$$

Where $\bar{x} = \frac{x - x_{sep}}{L_{sep}}$, with x_{sep} the streamwise location where separation occurs, and L_{sep} the distance between the separation location and where the pressure rise is observed first. This equation couples the pressure rise through the interaction to the flow conditions upstream, as explained in Giepman's thesis. In his thesis, Giepman [16] showed that there is a good correlation between the function defined in equation Equation 2.4 and different OSBLI experiments performed for different shock strengths (shock impingement angles from 1°- 5°), as seen in Figure 2.6.

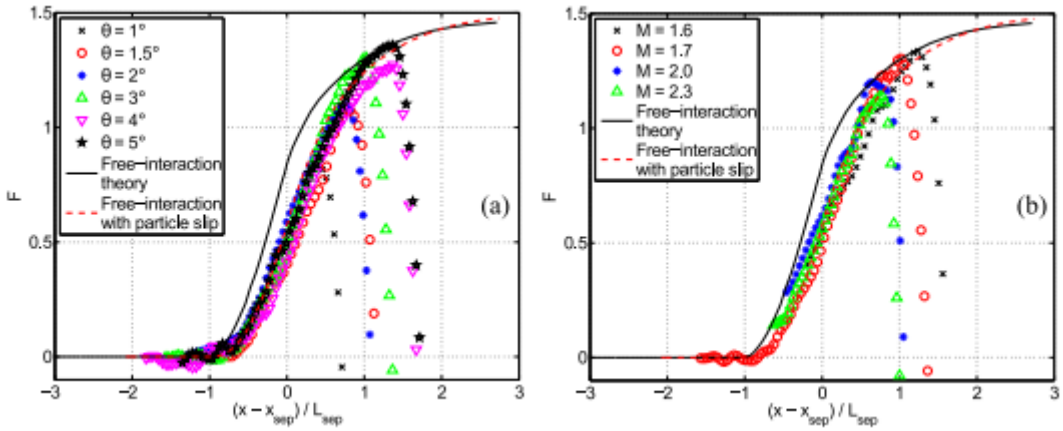

Figure 2.6: Comparison of the correlation function at different shock strength OSBLI conditions(Giepman [16])

As seen in the figure, the experiments performed showed almost the same pressure rise, with a sudden drop in the region where linear supersonic theory did not hold true anymore.

The overall agreement of free-interaction theory with the experiments performed by Giepman [16] allowed the assumption that variations in shock generator angle do not produce significant differences, as long as the inviscid pressure jump remains the same. As such, different shock generator setups—despite differing shock deflection angles—yield virtually the same kind of SBLI because the primary cause of unsteadiness lies within the interaction process itself.

2.2 Unsteadiness of SBLIs

The source of the unsteadiness of SBLIs is very popular among researchers and aerodynamicists, as explained by Dolling [19]. There are two main theories that attempt to explain the physical mechanism occurring within SBLIs of all types (not only oblique). A very good synthesis of these two explanations is presented in the work of Webb et al. [5], namely that either the low frequency motions are caused by upstream effects (correlating the oscillation to bursting per Andreopoulos [20] or streamwise elongated structures - Ganapathisubramani et al. [21] and Beresh et al. [22]), or that the perturbations that are formed downstream cause the instability (through vortex shedding from the shear layer - Piponniau et al. [23]). This latter explanation attributes the unsteadiness to a Kelvin-Helmholtz type instability.

A significant portion of the earlier investigations which mainly focused on the source of the unsteadiness (leading to the two explanations including either the upstream disturbances or the dynamics of the separation bubble itself) were performed in the context of fully turbulent or laminar SWBLIs. High-speed vehicles could, however, encounter transitional SWBLIs, which, according to Sandham et al. [24] combines the attributes of both turbulent and laminar SWBLIs. This hybrid nature was discovered to add to the local heating, drag and unsteadiness of the interaction, as explained in both Murphree et al. [25] and Shinde et al. [26].

While the research of Nel et al. [7] attributes the unsteadiness to a Kelvin-Helmholtz type instability, a weaker interaction investigated by Shinde et al. [27] on transitional SWBLIs over a flexible panel at Ma = 2 has revealed a "streamline curvature in the laminar boundary layer, initiating a centrifugal instability similar to Görtler instability; where the nominally two-dimensional and steady SWBLI becomes three-dimensional and unsteady at a critical Reynolds number", as described by Shinde et al. [27]. Notably, these Görtler vortices have also been observed in fully turbulent SWBLIs (Pasquariello et al. [28] and Zhuang et al. [29]).

Most of these analyses (including the transitional SWBLI investigated by Shinde et al. [27], which is the most similar analysis to the one of the current thesis) are performed for relatively weak OSBLIs (wedge angle at most 9.5o). Not much is researched on the topic of the unsteadiness source of highly separated transitional OSBLIs in the Mach range and shock strength that will be studied in this thesis, and therefore the previously discussed oscillation mechanisms which are ascribed to either the upstream effects or the interaction itself are cautiously taken into consideration but they are not automatically described as the explanation to the unsteadiness which appears during the experiments performed in the present thesis.

Dussauge et al. [30] compiled a series of different SBLI configurations (as seen in Figure 2.7: oblique SBLIs, compression ramp flows, blunt fin interactions, overexpanded nozzle SBLIs) and made a comparison of the interaction/oscillation length at different flow conditions.

In their paper, Dussauge et al. [30] used the nondimensional interaction length L_{ex}/L, where L_{ex} represents the "excursion length" of the shock (the distance travelled by the shock upstream before the oscillation repeats), and L represents the "interaction length", defined as "the distance between the median position of the reflected shock and the extrapolation to the wall of the incident shock" (Dussauge et al., [30]). With Figure 2.7, they noticed typical values of 0.3-0.5 for this nondimensionalized length, and justify the use of the interaction length L as the characteristic length scale for a Strouhal number analysis: $S_L = \frac{f_s L}{U_e}$, wherein f_s is the characteristic frequency of the oscillation, and U_e the external velocity.

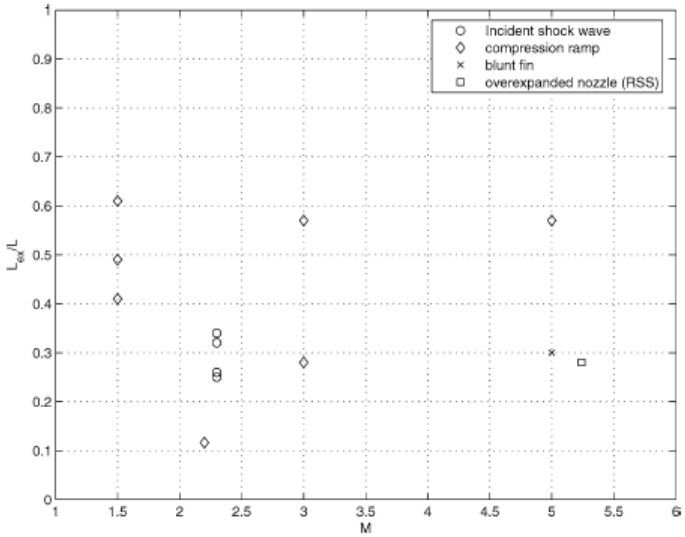

Figure 2.7: Oscillation length for the unsteady shock for different configurations (Dussauge et al. [30])

This is important because, to make meaningful comparisons between different test cases, concentrating on the dimensionless Strouhal number rather than the "raw frequency" helps normalize data across varying flow speeds, length scales, and operating conditions. This universal approach ensures that the unsteady flow phenomena are accurately captured for scaling, predictive modeling, and design optimization.

Furthermore, Dussauge et al. [30] performed a preliminary Power Spectral Density (PSD) comparison between two areas: one is at the shock foot, where the dimensionless distance $X* = 0$. This dimensionless distance is defined by $X* = (X - X_0)/L$, where X is the longitudinal position, and X_0 is the abscissa of the mean shock (hence why $X* = 0$ at this location).

The second location is well inside the interaction zone, at $X* = 0.78$, and the PSD comparison is shown in Figure 2.8, showing clear differences between the energetic scales of the two regions; the region close to the shock foot is characterized by a low-frequency peak, while the area closer to the recirculating zone corresponds to higher frequencies.

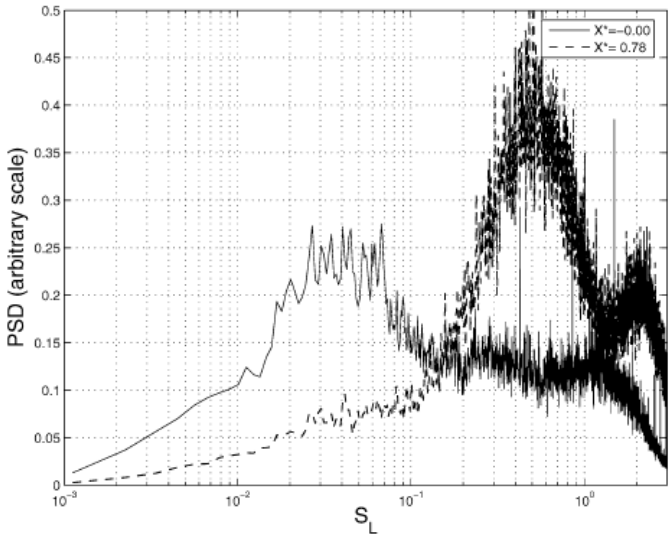

Figure 2.8: Power Spectral Density of wall pressure fluctuations - comparison between the "foot" of the reflected shock and the interaction zone (Dussauge et al. [30])

In the analysis of the current thesis, we will also look at this length scale of the interaction in the Strouhal number analysis and in the identification of the low-frequency peaks which were also shown to appear (for example, in Figure 2.10).

Dupont et al. [31] performed power spectral density analyses for two sections inside the separation area, at $X* = 0.4$ and $X* = 0.7$, as shown in Figure 2.9. They make a remark about the decrease in the frequency peak from 9 kHz to 6 kHz for the $\theta = 8^o$ case, as well as a decrease from 6 kHz to 3 kHz in the $\theta = 9.5^o$ experiment, stressing the idea that the dominating frequencies appear to decrease moving downstream of the flow in the separation zone (Dussauge et al. [30]).

This complements the comparison between the portion upstream of the separation area and inside the separation zone depicted previously in Figure 2.8, showing a further decrease in the frequency peaks recorded for OSBLIs. On the other hand, moving further downstream beyond the separation area leads to the same higher-order frequencies as the ones recorded in the portion upstream of the separation zone of the interaction, as explained in Dussauge et al. [30].

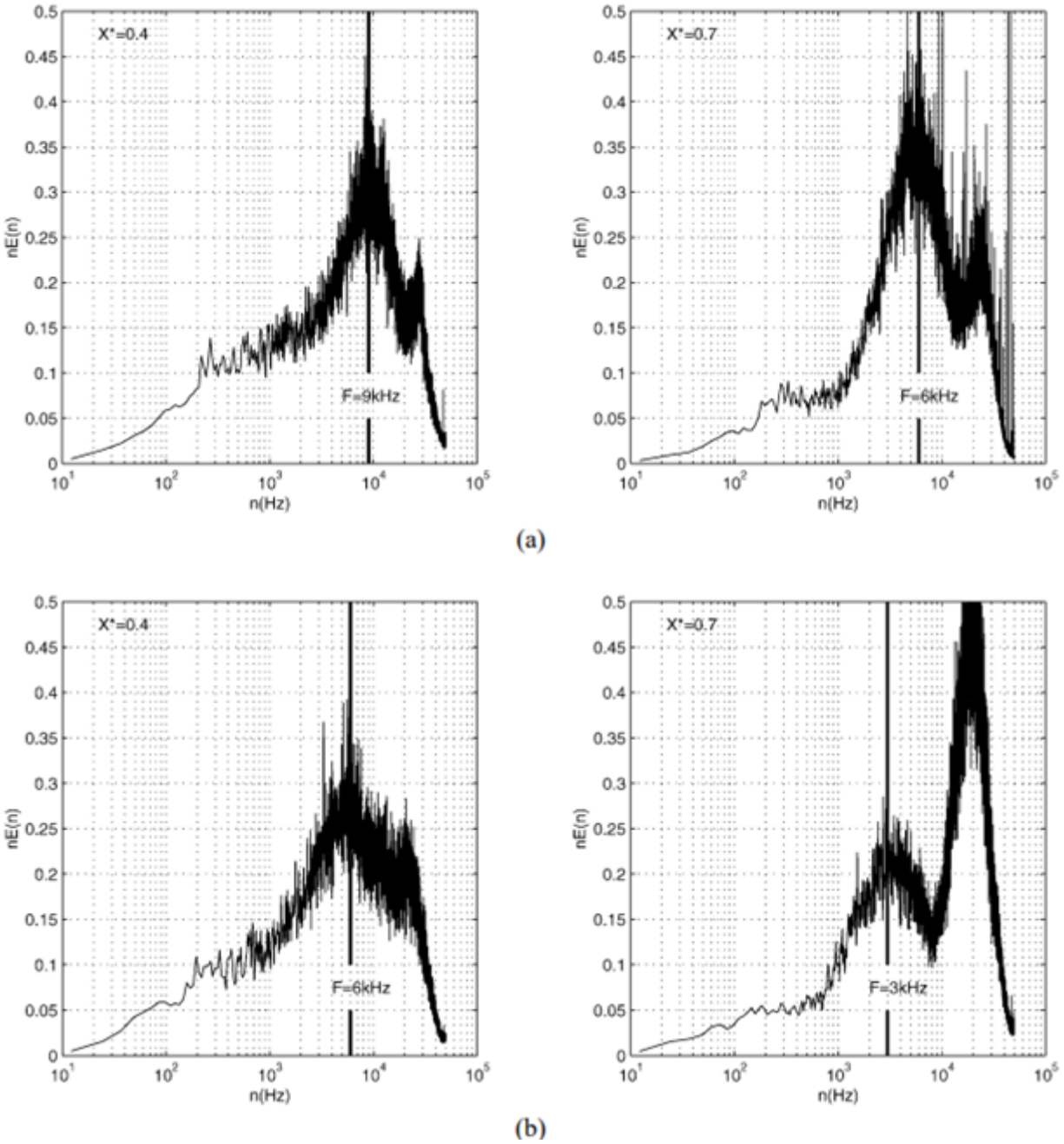

Figure 2.9: Power Spectral Density analysis of an Oblique SBLI for two locations: $X* = 0.4$ and $X* = 0.7$ at a) $\theta = 8^o$, and b) $\theta = 9.5^o$ (Dupont et al. [31])

To bring the case study to a more particular situation, a DMD analysis by Nel et al. [9] (Figure 2.10) for the previously presented research case shows a peak in the frequency content at 3728 Hz showing that there is indeed a low-frequency oscillation of the laminar separation shockwave. It would be interesting to extend

this analysis to further cases and compare the frequency spectra obtained to the physical phenomenon which is observed.

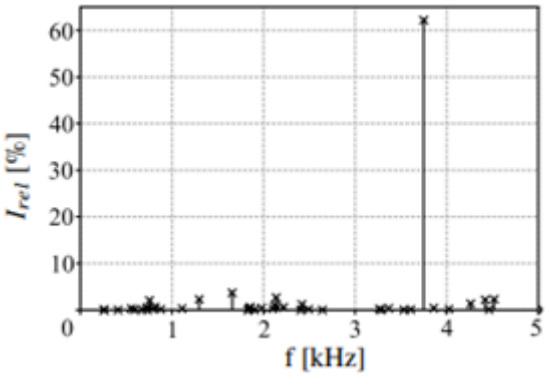

Figure 2.10: Transitional OSBLI DMD spectrum (Net et al. [9])

Several passive and active separation control techniques have been employed to mitigate the adverse effects of the unsteadiness of these interactions, such as ramps (Babinsky et al. [32]), micro-vanes (Anderson et al. [33]) and plasma actuators (Webb et al. [5]). For the purpose of this thesis, it would be interesting to build on the work of Nel et al. [9] and continue the study of the effect of using a 2D step to trip the flow, then provide a comparison with the baseline cases where the shock oscillation mechanism with a low-frequency movement of the shock was identified. The configuration used by Nel et al. is found in Figure 2.11, where a 100 micron strip was applied. Since it would be preferable to minimize the height of this passive control system in order to lower the friction drag it would create, it would be interesting to see how the shock oscillation mechanism behaves when applying thinner (or thicker strips).

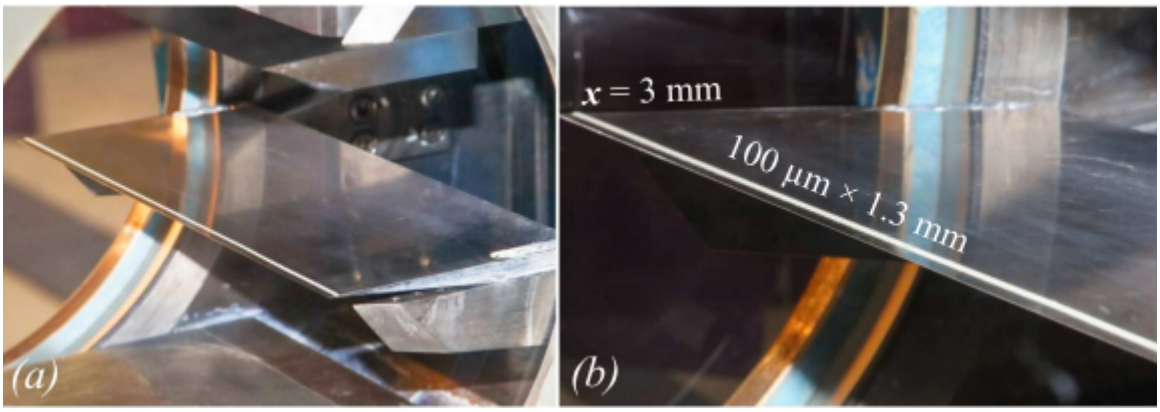

Figure 2.11: Flat plate overview with the 2D step applied (Net et al. [9])

2.3 Shock-shock interactions and shock polars

In the context of SBLIs where separation occurs, it becomes apparent that at least two shockwaves will exist: the shockwave that causes the SBLI (the "impinging" shockwave for oblique SBLIs) and the shockwave that appears by the effective "ramp" that forms when the boundary layer separates. These two shockwaves can interact and change the flow downstream of the interaction, and it is therefore useful to look at how the flow can be characterized in the different regions of the interaction, mainly using shock polars. They are useful because one can obtain a graphical representation of the relationship between the pressure rise across the shock, and the flow deflection angle.

Two examples relevant to the physical phenomena presented in this thesis are illustrated in Figure 2.12. In both scenarios, the flow is initiated by a wedge that produces an attached incident shock (I), with the wedge angle θ larger in the case with Mach reflection (b). The dashed line indicates a streamline, which runs parallel to the lower wedge surface between the incident and reflected shocks (R). In figure b), the

incident shock is stronger than a regular reflection, resulting in a two-shock system. The nearly normal shock, labeled M, forms what is known as a Mach stem, as described by Ben-Dor et al. [34]. The flow downstream of the Mach stem is subsonic, while the region between the slipstream and the reflected shock typically remains supersonic.

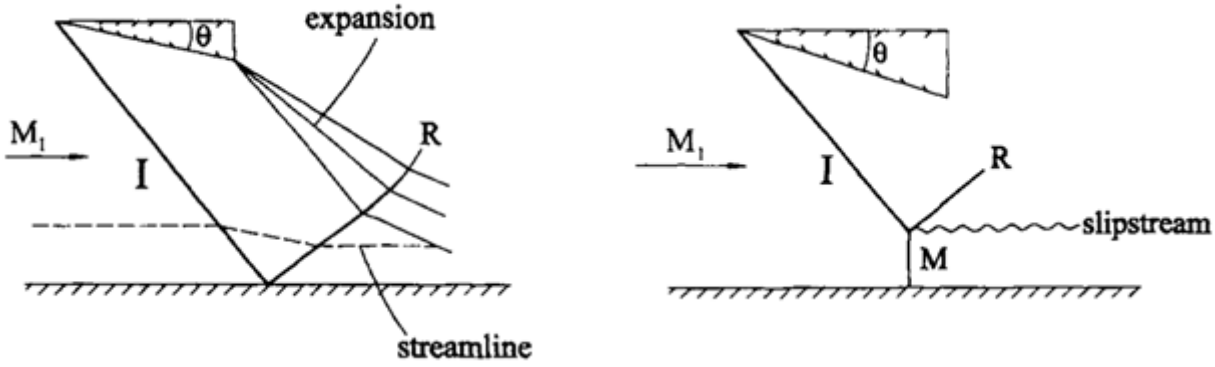

(a) regular reflection **(b)** Mach reflection

Figure 2.12: Steady, oblique wall reflection inviscid cases (Ben-Dor et al. ([34])

Shock polars can be used to understand the behavior of oblique shocks and predict the flow conditions downstream of the shock. The Rankine-Hugoniot equations govern these interactions, providing a framework for analyzing the changes in flow properties across shock waves (Babinsky & Harvey [1]). These graphical representations plot the shock-pressure rise (or the pressure ratio p_2/p_1) against the velocity deflection angle δ) through the shock. The shock polar helps identify the weak and strong solutions for a given deflection angle, indicating the pressure rise and flow conditions downstream of the shock. This shock polar is a closed curve symmetrical with respect to the deflection angle axis.

By defining relevant regions in the flow of an OSBLI, one can perform a shock polar analysis to identify the pressure jumps and Mach number in these different regions. To calculate the pressure jump, the isentropic flow relations are used, which are described in the book of J.D. Anderson, "Fundamentals of Aerodynamics" [35]:

$$\frac{p}{p_1} = \left[\frac{(\gamma+1)\,Ma^2\sin^2\beta}{(\gamma-1)\,Ma^2\sin^2\beta+2}\right]^{\frac{\gamma}{\gamma-1}} \left[\frac{\gamma+1}{2\gamma\,Ma^2\sin^2\beta-(\gamma-1)}\right]^{\frac{1}{\gamma-1}} \tag{2.5}$$

In Equation 2.5, p denotes the pressure in the region after the shockwave (to maintain consistency with the notations in Figure 2.13); β represents the flow deflection angle (related to the geometrical flow deflection angle ϕ in the figure through the oblique shock angle relations; γ denotes the gas adiabatic constant (ratio of the specific heats at constant pressure and volume) – for air, this value is approximately 1.4; finally, Ma represents the Mach number of the flow before passing through the shock.

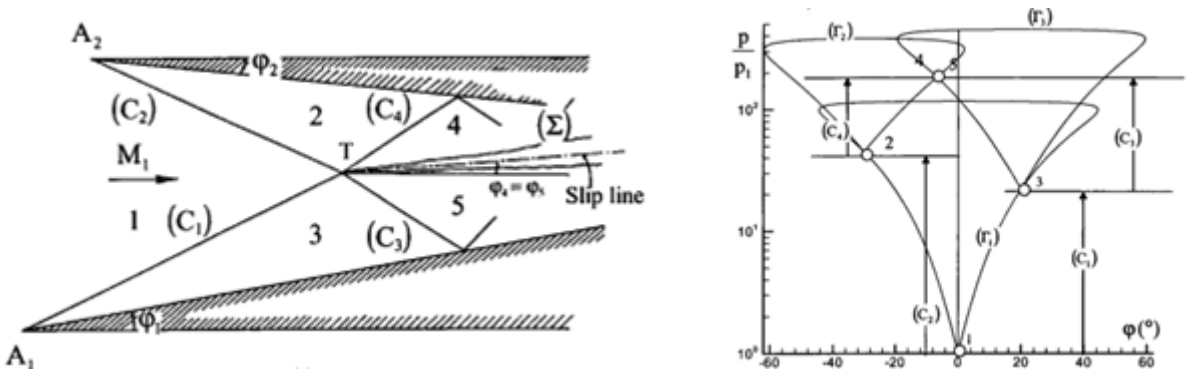

(a) Type I shock-shock interference **(b)** Plane of polars

Figure 2.13: Type I shock-shock interference (regular reflection) - Babinsky & Harvey [1]

In reality, the flow is not inviscid as depicted in Figure 2.12, where the incident shockwaves reflect directly "off the surface". By analyzing the configuration with a boundary layer present, one can see a similarity with the Type I shock-shock interference presented by Babinsky & Harvey, Figure 2.13.

This situation is similar to a regular reflection of an oblique SBLI, with the angle ϕ_2 from Figure 2.13 corresponding to the shock generator angle, and the angle ϕ_1 corresponding to the angle formed between the separation bubble and the surface. Figure 2.13b complements the schematic drawing of the interaction by highlighting the intersection points (4)-(5) of the shock polars corresponding to the two angles ϕ_1 and ϕ_2. This intersection reflects that the pressures and the flow angles in regions 4 and 5 are the same, but the Mach number differs. Therefore, only one slip line appears (hence a "regular reflection").

Similarly, the Mach reflection case is described by Babinsky & Harvey [1] through the development of two slip lines; this occurs when the interaction is so strong that the curves Γ_2 and Γ_1 no longer intersect, see Figure 2.14.

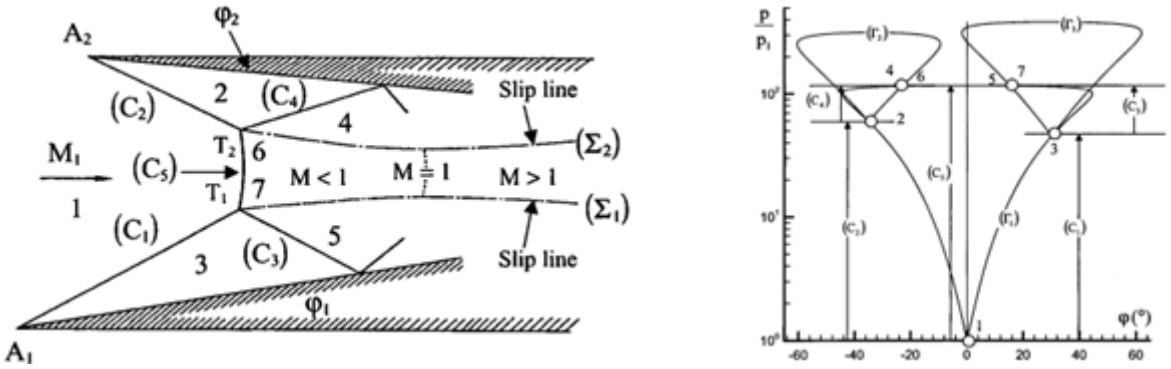

(a) Type II shock-shock interference **(b)** Plane of polars

Figure 2.14: Type II shock-shock interference (Mach reflection) - Babinsky & Harvey [1]

Shock polars are therefore useful for identifying and anticipating certain flow characteristics by knowing the incoming Mach number and the two deflection angles. While the incoming Ma and the deflection angle of the impinging shock are always known (given as input variables), the challenge arises when identifying the angle ϕ_1 corresponding to the separation shock, since that can only be identified after visualizing the interaction.

2.4 Transitional OSBLIs

As we begin the discussion on transitional boundary layers (BLs), it's important to establish a clear understanding of the key terms and physical mechanisms that are involved in OSBLIs. The phenomena associated with these interactions will be crucial throughout the subsequent sections, particularly when dealing with the unsteadiness and frequency analyses that characterize such flows. Terms like "interaction length," "separation length," and "incoming boundary layer" will be introduced and play a significant role in understanding the dynamics of SBLIs under different flow regimes.

The schematic shown below in Figure 2.15, which originates from the work of Pasquariello et al. [36], illustrates the key mechanisms of an oblique shockwave interaction with a turbulent boundary layer. In the paper, they describe the phenomenon in the following way: the adverse pressure gradient from the incident shock (C1) triggers boundary layer separation upstream of the shock's "theoretical" impingement point. Compression waves form in the supersonic region of the boundary layer, coalescing into a reflected shock (C2), which intersects the incident shock, producing transmitted shocks (C3 and C4). The distance between this theoretical impingement point x_imp and the most upstream part of the reflected shock (C2) is defined as the "interaction length" Lint. The transmitted shock (C4) curves through the separated shear

layer and reflects as an expansion fan. Finally, the separated shear layer follows the inclination of the initial part of the separation bubble, deflects towards the wall due to the expansion fan, and reattaches further downstream, forming a reattachment shock (C5) (Pasquariello et al. [36]).

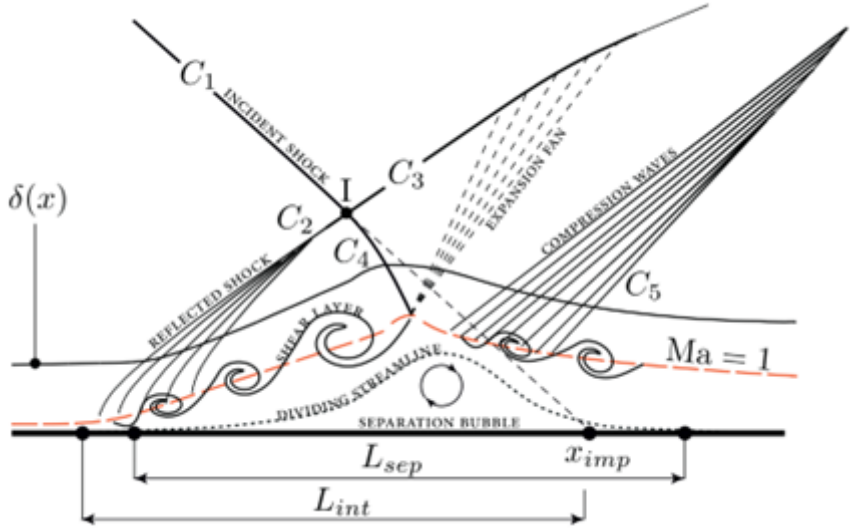

Figure 2.15: Schematic of an OSBLI (Pasquariello et al. [36])

This chapter will explore the differences found in the current state of the art for transitional OSBLIs, with a focus on several key characteristics, such as: physical (oscillation) mechanisms, frequency spectra, interaction lengths, separated vs. unseparated interactions. Note that, in Figure 2.15, the state of the interaction or the incoming boundary layer can be described, apart from using the Reynolds number, by the boundary layer thickness $\delta(x)$.

In the experiments performed in the TST27 at TU Delft by Nel et al. [9], the shock oscillation mechanism depicted in Figure 2.16 was identified: the interaction is considered "transitional" because, when the separation shockwave begins to travel upstream, the boundary layer is still laminar. However, due to the instabilities induced into the flow, the boundary layer transitions to turbulent earlier than for the "natural" flat plate and develops a fan of compression waves which form the "turbulent separation shock" illustrated in both subfigures of Figure 2.16.

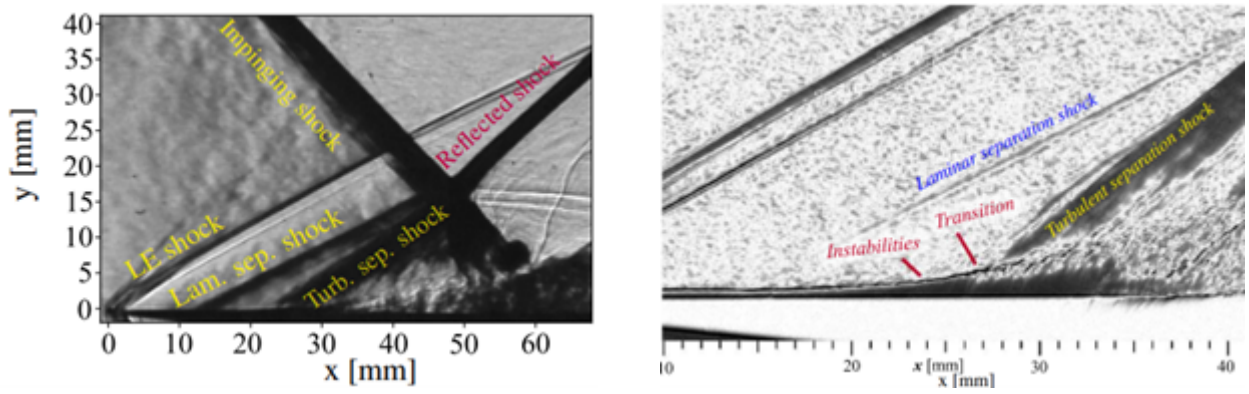

(a) High speed Schlieren visualization **(b)** Spark light Schlieren visualization

Figure 2.16: Transitional OSBLI as found by Nel et al. [9]

Therefore, the "classical" OSBLI schematic which only typically features one oscillating separation shockwave can be adapted to the current scenario such as in Figure 2.17

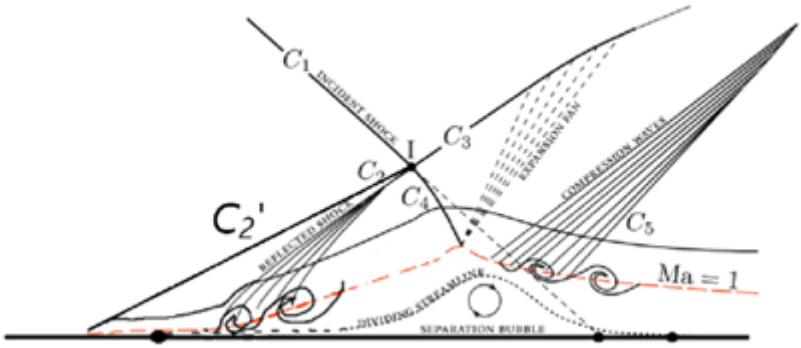

Figure 2.17: Transitional OSBLI, adapted from Pasquariello et al. [36]

However, as previously noted, it is not entirely known what exactly causes this oscillation for some research configurations, while for others it does not. It would be useful, in the context of analyzing transitional OSBLIs, to see where exactly (or for which Reynolds number values), the boundary layer is transitional. Thankfully, as described at the beginning of the chapter, the Ph.D. thesis of Rogier Giepman [16] focused on identifying the natural transition of the boundary layer on this particular flat plate using Schlieren/spark light Schlieren and oil-flow visualizations, infrared thermography, hotwire anemometry and particle image velocimetry.

Furthermore, Giepman identified an "accelerated transition" when testing the natural case and a case with a weak OSBLI separately, Figure 2.18.

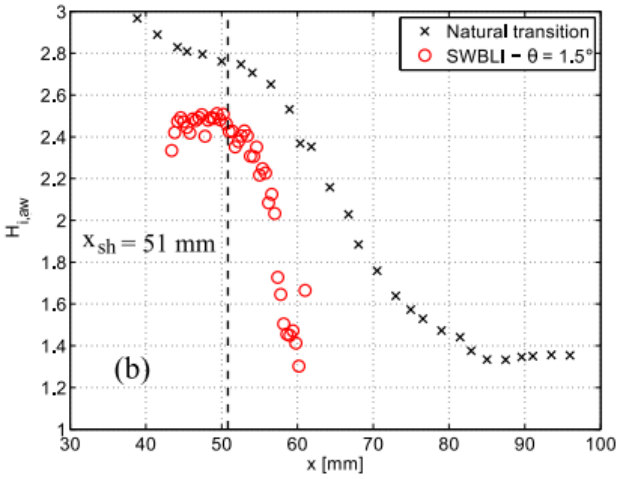

Figure 2.18: Comparison of the transition location for the natural BL flat plate and a case with a weak OSBLI (Giepman [16])

Giepman [16] also performed an analysis of the Re_x trend (Figure 2.19) in the context of this weak (wedge angle of 1.5°) OSBLI at different theoretical impingement locations (incorporating laminar, transitional and turbulent interactions) and found similar sizes angles of the separation bubble for the laminar interactions, and lower sizes for transitional (and, subsequently, turbulent interactions).

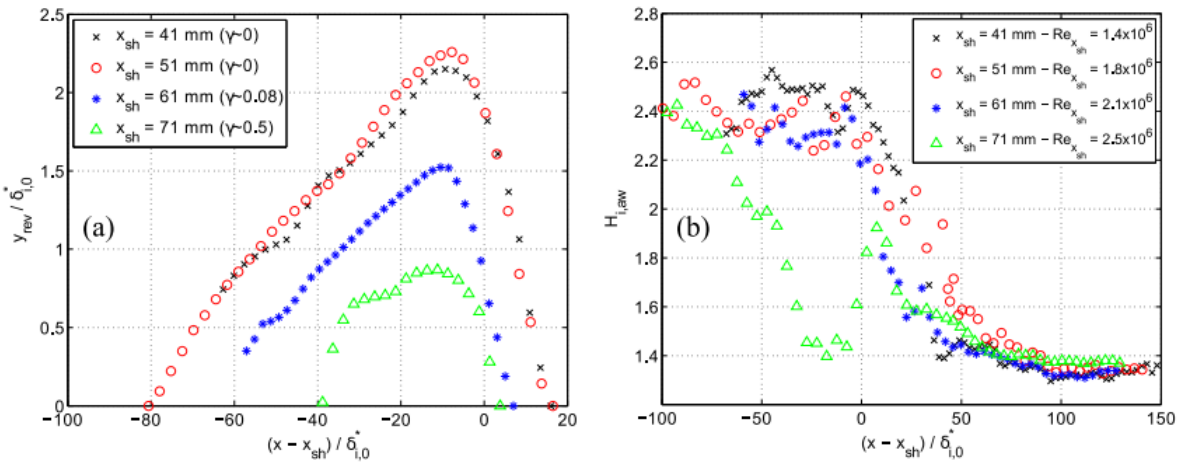

Figure 2.19: Reynolds number effect for a weak OSBLI (Giepman [16])

As presented by Joseph et al. [37], separation not only appears to start much earlier at low Reynolds numbers, but the boundary layer also reattaches much further downstream (Figure 2.20). A larger separation bubble and length of interaction is obtained for this normal transonic configuration.

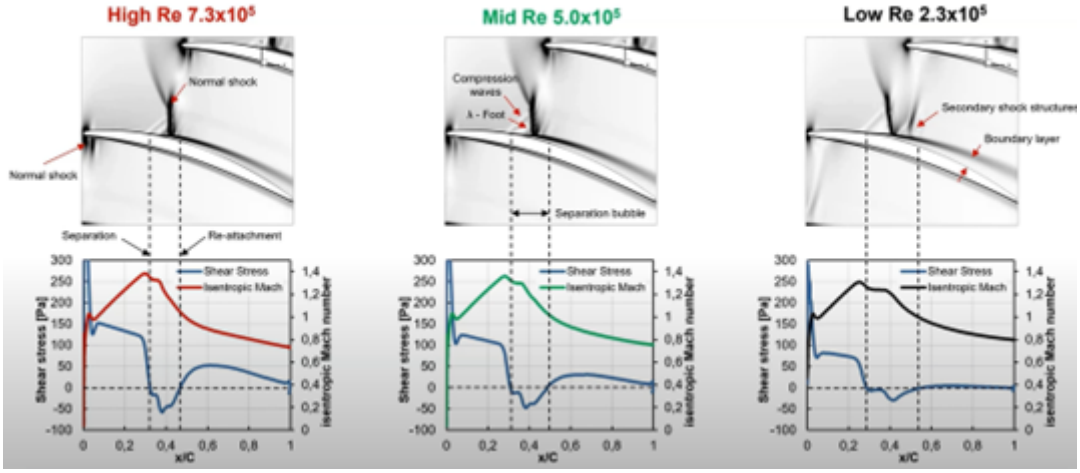

Figure 2.20: Effect of the Reynolds number on the position and size of the separation bubble in transonic fans (Joseph et al. [37])

When it comes to the effect of the shock strength/Mach number, a trend of decreasing length of the separation region with increasing Mach number was found by Giepman [16]. Furthermore, they reported an increase in the separation bubble angle and no clear differences in the transition behavior, Figure 2.21.

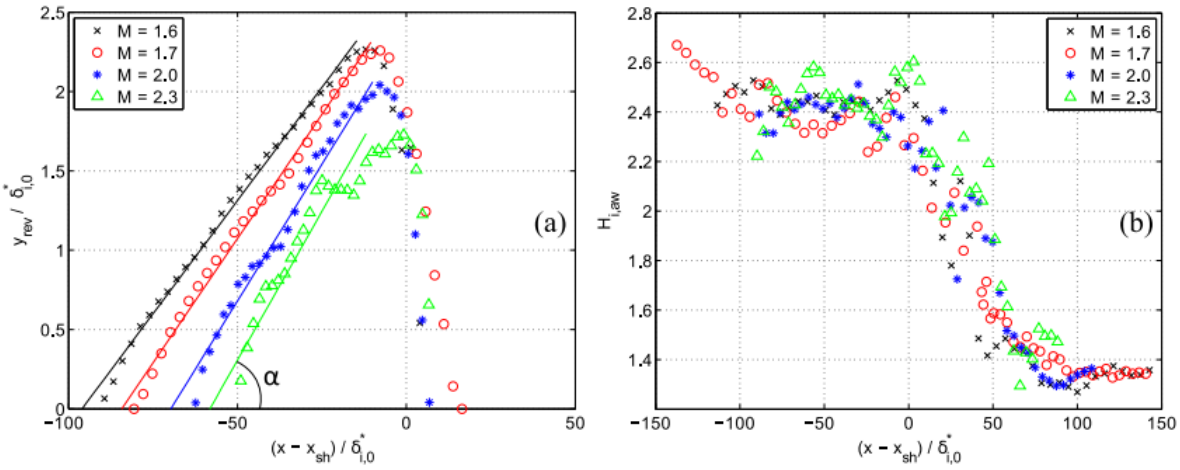

Figure 2.21: Mach number effect for a weak OSBLI (Giepman [16])

Transitional SBLIs are mostly the topic of interest found in the context of hypersonic flows (Babinsky & Harvey [1], Sandham et al. [24], Lugrin et al. [38], Bibin et al. [39]), especially due to the enhanced heat transfer rates which can be further exacerbated by the instabilities of such an interaction. However, research is still lacking for low supersonic transitional OSBLIs and its mechanisms, and there is not much data regarding the effect of the appearance and the disappearance of the Mach stem during the interaction. This conclusion elicits a discussion on the frequency content of these interactions and the unsteadiness of (transitional) OSBLIs.

2.5 Research questions

Despite extensive research, several gaps remain in understanding the specific mechanisms and effects of these interactions under various configurations. This section outlines the key research questions addressed in this thesis, focusing on the identified gaps and the results we aim to obtain.

Primary Research Question: What are the main parameters that can be changed which drive the low-frequency unsteadiness in the massively separated transitional OSBLI?

Sub-questions:

- Does the formation (and periodic disappearance) of a Mach stem, as observed in the “baseline” case of Nel et al. [9], constitute a necessary condition for unsteadiness, and how does its presence or absence influence the overall interaction?
- Do the Reynolds numbers calculated at the theoretical shock impingement point under a “natural boundary layer” scenario indicate a laminar separation shock followed by accelerated transition, and how does this influence unsteadiness?
- How effective are flow control methods (the 2D steps to trip the boundary layer) in reducing shock oscillation amplitude and unsteadiness?
- In what ways do variations in parameters such as local Reynolds number (Rex), Mach number (Ma), and inviscid pressure jump affect the dominant frequency content and the spatial extent of the interaction? Can one parameter be isolated to evaluate its individual impact?

By addressing these questions, this thesis will contribute to a better understanding of the mechanisms driving shock oscillations in the context of transitional OSBLIs, the impact of boundary layer conditions, and the effectiveness of various flow control methods.

Chapter 3

Experimental Design

3.1 Experimental facilities

The experimental campaign was conducted in the TST-27 transonic-supersonic wind tunnel of TU Delft (pictured in Figure 3.1). More specifically, this is a blowdown supersonic wind tunnel supplied by an external pressurized reservoir capable of maintaining air pressures between 25 and 40 bar. The test section, measuring 270 × 280 mm, and allowed for model mounting via the sidewall attachments.

Figure 3.1: The TST 27 blowdown wind tunnel

A detailed schematic of the wind tunnel is presented in Figure 3.2. The tunnel provides a Mach number range from 0.5 to 0.85 in the transonic regime and from 1.15 to 4.2 for supersonic cases [2]. Control over the total pressure is achieved through a valve that regulates the settling chamber pressure (refer to Figure 3.2). In terms of the startup pressures, the upper bound is constrained by the system's maximum mass flow capacity of 50 kg/s, while the lower bound is set by the need to avoid condensation in the test section. A discussion focused on the total pressure in the wind tunnel will be made further in this section when discussing the problem of "tunnel unstart". Finally, the total temperature of the airflow is dictated by the external reservoir temperature, which remains at ambient conditions. In this case, it was approximately 15°C (288 K). The total pressure and total temperature are relevant parameters when it comes to computing the Reynolds number of the flow using the isentropic flow relations (which yield the freestream conditions) and Sutherland's law (which yields the freestream viscosity).

The total pressure and total temperature are relevant parameters when it comes to computing the Reynolds number of the flow using the isentropic flow relations (which yield the freestream conditions) and Sutherland's law (which yields the freestream viscosity).

[2] https://www.tudelft.nl/en/ae/organisation/departments/flow-physics-and-technology/facilities/high-speed-wind-tunnels/tst-27-transonicsupersonic-windtunnel

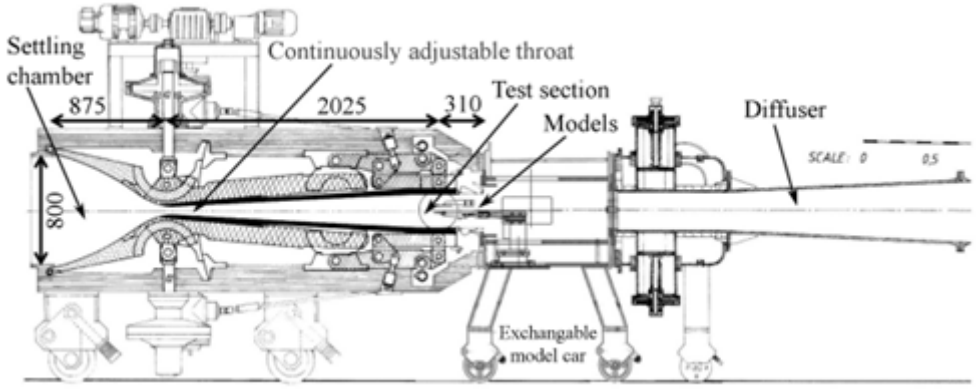

Figure 3.2: TST 27 configuration schematic (from Giepman [16])

Schlieren visualizations were employed to capture the flow structures and shock interactions during the experiments, utilizing a Z-type optical configuration very similar to the one depicted in Figure 3.3. This setup allows for a clear identification of the main structures of the flow: shock waves and expansion waves, several indicators of boundary layer separation and reattachment (through the separation- and reattachment shockwaves), and other relevant flow phenomena. Further details on the working principles, advantages, and specific implementation of Schlieren visualization techniques will be discussed in Chapter 4, where flow visualization methods are examined in depth. For now, the focus remains on describing the experimental setup and test conditions.

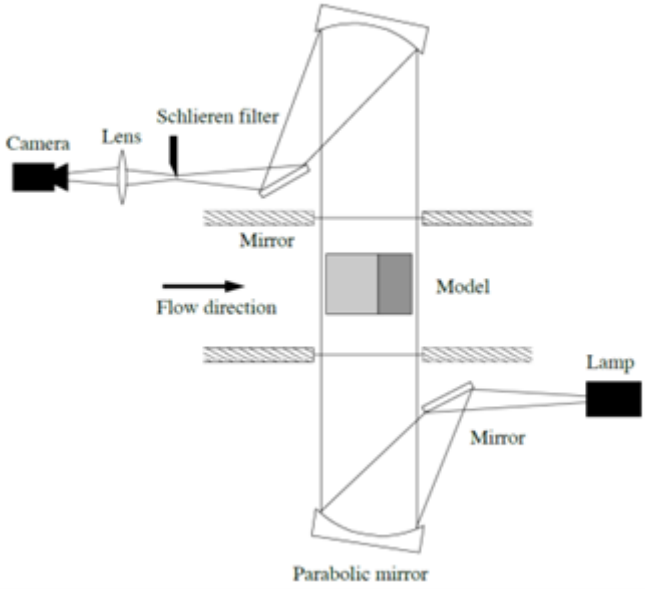

Figure 3.3: Z-type Schlieren configuration (from Schrijer [40])

The physical arrangement of this setup is presented in Figure 3.4.

(a) side 1 – "bottom" of the Z configuration in Figure 3.3

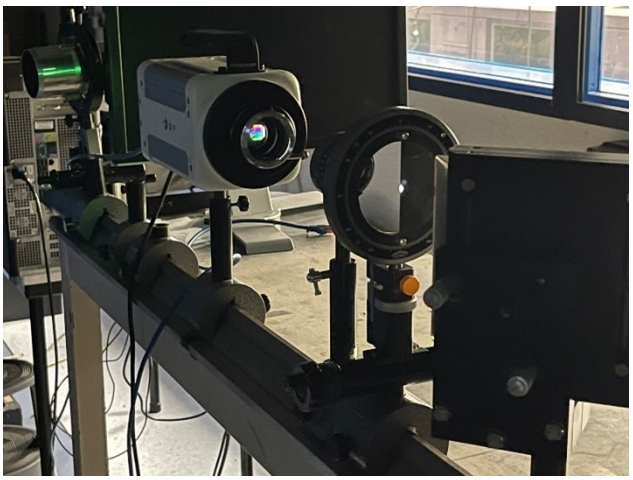

(b) side 2 – "top" of the Z configuration in Figure 3.3

Figure 3.4: Schlieren configuration setup

3.2 Wind tunnel model

As stated in the literature review and the research questions, one of the main objectives of these experiments is to investigate the key mechanisms driving the low-frequency unsteadiness observed in the work of Nel et al. [7][9][10], the same experimental setup was used. This includes the flat plate model originally employed in the Ph.D. research of Rogier Giepman [16], along with various shock generators with large wedge angles (17°– 22°) designed to induce a strong interaction, resulting in a massively separated OSBLI under different test conditions.

The test section, as depicted in Figure 3.5, features an optical access window, made of special glass, allowing for Schlieren visualization of the flow. Both the flat plate and shock generator are securely mounted to the wind tunnel sidewalls using metallic supports, which are fixed in place via eight screws to ensure stability throughout the test runs.

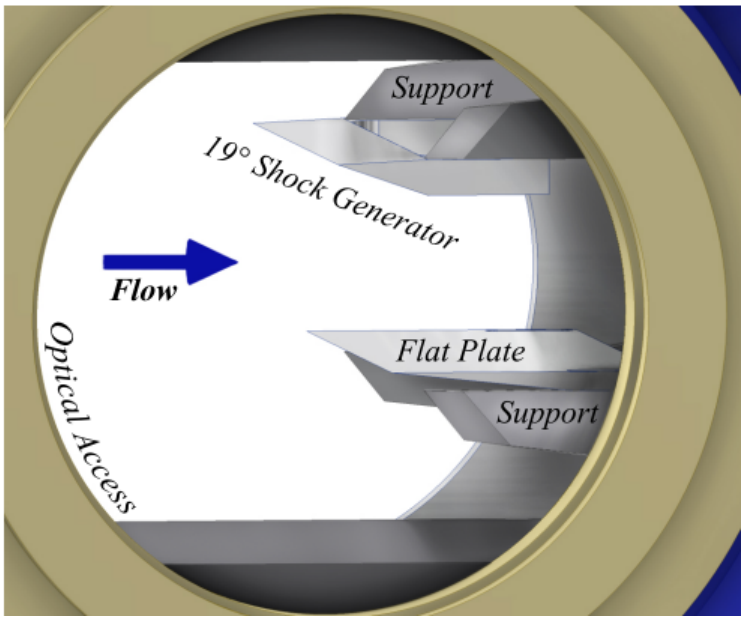

Figure 3.5: Shock generator and flat plate setup - adapted from Nel et al. [9]

A description of the dimensions for the flat plate and shock generator inside the wind tunnel is provided in Figure 3.6. The dimensions are given in millimeters (mm), and they are relevant when estimating the theoretical impingement point of the oblique shock which forms at the leading edge of the shock generator. This value is important when computing the Re_x.

The height of 78.25 mm between the shock generator and flat plate is fixed; in the TST 27, the following two are possible height positions for the shock generator (the top mount): the one depicted in Figure 3.6a (78.25 mm) and 30 mm. The latter, however, is too low, and an unstart of the wind tunnel would occur for any test.

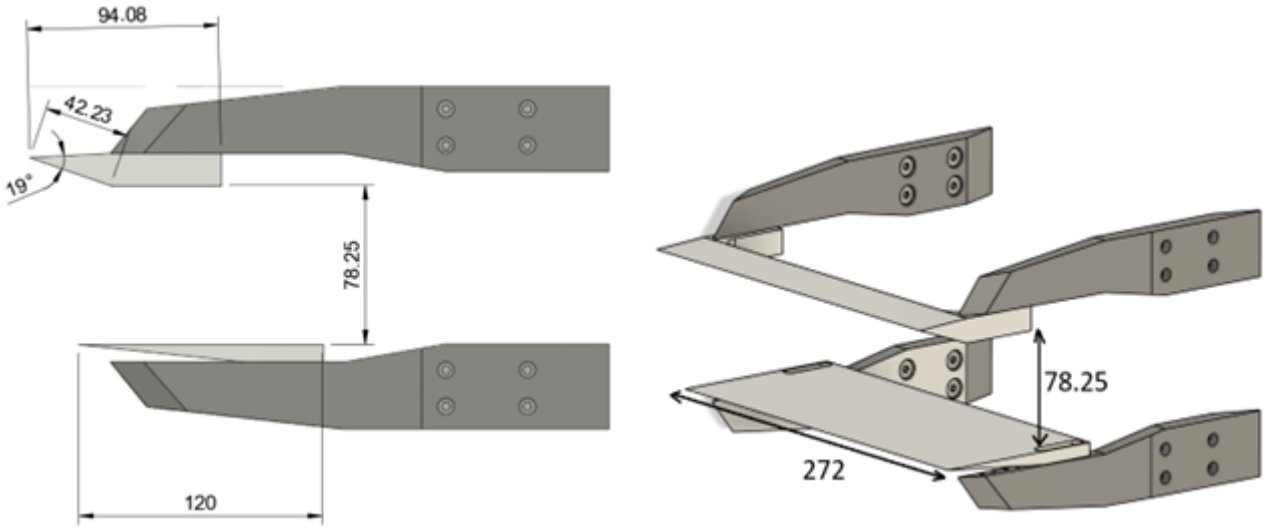

(a) side view **(b)** isometric view

Figure 3.6: Dimensions of the wind tunnel model with the 19°shock generator

Therefore, in all the tests performed, the two components were mounted at the same position (i.e., the one in Figure 3.6a). Finally, Figure 3.7 shows the physical setup with the Schlieren setup defocused in the foreground and the optical view of the flat plate and shock generator configuration inside the wind tunnel in the background.

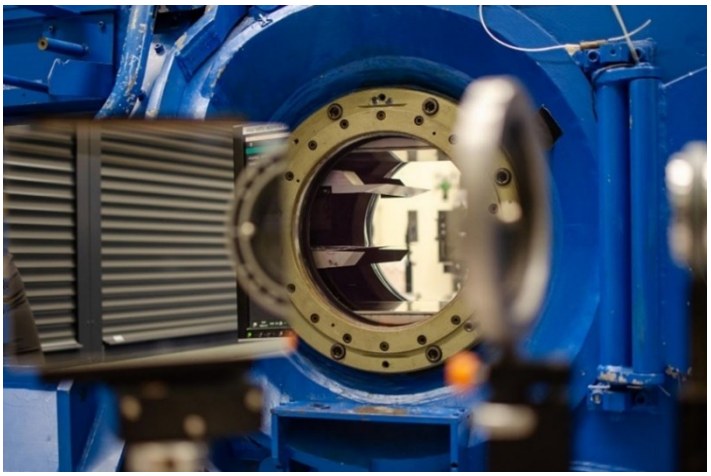

Figure 3.7: Flat plate and shock generator configuration in the TST 27

3.3 Addition of the 2D step

One other research topic of interest was to investigate how the interaction changes when (passive) flow control systems are added. Because of its simplicity and ease of use, a 2D step made of thin aluminum tape (the thickness of one layer is 60 microns) was used and applied on the flat plate as shown in Figure 3.8. The tape was cut in strips of 1.3mm width and applied 3mm from the leading edge.

A reasonable justification for placing the 2D step at this distance from the leading edge can be linked to the maximum upstream position of the laminar separation shockwave, which was observed at x=10 mm in prior tests (Nel et al. [9]). Given that lower Mach numbers tend to shift the interaction further upstream when not changing the position of the flat plate or shock generator, it is necessary to ensure that the step is positioned well ahead of the expected separation region in order to influence the early stages of boundary-layer development. While no prior and definitive calculation was made to fully justify this x = 3 mm positioning, it was considered that the setup accounts for cases where the shock moves even closer to the leading edge, ensuring that its effect is felt across a range of conditions.

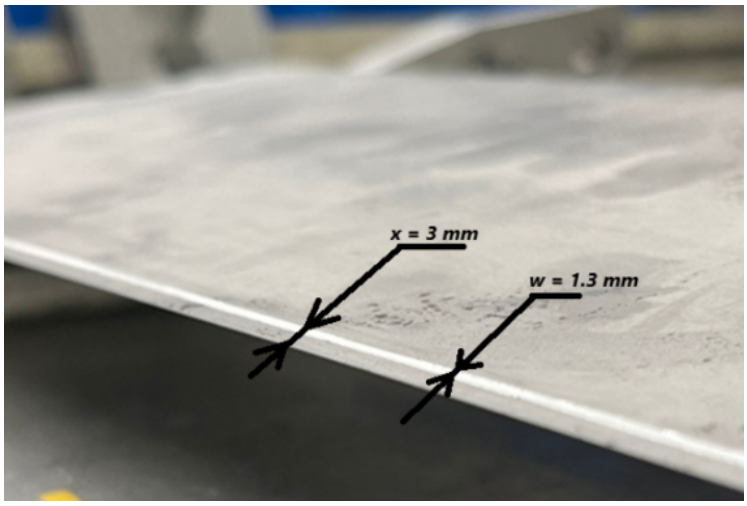

Figure 3.8: 1 layer (60 microns) of 2D step added to the flat plate

The way in which this 2D step height can be increased is by simply adding more layers of the same aluminum tape on top of each other. For instance, Figure 3.9 depicts the flat plate with 3 strips of aluminum tape (for a total of 180 microns) mounted in the TST 27.

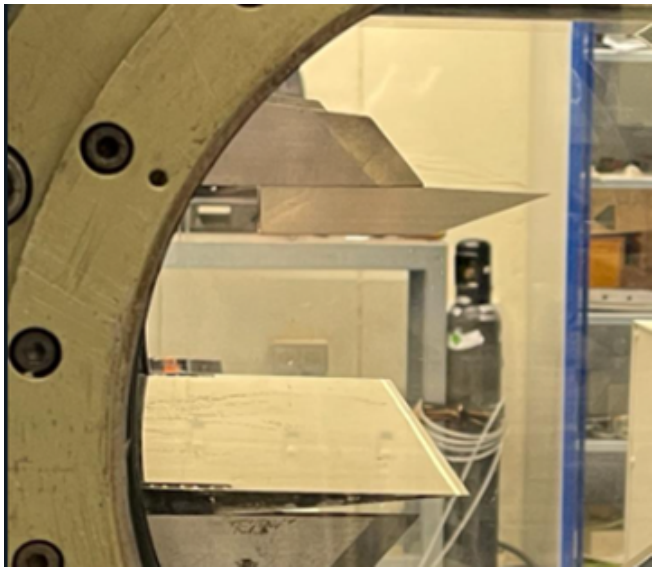

Figure 3.9: Flat plate with 3 layers (180 microns) of 2D step, mounted in the wind tunnel

3.4 Measurement conditions

Conceptualizing the test matrix starts with understanding two key points:

- What we want to observe in our tests: a periodic oscillation of the laminar separation shockwave in the context of a transitional OSBLI; and to see which "ingredients" facilitate this mechanism).
- What variables we can control in our tests: the experimental parameter space (we control the geometry of the configuration and the wind tunnel starting conditions).

We will begin the explanation starting from the latter. When setting up the experiments, we are aware of the geometry of the flat plate and shock generator(s) (depicted in Figure 3.6). This geometry dictates the shock impingement location (denoted "x" in mm) and whether or not the wind tunnel experiences an unstart (a more extensive discussion on this follows later on). However, as mentioned before, the positioning of the flat plate and shock generator remained the same throughout the tests. The main variables that can still be adjusted are:

- The Mach number (by adjusting the throat area of the wind tunnel);
- The total pressure in the wind tunnel (more precisely, in the settling chamber, see Figure 3.2);
- The wedge angle of the shock generator.

Each of these directly affects either the Reynolds number calculated at the theoretical impingement point "x" or the inviscid pressure jump. The Reynolds number is a dimensionless variable that can be used to describe the state of the boundary layer at a certain point, while the inviscid pressure jump is a means to describe the "shock strength", or the intense adverse pressure gradient imposed on the boundary layer, which subsequently causes it to separate.

The calculation of the Reynolds number starts with Equation 3.1:

$$Re_x = Ma \frac{\sqrt{\gamma R T} x}{\nu} \tag{3.1}$$

It is already clear how the Mach number (directly in the equation, but also influences x) and the wedge angle (influences the impingement location x) affect Re_x. However, a further clarification on how this Reynolds number is calculated also shows the degree in which the total pressure variable influences it. For now, in Equation 3.1, the following are considered "known": the Mach number; the parameter x, the specific heats ratio γ, and the gas constant $R = 287\ J/kgK$. The free stream temperature is computed using the isentropic relation:

$$T = T_T \left(1 + \tfrac{\gamma-1}{2} Ma^2\right)^{-1} \tag{3.2}$$

Where the total temperature, T_T, was previously defined as being 288 K. Finally, the freestream dynamic viscosity is obtained from the following sequence:

$$\begin{cases} \rho_T = \dfrac{p_T}{R\,T_T} \\ \rho = \rho_T \left(1 + \tfrac{\gamma-1}{2} Ma^2\right)^{-\frac{1}{\gamma-1}} \implies \nu = \dfrac{\mu}{\rho} \\ \mu = \mu_0 \left(\dfrac{T}{T_0}\right)^{\frac{3}{2}} \dfrac{T_0 + S_\mu}{T + S_\mu} \end{cases} \tag{3.3}$$

The first relationship in Equation 3.3 proves the role that the variable p_T has in determining the Reynolds number of the flow at point x. Furthermore, according to the oblique shock relations[3], and maintaining the numbering convention from before:

$$\frac{p_2}{p_1} = \frac{2\gamma Ma^2 \sin^2\beta - (\gamma - 1)}{\gamma + 1} \tag{3.4}$$

Figure 3.10 is an adaptation of the previous schematic shown in Chapter 2 when discussing shock polars, but now has the added β angle which appears in Equation 3.4.

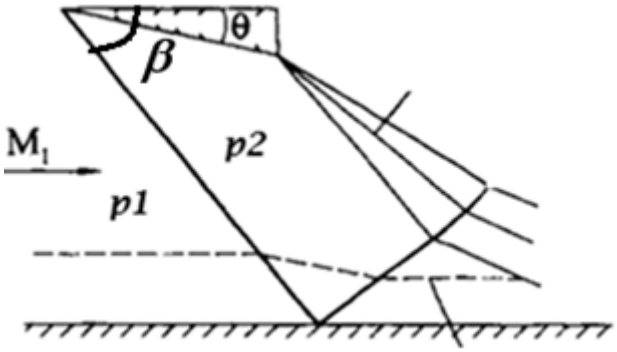

Figure 3.10: Inviscid shockwave reflection - adapted from Ben-Dor et al. [34]

Because the angles of the separation bubbles are not known a priori, it is difficult to estimate the pressure rise over the whole interaction since that requires also knowing the β angles resulting from the separation shockwave. Therefore, in the test matrix, this inviscid pressure rise (only using the incoming Mach number and the defined shock generator angle) is used to characterize the "shock strength".

After analyzing which variables affect what, one can notice the advantage of using this type of blowdown supersonic wind tunnel with variable total pressure: because p_T only affects the Reynolds number and not the shock strength (at least directly), an investigation can be performed on the Reynolds number effect in isolation, with the other parameters remaining the same.

We now return to the first point mentioned with regards to the "physical" mechanism investigated. The experiments were based on a known "baseline" condition—Mach 2.3, total pressure (p_T) of 2.8 bar, and a 19-degree shock generator—under which a particular shock oscillation phenomenon (involving a low-frequency oscillating laminar separation shockwave) was already observed. To visualize the exact physical mechanism that was researched, refer to Figure 5.1 in Chapter 5. In setting up the new tests, the first task was to replicate this baseline scenario using high speed Schlieren.

Next, the plan was to explore whether this shock oscillation mechanism would also be observed under different variable settings (i.e., changing geometry/Mach number/total pressure from the ones in the "baseline" case) but maintain similar Rex and/or inviscid pressure jump. The goal was ultimately to notice if the same, or a similar oscillation mechanism such as the one presented in the Results section, Figure 5.1. Another aspect was to notice if, in those cases, one notices the appearance and of a Mach stem. One of the necessary conditions was to pre-calculate the Re_x such that its value corresponded to one in the transitional region as found by Giepman [16].

Because the shock separation angles could not be determined beforehand, there was no way to anticipate (by use of shock polars) if a Mach stem would appear or not. Without another tool such as CFD simulations, the only way to verify if the shock oscillation mechanism of interest would develop was to physically run the tests and observe the Schlieren results "in real time".

[3] https://www.grc.nasa.gov/www/k-12/airplane/oblique.html

The chosen option in developing the test matrix was the following: for each test run, the Mach number, total pressure, and wedge angle were chosen such that they matched either the baseline Re_x or the inviscid pressure jump (it was hard to manipulate both at the same time) as closely as possible. If the wind tunnel "unstarted" under those conditions (meaning the flow could not establish a stable supersonic state), the total pressure was gradually increased in increments of 0.1 bar until the tunnel started.

During each successful run (when the tunnel started), the live Schlieren recordings were observed to see if the laminar separation shockwave would travel upstream, collapse, and repeat, in a pattern similar to the baseline test. Consistency in the amplitude and rate of these shock movements was important: a stable, repetitive oscillation with no unexpected instabilities signified that the new test conditions produced a similar fundamental mechanism as before.

Besides the clear oscillation mechanism noticed in the baseline case, two other situations were observed during the test. Again, for reference and more information on the exact the physical mechanism observed, the reader is referred to the Results section (particularly Figure 5.1, Figure 5.3 and Figure 5.4).

To conclude, the experiments were done in such a way as to capture one of the three mechanisms identified so that they can later be compared and analyzed.

3.5 Limitations and constraints of the wind tunnel

The unstart problem of the wind tunnel is very well explained in the Master's thesis of Patterson [41]: In a blowdown supersonic facility, the flow accelerates from rest to supersonic conditions through a sequence of sections—including a settling chamber, a convergent-divergent nozzle, a test section, and a diffuser—driven by the pressure difference between the high-pressure chamber and the diffuser exit at ambient conditions. As the tunnel starts, a normal shock generated at the nozzle throat travels downstream through these sections, which is only possible if total pressure losses stay within acceptable limits and the test section can handle sufficient mass flow around any installed model. The phases through which the shock goes through during startup is depicted in Figure 3.11.

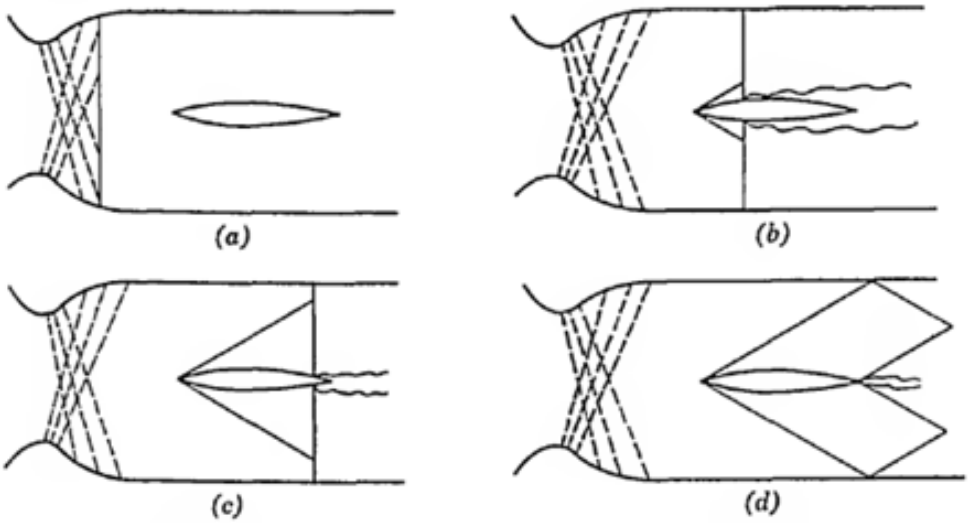

Figure 3.11: The phases of the normal shock during the start of a blowdown supersonic wind tunnel (Pope and Kennith [42])

When it comes to the total pressure losses "staying within acceptable limits", there is a significant total pressure drop during startup across the traveling normal shock, and it is estimated that the pressure remains

needs to be above about 1.6 bar in TST-27 to overcome back pressure in the diffuser and sustain supersonic flow (Patterson [41]). Once the tunnel transitions to steady state, compression is mostly done by oblique shocks, minimizing total pressure losses and preventing an unstart of the system. The total pressure after the normal shock is defined by the following relationship[4]:

$$p_{t1} = p_{t0} \left(\frac{(\gamma+1)\,Ma^2}{(\gamma-1)\,Ma^2+2} \right)^{\frac{\gamma}{\gamma-1}} \left(\frac{\gamma+1}{2\gamma\,Ma^2-(\gamma-1)} \right)^{\frac{1}{\gamma-1}} \tag{3.5}$$

This result has to be above the aforementioned value of 1.6 bar.

The second part, the "mass flow requirement", states that, during startup, the test section must accommodate a high enough mass flow to allow the normal shock to pass on downstream—something that can become complicated by a full-span model such as the one used in this experiment that restricts the effective cross section (and effectively acts as a convergent duct). Since the flow is subsonic after the shock and is forced through a convergent duct formed by the wedges, it can choke before the throat if Mach 1 is reached prematurely, preventing the shock from passing and causing the tunnel to fail to start (Patterson [41]).

The critical area ratio is calculated the same as in the formula for a (convergent-)divergent duct in the book "Fundamentals of Aerodynamics" of Anderson [35]:

$$\frac{A}{A^*} = \frac{1}{Ma_1} \left[\frac{2}{\gamma+1} \left(1 + \tfrac{\gamma-1}{2} Ma_1^2 \right) \right]^{\frac{\gamma+1}{2(\gamma-1)}} \tag{3.6}$$

In Equation 3.6, A represents the inlet area of the convergent duct, $A*$ represents the critical area of the duct (where the flow reaches $Ma = 1$), and Ma represents the Mach number after the normal shock during the startup. The necessary condition for the shock to pass is that the area A is equal or larger than $A*$.

Using the known dimensions of the shock generator and the flat plate (Figure 3.6a), one can calculate the necessary height required between the two components. However, this is not necessary anymore, since as explained before, this height is fixed at 78.25 mm.

Through the normal shock relations, this Ma_1 can be computed as a function of the steady state Mach number Ma:

$$Ma_1 = \left(\frac{1 + \frac{\gamma-1}{2} Ma^2}{\gamma\,Ma^2 - \frac{\gamma-1}{2}} \right)^{\frac{1}{2}} \tag{3.7}$$

Finally, as very well explained by Patterson [41], after the mass flow rate condition is achieved and the tunnel runs in steady operation, the following problem can still arise: if the height between the two components is too low, the forming shocks could impinge on the wedge or trailing-edge expansion fans that cross the interaction point, which can lead to unstart or disrupt the shock-shock interaction, so the geometry must be carefully chosen to avoid these conditions.

The "problems" that arose are summarized in Figure 3.12:

- in subfigure a), the tunnel unstart due to the total pressure/mass flow rate conditions not being satisfied;
- in subfigure b), the tunnel unstart due to impingement of the reflected shocks on the wedges (in this situation, the height chosen was the lower 30 mm, which proved to be too low for any scenario;
- in subfigure c), if the Mach number was too low (or the shock generator angle too high), the oblique shock would impinge too far upstream which caused a "spillover" of the boundary layer over the

[4] https://www.grc.nasa.gov/www/k-12/airplane/oblique.html

leading edge. Mitigating this would mean either moving the flat plate more upstream (but it was already at maximum upstream physical position) or moving the shock generator further downstream (it was already at almost full "downstream" position)

- in subfigure d), if the Mach number was too high (or the shock generator angle too low), the wave angle would also lower and cause the shock to impinge very far downstream. While this does not initially seem to be a problem, since it was just mentioned that we could move the plate more downstream, it would still cause the interaction to be "out of frame" and the whole details could not be captured.

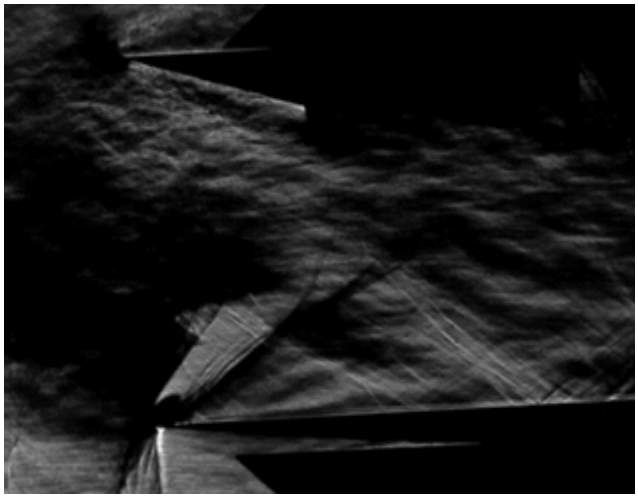

(a) tunnel unstart due to insufficient mass flow rate

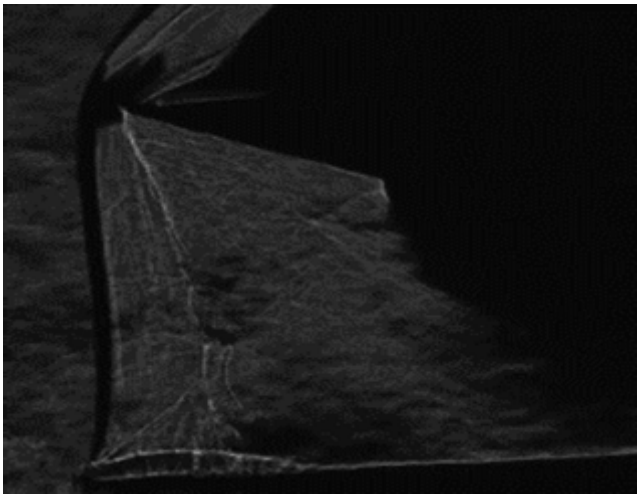

(b) tunnel unstart due to very low height between the shock generator and flat plate (impingement of the reflected shock on the wedges)

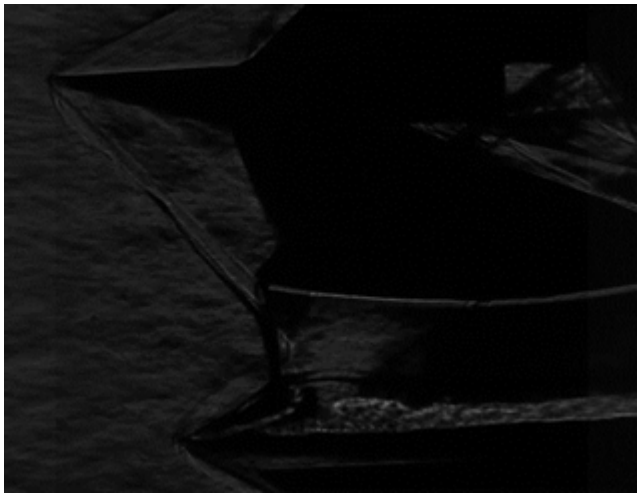

(c) too low Mach number – steep angle

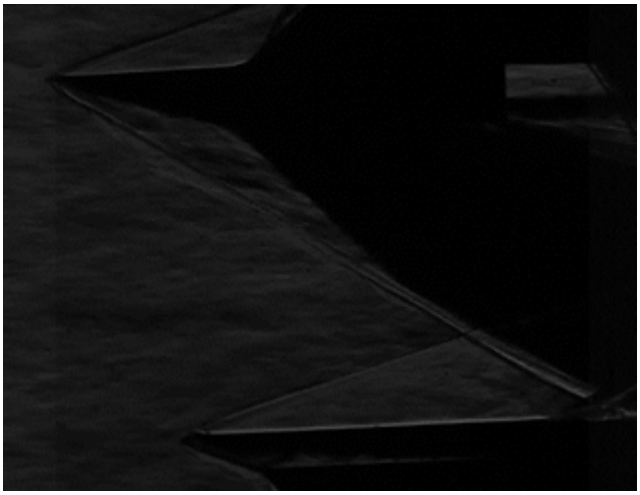

(d) too high Mach number – shallow angle

Figure 3.12: Constraints that appeared during testing

As a result, and as previously noted, the height and position of the shock generator and flat plate remained fixed, so the only thing that could be done is to analyze the chosen Mach number and total pressure pt and introduce these variables in Equation 3.4, then check if they satisfy the condition for startup. In other words, all that could be done is to just "have an idea"/predict whether an unstart would occur or not.

Because of the strength of the interaction and the rising shear layer which adds additional height to the flat plate and further complicates the calculations, we could not precisely predict whether an unstart would occur or not, so the final decision was to still perform the tests as planned, even though an unstart of the wind tunnel was possible.

Another consideration that has to be taken into account is the expansion wave that forms at the shoulder of the shock generator, which can impinge onto the incoming oblique shockwave and affect its strength. This phenomenon will be much more visible in Chapter 4, where different knife edge setups for the Schlieren configuration are shown. Depending on the Schlieren knife edge sensitivity to density gradients, different position can highlight certain aspects of the flow, including this expansion wave that forms.

While on the topic of interference effects that can affect the OSBLI which is studied, it is important to recall that the 3D effects from the sidewalls can also induce further compression (as in Figure 3.13) or expansion waves (depending on the location) which can alleviate or worsen the interaction. Again, for the scope of this thesis, they were not included as calculations (or their specific effect on the interaction was not taken into account since there would need to be a sidewall boundary layer study to see the positions of the compression waves), but they are kept in mind.

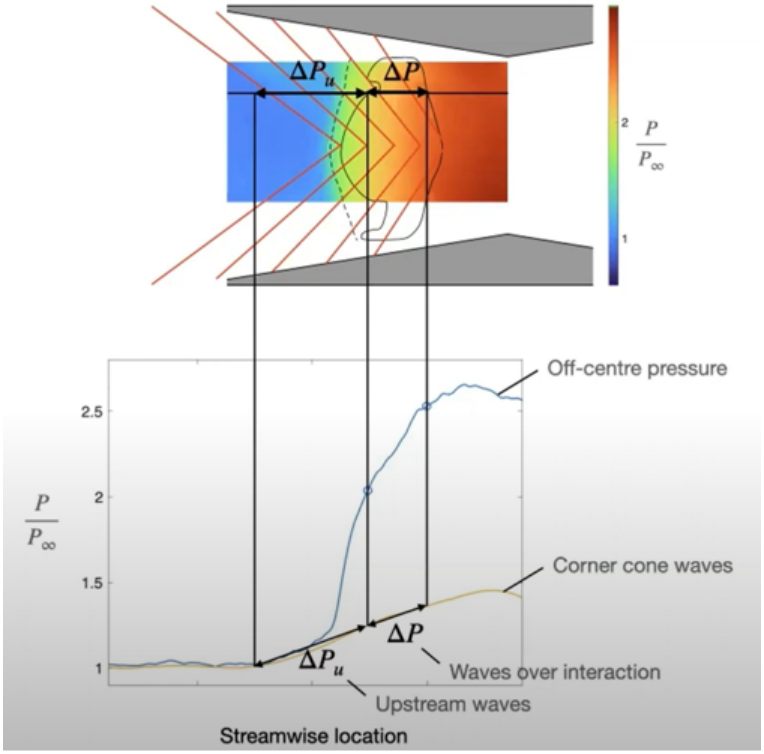

Figure 3.13: 3D wall effects affecting the OSBLI (Missing & Babinsky [43])

3.6 Test matrix

The final test matrix is presented in Table 3.1. The rubrics it contains and their relevance were all explained previously in this section. A few further clarifications can be made to fully explain its contents:

- The column "$\theta - x$" represents the turn angle of the shockwave (17°, 19°or 22°), and the "x position of the flat plate". In rows 2-3 and 5-6, the mention "(-2cm x)" is added to signify that the flat plate was moved 2 centimeters downstream to accommodate for the problem that appeared in Figure 3.12d), however this idea was abandoned after the first few tests and the configuration remained fixed to the position in Figure 3.6.
- "Observation": includes the three scenarios that were presented before and depicted in the Results section: "desired oscillation", "low amplitude oscillation)", "very low amplitude oscillation)".
- "Inviscid pressure jump": "shock strength" calculated using Equation 3.4.

Nr.	Ma	p_T [bar]	Re_x ($\cdot 10^6$)	$\Theta - x$	Observation	Inviscid pressure rise
1	2.3	2.8	2.055	19°	Started (Baseline)	2.878
2	2.3	2.1	2.179	19°(− 2 cm x)	Not started	2.878
3	2.6	3	3	19°(−2 cm x)	Not started	3.143
4	2.8	3	2.987	19°	Not started	3.35
5	2	2.8	2.376	19°(−2 cm x)	Not started	2.7
6	2	2	1.7	19°(−2 cm x)	Not started	2.7
7	2.3	2.6	2.01	19°	Low oscillation amplitude	2.878
8	2.3	2.4	1.83	19°	Not started	2.878
9	2.3	2.5	1.91	19°	Low oscillation amplitude	2.878
10	2.3	2.3	1.76	19°	Not started	2.878
11	2.3	3	2.295	19°	Desired oscillation	2.878
12	2.3	3.4	2.602	19°	Low oscillation amplitude	2.878
13	2.3	4	2.977	19°	Low oscillation amplitude	2.878
14	2.3	4.2	3.22	19°	Very low oscillation amplitude	2.878
15	2.8	2.6	2.18	19°	Not started	3.35
16	2.8	3	2.516	19°	Not started	3.35
17	2.8	4	3.354	19°	Out of bounds	3.35
18	2.6	2.6	2.18	19°	Not started	3.143
19	2.6	3	2.45	19°	Not started	3.143
20	2.6	3.2	2.64	19°	Very low oscillation amplitude	3.143
21	2.6	3.4	2.79	19°	Very low oscillation amplitude	3.143
22	2.5	2.7	2.2	19°	Not started	3.05
23	2.5	2.8	2.325	19°	Not started	3.05
24	2.5	2.9	2.4	19°	Low oscillation amplitude	3.05
25	2.0	3.4	2.12	19°	Low oscillation amplitude	2.69
26	2.5	3.1	2.57	19°	Low oscillation amplitude	3.05
27	2.4	2.8	2.18	19°	Low oscillation amplitude	2.96
28	2.4	2.7	2.2	19°	Low oscillation amplitude	2.96
29	2.4	2.5	2.0	19°	Not started	2.96
30	2.4	2.6	2.118	19°	Not started	2.96
31	2.1	2.8	1.94	19°	Out of bounds	2.74
32	2.1	3.0	2.08	19°	Out of bounds	2.74
33	2.1	3.2	2.21	19°	Out of bounds	2.74
34	2.2	2.9	2.17	19°	Very low oscillation amplitude	2.80
35	2.2	2.7	2.0	19°	Low oscillation amplitude	2.80
36	2.2	3.1	2.3	19°	Very low oscillation amplitude	2.80
37	2.2	2.6	1.946	19°	Low oscillation amplitude	2.80
38	2.2	2.5	1.871	19°	Low oscillation amplitude	2.80
39	2.6	2.4	2.262	17°	Not started	2.82
40	2.6	3.0	2.83	17°	Not started	2.82
41	2.6	3.1	2.922	17°	Out of bounds	2.82
42	2.5	2.9	2.71	17°	Out of bounds	2.75
43	2.5	2.7	2.526	17°	Not started	2.75
44	2.4	2.7	2.488	17°	Low oscillation amplitude	2.67
45	2.4	2.5	2.3	17°	Not started	2.67
46	2.4	2.6	2.396	17°	Not started	2.67
47	2.3	2.6	2.21	17°	Desired oscillation	2.60
48	2.3	2.5	2.249	17°	Low oscillation amplitude	2.60
49	2.4	2.8	2.48	17°	Low oscillation amplitude	2.60
50	2.1	2.2	1.792	17°	Unstable due to being close to unstart	2.48
51	2.4	2.8	1.89	22°	Desired oscillation	3.45
52	2.6	3.4	2.41	22°	Low oscillation amplitude	3.67
53	2.7	3.6	1.78	22°	Very low oscillation amplitude	3.79
54	2.7	3.8	1.81	22	Very low oscillation amplitude	3.79

Table 3.1: Test matrix

Chapter 4

Flow Measurement and Post-Processing Techniques

Schlieren visualizations were used during testing, as presented in Chapter 3. The notion of "high speed Schlieren" relates to the fast acquisition rate of the selected camera, the Photron FASTCAM NOVA S12, with an acquisition rate of 80 kHz and a resolution of 512 × 256 pixels at a shutter speed of 1/150.000s) to capture the movement of the oscillation system: of the separation bubble, the reflected shock, and the separation shock.

Schlieren visualizations are based on being able to relate changes in refraction (through the gradient of the refractive index n, as opposed to shadowgraphy, which measures changes in the second derivative of the refractive index) to changes in density, as explained by Settles [44]. It can also be used as a tool to measure quantitative density variations according to Eslinga et al. [45], but mostly (also for the purpose of this thesis) it provides (quick) qualitative data of the flow, including to see if the tunnel is started or not. The basic working principle is dependent on the light refraction in a medium with a different speed of light than in vacuum:

$$n = \frac{c_0}{c} = 1 + K\rho \tag{4.1}$$

Where K is the Gladstone-Dale constant (known) and ρ represents the air density. The curvature of a light ray when it is refracted can be expressed for the two directions (the direction of light propagation z and the perpendicular plane xy):

$$\begin{cases} \dfrac{\partial^2 x}{\partial z^2} = \dfrac{1}{n}\dfrac{\partial n}{\partial x} \\ \dfrac{\partial^2 y}{\partial z^2} = \dfrac{1}{n}\dfrac{\partial n}{\partial y} \end{cases} \tag{4.2}$$

Which ultimately leads to the identification of the deflection angle of the light ray:

$$\begin{cases} \epsilon_x = \dfrac{1}{n}\displaystyle\int \frac{\partial n}{\partial x}\, dz \\ \epsilon_y = \dfrac{1}{n}\displaystyle\int \frac{\partial n}{\partial y}\, dz \end{cases} \tag{4.3}$$

Therefore, a light ray is deflected in the direction of increasing refractive index (density), and the Schlieren setup defined in the previous chapter can be used to capture the density gradients associated with aerodynamic phenomena such as shockwaves and expansion waves. Schlieren visualizations can therefore reveal the overall wave structure by highlighting areas of density gradient, which can further be used to measure the interaction length(s). In this particular setup, that distance spans from the average reflected shock foot to the primary shock's inviscid impingement point. This length serves as the basis for computing the Strouhal number (together with the frequencies associated with the unsteady shock behavior). This method of choosing the Strouhal number, with the frequency of the shock behavior, the freestream velocity, and the interaction length as defined before has been shown to collapse unsteadiness frequencies from different types of interactions to similar values, as mentioned in Dupont et al. [31].

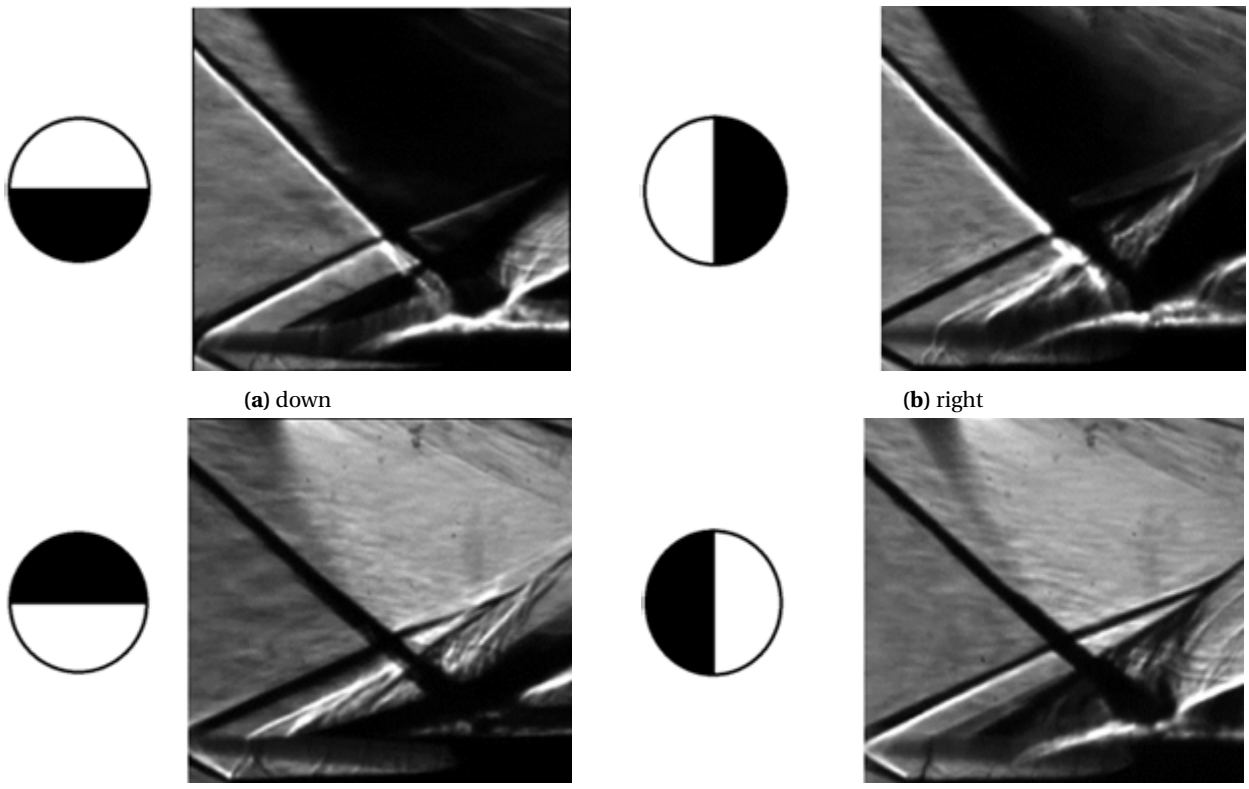

(a) down **(b)** right

(c) up **(d)** left

Figure 4.1: Effect of the knife edge placement

In a Schlieren setup, a parabolic mirror collimates light from a point like source, and a second mirror then focuses it onto a knife edge, where density-induced deflections show up as bright or dark areas. Although an infinitely small pinhole would make the system extremely sensitive, a “moderate” pinhole size is chosen to avoid oversensitivity and maintain a practical measurement range. The choice of the knife edge position depends on how well we can view the flow structures. Four possible choices were selected and are depicted in Figure 4.1.

Subfigures a) and b) are interesting because they highlight the interference of the expansion wave stemming from the shoulder of the shock generator (the dark fan-like structure) with the impinging shockwave. This is one of the considerations that has to be kept in mind, because it affects the overall interaction, but no way of mitigating it/taking it into consideration was found apart from acknowledging it. However, as can be noticed, it “masks” the downstream features, including the reflected shockwave, which makes this setup unsuitable in the analysis.

Figure 4.2: Configuration of the knife edge for the tests

Thus, it was decided that the knife edge setup from Figure 4.1d provides the best view of all the components in the system: the impinging shock, the reflected shock, the growing shear layer and the reattachment shockwave.

Bringing into context the conclusions from before, the final high speed Schlieren configuration chosen is shown in Figure 4.2. In the right-hand side of the image, the last element is the high acquisition rate camera, the Photron FASTCAM NOVA S12.

4.1 Spark light Schlieren

Besides using a continuous light source such as in the high speed Schlieren, the so-called "Spark light Schlieren" system can be used in which a light source generates short pulses (20 ns) that can "freeze" the flow in the recording and capture several instantaneous features of the flow. This can be used to analyze the natural transition of the boundary layer (not the scope of this thesis) and to identify the structures of the boundary layer ahead of the OSBLI (will be particularly useful when looking at the comparison with the 2D steps).

The setup for the spark light is depicted in Figure 4.3. Instead of a continuous light source, a pulsating command is given by the control terminal (left side of the figure), and the image is captured using a BOBCAT camera (right side) with an acquisition rate of 5 Hz.

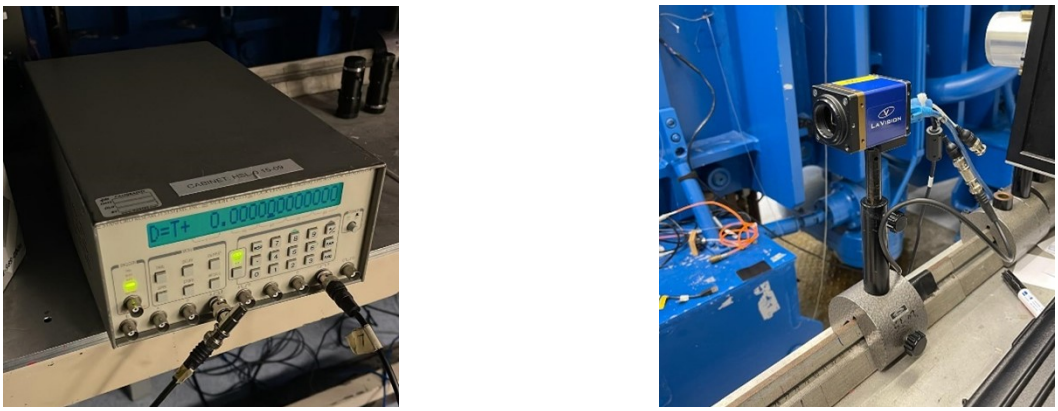

Figure 4.3: Spark light Schlieren setup

4.2 Post-processing methodology and code

The outputs of the Schlieren visualizations are a succession of frames in ".tiff" files that are captured at a very high acquisition rate (around 170.000 files for a 2.5 second recording). These .tiff files are matrices that contain values that describe the light intensity captured. It is natural to understand that, when a sudden jump in these values happens, it is indicative of a flow structure being encountered (for example, a shockwave).

These matrices can further be manipulated using matlab and several qualitative and quantitative outputs can be obtained, such as for calculating mean and standard deviation images.

Matlab calculates the mean intensity of each pixel over the whole set of frames. Physically, this represents the time-averaged flow field. It highlights the stationary or slowly varying features of the flow, by showing the average intensity values corresponding to where shock waves and other areas of varying density occur. The obtained result is depicted in Figure 4.4a, where one can also notice that, by using the gradients of the pixels, the shock foot and impingement point can be computed and the relevant lengths determined.

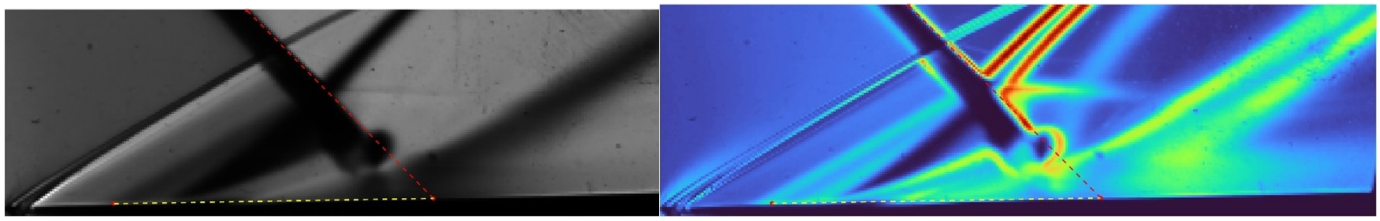

(a) mean image **(b)** standard deviation

Figure 4.4: Mean and standard deviation image of a test case: Ma = 2.3, p_T = 2.8 bar, 19°s.g

Furthermore, for the standard deviation image, matlab calculates the standard deviation of the intensity values of each pixel across all frames. Physically, it highlights regions where there is significant temporal variation in the flow. A "high std value" in a pixel would mean that the intensity value of that pixel varies greatly over time compared to the mean. In Schlieren imaging, as explained before, this variation is due to large changes in the refractive index gradients caused by density fluctuations in the flow. It effectively highlights areas of unsteady flow phenomena which can help us analyze the dynamics of the SBLI.

Because it uses a color scale to indicate the magnitude of the standard deviation, it is easier to follow than the image of the mean. In Figure 4.4b, we notice some prominent features:

- Upstream, where the laminar separation shockwave oscillates, there is a blueish-green tint more visible at the "extremities" of its amplitude, and not necessarily in-between. The stronger/higher tint at the upstream positions are an indicator of more unsteadiness close to the region where the shock vanishes (it doesn't always vanish at the same point upstream). The same phenomenon can explained for the region more downstream; the transition region, just before the turbulent shockwave, also doesn't always happen at the same point. In-between these two areas, the flow features may be more stable.
- The region of the reflected shockwave has the highest color intensity (i.e., the highest values for the standard deviation). Due to the mechanism of the separation bubble breathing, the upstream disturbances, and the separated flow region (all of which are estimated to exacerbate the effects in a highly separated transitional interaction), the reflected shock is more unsteady than the other elements in the flow.

The "std" image is useful because it can be used to complement the frequency analysis done using the Fast Fourier Transform (FFT) and the Power Spectral Density (PSD) analysis:

- The standard deviation image quantifies the overall variability/unsteadiness of the pixel intensity, integrating contributions from all frequencies present in the signal.
- The FFT/PSD decomposes the intensity time series at a specific pixel/line into its constituent frequencies, revealing how much each frequency contributes to the overall signal; then, what one sees in a standard graph containing the power spectral density is the amplitude/power density associated with each frequency component in the signal.

Moving forward, it was mentioned that these resulting images allow us to perform some length measurements in order to identify the lengths which will subsequently be used in the frequency/Strouhal analysis. The procedure to calculate the interaction length is as follows:

- The first point belonging to the shock foot of the separation shockwave is identified by calculating the largest gradient in the area of the shock foot of the frames;
- The second point (the theoretical "inviscid" impingement point of the oblique shock) has a more complex calculation algorithm: it is found by identifying the intersection point of the line belonging to the flat plate and a line defined by two points of the impingement shock (these two points are again calculated by taking the maximum gradient around the area of the impinging shock, which indicates its presence).

4.3 Frequency and Power Spectral Density Analysis

The FFT/PSD analysis for several features of the flow starts by selecting a line that crosses relevant areas in the frame (like in Figure 4.5: the laminar separation shock, the impinging shock, the reflected shock, the shear layer), and tracking the location of the highest gradient throughout the sequence of frames. Once this vector of locations is identified, the matlab function "pwelch" runs a power spectral density analysis using a Hamming window and 50% overlap in the calculations. The subtraction of the mean has to be done by the user, otherwise there will be a large peak belonging to the mean value at 0 Hz.

Note that, in Figure 4.5, the flat plate appears to be a bit "slanted" due to the camera orientation. The position and orientation of the setup was taken into account when performing the post-processing of the figures.

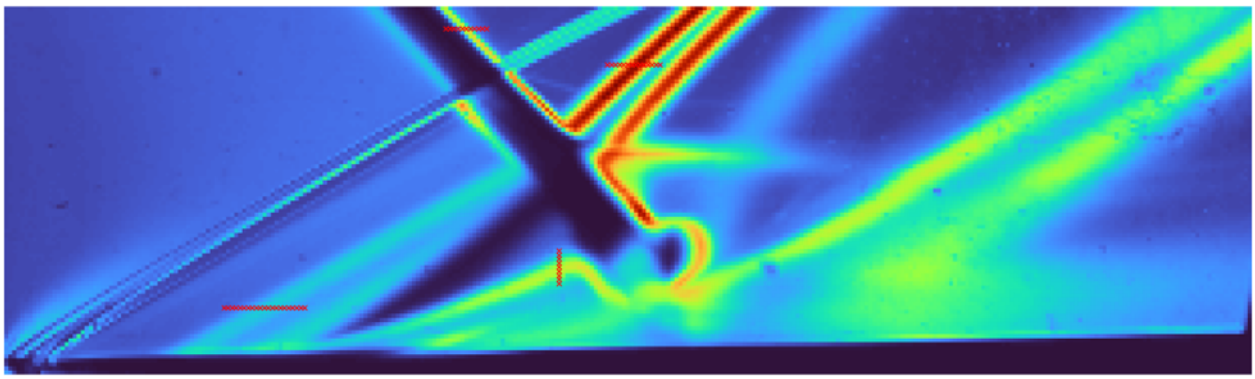

Figure 4.5: Locations where the FFT can be taken in the frequency analysis, test case Ma = 2.3, p_T = 2.8 bar, 19°s.g

The basis of digital signal processing (and, for the scope of the present thesis, the FFT and PSD analysis) is very well described in Smith's Guide for Digital Signal Processing [46]. In principle, as engineers, we are interested in characterizing specific (or random thereof) processes mathematically. Therefore, we can decompose a time- (or frame-, in this case) domain signal into its constituent frequency components as explained before.

In digital form, the most efficient tool for this purpose is the Fast Fourier Transform (FFT). The FFT is an algorithmic implementation of the Discrete Fourier Transform (DFT), which, for a sampled signal $x[n]$ of length N, is given by:

$$X[k] = \sum_{n=0}^{N-1} x[n]\, e^{-j2\pi \frac{kn}{N}}, \quad k = 0, 1, \ldots, N-1 \tag{4.4}$$

Here, $x[n]$ represents the signal value at the n-th sample, j is the imaginary unit, and X[k] denotes the complex amplitude of the k-th frequency bin. By applying the FFT, one can efficiently analyze how the signal energy is distributed across different frequencies (and see if there is a dominant one). In the context of Schlieren image sequences, each image (or a derived quantity from each image) can be treated as a sample in time, allowing to investigate unsteady flow phenomena through their spectral characteristics.

While the FFT reveals frequency components, it can be more informative to focus on how signal power is distributed over frequency. The Power Spectral Density (PSD) provides exactly this. Conceptually, the PSD describes the average power (mean square amplitude) per unit of bandwidth (it is measured typically in Watt/Hz, hence why it is called power "density").

For a discrete signal of length N and sampling frequency fs, the estimate for the PSD can be defined as:

$$S_{xx}(f) \approx \frac{1}{N f_s} |X[k]|^2 \tag{4.5}$$

Where $X[k]$ is the FFT of the time sequence $x[n]$ (as defined in Equation 4.4). Unlike simply looking at an averaged value of the FFT, the PSD shows how the energy in the signal is spread across the frequency spectrum, making it particularly valuable for identifying dominant frequencies or broadband noise levels.

Welch's method [47] provides an estimate for this PSD and is the most convenient and fast tool to be used with matlab. It divides the signal into successive blocks, performs the periodogram for each of these blocks, and then averages them. According to this, the periodogram of the m-th block is given by:

$$P_{x_m,M}(\omega_k) = \frac{1}{M}\left|\mathrm{FFT}_{N,k}(x_m)\right|^2 \tag{4.6}$$

And Welch's estimate for the PSD is:

$$\hat{S}_x^{\mathrm{Welch}}(\omega_k) = \frac{1}{K}\sum_{m=0}^{K-1} P_{x_m,M}(\omega_k) \tag{4.7}$$

Where, similarly as in Equation 4.4, K denotes the frame number. As can be seen in Equation 4.6 and Equation 4.7, Welch's estimate is an average of periodograms in time. In matlab, the function pwelch(x) divides the signal x into as many segments as possible without exceeding eight segments in total, each of which has 50% overlap with its neighbor. This design choice creates a balance between spectral resolution (longer segments yield finer frequency resolution) and statistical reliability (more segments reduce variance). Specifically, "50% overlap" means that the second segment begins halfway through the first segment, the third begins halfway through the second, and so on.

Also mentioned in the matlab guide for the function pwelch[5] is that this function is that each segment is multiplied by a Hamming window. This Hamming window is defined as:

$$w[l] = 0.54 - 0.46\cos\left(\frac{2\pi l}{L-1}\right), \quad l = 0,\ldots,L-1 \tag{4.8}$$

With a number of L samples of the signal and l the l-th sample of that signal. Windowing reduces discontinuities at the segment boundaries that can otherwise introduce spurious high-frequency content in the FFT. The Hamming window leads to an acceptable compromise between main-lobe width (frequency resolution) and side-lobe level (leakage suppression). After windowing, each segment is Fourier-transformed, yielding a so-called modified periodogram. Averaging these periodograms across all segments (including overlapped data) produces a smoother, less noisy PSD estimate than a single periodogram approach, finalizing the description of Welch's method and why it is the preferred method in the frequency analysis.

4.4 Shock polar analysis

It was previously explained that, once the relevant test cases are selected, the oscillation mechanism would be searched for and identified. Then, we would check whether or not the periodic appearance and disappearance of the Mach stem occurs. To be able to do this analytically, one would either need to know the wave angle (the angle formed between line bordering regions 0 and 2 and the flat plate in Figure 4.6a), or the turn angle (which would correspond to the separation bubble angle to the flat plate). Because the incoming Mach number and the turn angle of the impinging shock are are known, three shock polars can be computed (Figure 4.6b):

- The first (centered) polar corresponds to region 0 and dictates the conditions in regions 1 and 2;
- The second (left) polar corresponds to the obtained Mach number in region 1 following the first calculation and the turn angle of the shock generator;

[5] https://mathworks.com/help/signal/ref/pwelch.html

- The third (right) polar corresponds to the calculated Mach number in region 2 and the wave angle of the separation shockwave.

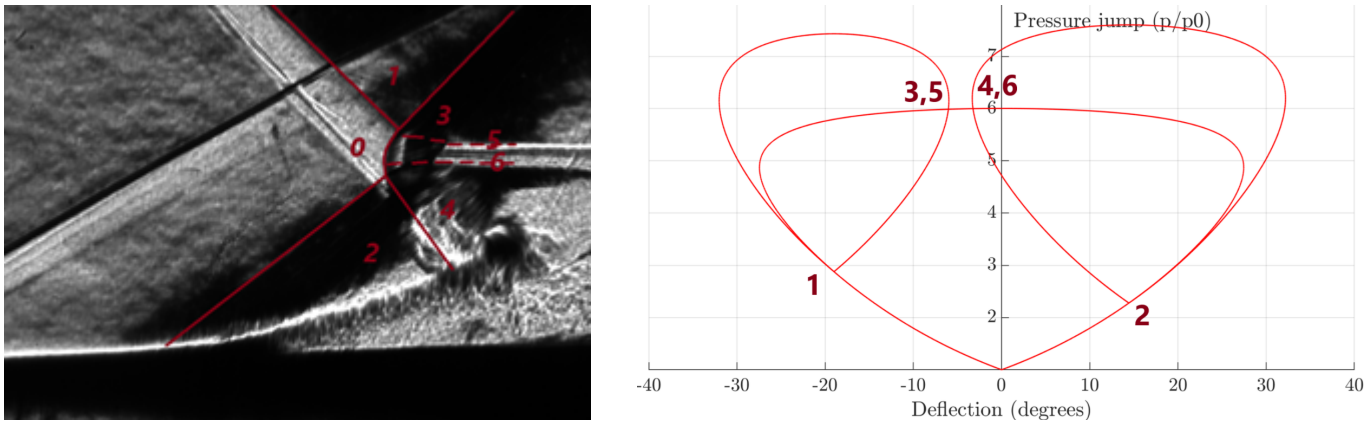

(a) spark light Schlieren image of the test **(b)** shock polar extracted using the information from a)

Figure 4.6: Example of a shock polar analysis, test case Ma = 2.3, p_T = 2.8 bar, 19°s.g.

Based on the results, the shock polars cand intersect or not. No intersection would be indicative of a Mach stem appearing (which can be verified through the recordings or frames like it is done in Figure 4.6), while an intersection would indicate a regular reflection.

4.5 Uncertainty analysis

In any experimental study, uncertainty analysis is important for judging the reliability of the measured data. When measurements are taken manually, especially from visual methods such as High Speed of Spark Light Schlieren images in this experimental investigation, there is an inherent degree of variability—no two measurements will be exactly the same. By quantifying the uncertainty, we ensure that we provide a clear sense of the accuracy (and repeatability) of the measurements.

It is important to acknowledge that, when calculating and drawing the shock polars, a prevalent aspect of the work involved measuring the separation shockwave angle on the flat plate as captured by the Schlieren recordings. Since the measurement process was done by hand—drawing a reference line along the shockwave and another along the flat plate—small errors in judging the exact position or orientation of the shock inevitably arose. Multiple measurements were taken at the same angle to estimate how scattered these measurements were.

For clarity, an example of how angle measurements were manually taken for the shock polar analysis is depicted in Figure 4.7. In the results section, the figures will usually be presented directly as in Figure 4.7a, with the lines corresponding to the angle measurement being the only ones highlighted to avoid clutter in the image. However, for this section, Figure 4.7b provides more insight into what is depicted in these figures: the flat plate is highlighted in orange and is the four-sided dark polygon in Figure 4.7a. The two lines that are taken for the angle measurement are the line along the turbulent separation shockwave (which is more clearly seen than the separation bubble angle) and the line along the flat plate.

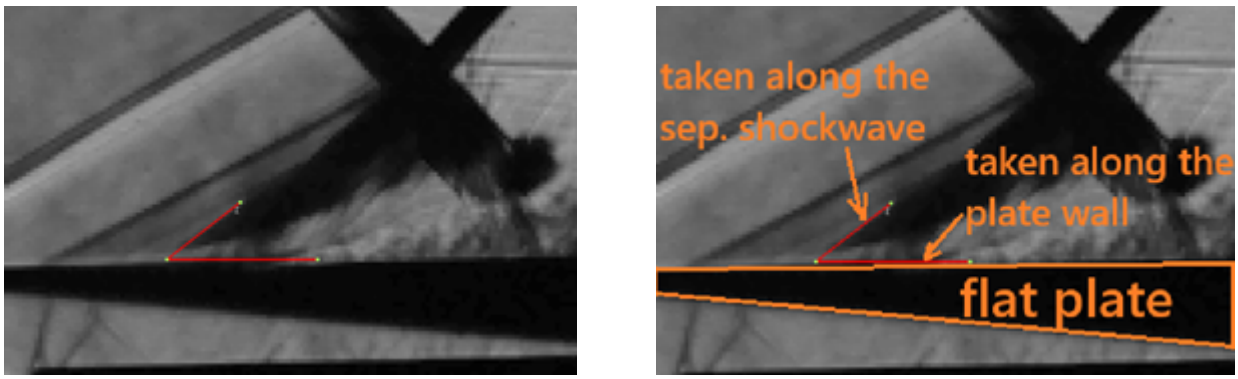

(a) example of an angle measurement **(b)** annotated version

Figure 4.7: Angle measurement example explained

It appears natural that, since these lines are drawn manually, errors can appear. Alternatively, several codes nowadays can perform "shock tracking algorithms", but due to the time constraints, it was decided to manually measure the angles observed.

To quantify the spread of the measured angles around their average value, we use the well-known standard deviation (σ). For a number of N repeated measurements of the shock angle (denoted by x1, x2, ..., xN), the mean angle is calculated like in Equation 4.9:

$$\bar{x} = \frac{1}{N}\sum_{i=1}^{N} x_i \tag{4.9}$$

The variance is then given by:

$$\sigma^2 = \frac{1}{N}\sum_{i=1}^{N} (x_i - \bar{x})^2 \tag{4.10}$$

From Equation 4.10 it can be seen that the standard deviation is the square root of the variance. The latter quantifies how widely individual data points deviate from their mean by taking the average of the squared differences between each data point and the mean. This is important, because it shows how "dispersed" the dataset is, allowing us to compare the variability across different experimental conditions.

If the main interest is the average shock angle measured rather than each individual measurement, we are often more concerned with the standard error of the mean rather than the raw standard deviation:

$$\bar{\sigma}_x = \frac{\sigma}{\sqrt{N}} \tag{4.11}$$

This tells us how precisely we have determined the mean. Importantly, as we increase the number of repeated measurements (NNN), the standard error of the mean decreases. In this study, we first conducted a quick test by measuring the same shock angle 30-35 times, arriving at a standard deviation of about σ = 0.41°. To achieve a standard error of the mean of roughly 0.1°-0.15°, it was decided to perform circa 10 measurements for each angle, such that:

$$\bar{\sigma}_x \approx \frac{0.41^\circ}{\sqrt{10}} \approx 0.13^\circ \tag{4.12}$$

This level of uncertainty was deemed sufficient for the purposes of the shock polar and flow analysis.

The second part of the measurements involved identifying and measuring specific lengths in the Schlieren videos. As explained in this chapter, this was based on the spatial location of steep density gradients (as indicated by high pixel-intensity differences). These length measurements were automated in MATLAB, using image-processing scripts to detect where the highest pixel intensity gradients were and record their location. Because the same algorithm is applied consistently to the same image frames, the result does not vary when the process is repeated—there is effectively only one "measurement." Hence, we cannot apply

the same statistical approach we used for angle measurements (i.e., repeated manual estimates) to reduce the variance of the mean.

Nevertheless, an estimated uncertainty of about 3–4 pixels can be assigned to this procedure, corresponding to approximately 1 mm in physical length at the scale of our setup. This estimation was chosen to reflect typical fluctuations in edge detection due to noise, limited spatial resolution, and minor variations in image thresholding.

Chapter 5

Results

Referring back to Table 3.1, the extensive volume of tests and associated data required a careful preselection process to ensure a focused and meaningful analysis. To achieve this, the tests were selected based on specific criteria, including the observed frequency content and the clarity with which the investigated OSBLI mechanism was observed.

5.1 Test case selection

The tests which resulted in wind tunnel unstart were excluded due to their lack of relevance. Consequently, the most representative and informative cases, as summarized in Table 2, were selected for detailed analysis. It was decided that this approach ensured a proper analysis of all relevant phenomena without the need for redundant examination of the entire dataset.

Nr.	Ma	p_T **[bar]**	Re_x $(\cdot 10^6)$	Θ	**Observation**	**Inviscid pressure rise**
1	2.3	2.6	2.008	19°	Low oscillation amplitude	2.878
2	2.3	2.8	2.056	19°	Desired oscillation	2.878
3	2.3	4	2.968	19°	Low oscillation amplitude	2.878
4	2.3	4.2	3.228	19°	Very low oscillation amplitude	2.878
5	2.4	2.8	2.183	19°	Low oscillation amplitude	2.96
6	2.6	3.2	2.643	19°	Very low oscillation amplitude	3.143
7	2.6	3.4	2.792	19°	Very low oscillation amplitude	3.143
8	2.3	2.6	2.217	17°	Desired oscillation	2.6
9	2.4	2.8	2.48	17°	Low oscillation amplitude	2.6
10	2.4	2.8	1.896	22°	Desired oscillation	3.45
11	2.6	3.4	2.414	22°	Low oscillation amplitude	3.67
12	2.7	3.6	1.781	22°	Very low oscillation amplitude	3.79
13	2.7	3.8	1.814	22°	Very low oscillation amplitude	3.79

Table 5.1: Tests selected for post-processing

To further justify the selection of these tests, the main criteria included:

- selecting all the tests where the “desired oscillation” (in green) was observed; a further description of what this physical mechanism entails is provided in the next part of the chapter;
- selecting tests such that a Reynolds number comparison can be performed: refer to tests 1-4, 5-6, 12-13 in Table 5.1, where the constant Mach number and shock generator angle meant that changing the total pressure in the wind tunnel could allow only a modification of the Reynolds number. One can already see for test cases 1-4 that different shock oscillation mechanisms were observed by simply modifying this parameter;

- selecting tests where very small changes in parameters led to different physical mechanisms: see cases 1 vs. 5 (in particular) and cases 8 vs. 9, where a minimal change in Mach number/total pressure led to a change in the observed phenomenon;
- selecting tests at the same wind tunnel conditions, but different shock generator angles: see cases 5, 9, 10 (all at Ma = 2.4, pT = 2.8 bar) but at three different shock generator angles leading to different observed physical mechanisms;
- selecting tests which where situated in the theoretical "transitional" range according to Giepman [16], but no transitional/laminar shockwave was observed in the Schlieren recordings (see cases 4, 6, 7, 12, 13).

Regarding the second bullet point, where the Reynolds number comparison is mentioned, it is worth noting that a separate analysis on the individual effect of the inviscid pressure rise was also desired. This was pursued by attempting to maintain the same Rex and modifying the other parameters (total pressure, Ma, shock generator angle) accordingly, and is shown in the initial test matrix, Table 3.1.

However, most of these tests led to the unstart of the wind tunnel, so the desired test cases needed for comparison were unfortunately not achieved. The datasets were large and comprised of 2 – 2.5 second recordings (usually the maximum allowed recording time for the given FPS settings) corresponding to circa 175.000 consecutive frames, since it was not known beforehand how long the timescale was for a single oscillation cycle.Later, in the analysis, what was observed is that even 20.000 frames (approximately 0.3 seconds in the live recording) were enough to reach the same results in terms of the obtained peaks of the frequency analysis.

5.2 Description of the oscillation dynamics

The steps of this oscillation mechanism are presented in Figure 5.1, and the sequence runs from the top left figure in clockwise order. Note that, in Figure 5.1a, a faded shockwave can still be observed upstream of the dark region of the compression waves. This fading shockwave corresponds to a previous oscillation cycle, but it was still captured as a new laminar separation shockwave began to travel upstream.

(a) "initial state" - no upstream moving separation shock yet

(b) 5 frames (0.063 ms) later

(c) 19 frames (0.24 ms) later

(d) 12 frames (0.15 ms) later

Figure 5.1: Oscillation mechanism identified during the baseline run: Ma = 2.3, p_T = 2.8 bar, 19°s.g.

For a better understanding of the description presented in Figure 5.1, the topology of the physical components of the interaction is depicted in Figure 5.2, where the adapted sketch of the transitional SBLI is compared to the results obtained from the High Speed and the Spark light Schlieren visualizations. Several features, such as the leading edge shockwave originating from the high speed flow encountering the sharp wedge of the flat plate leading edge are also highlighted. The "transition region" occurring between lines C2' and C2 is also highlighted.

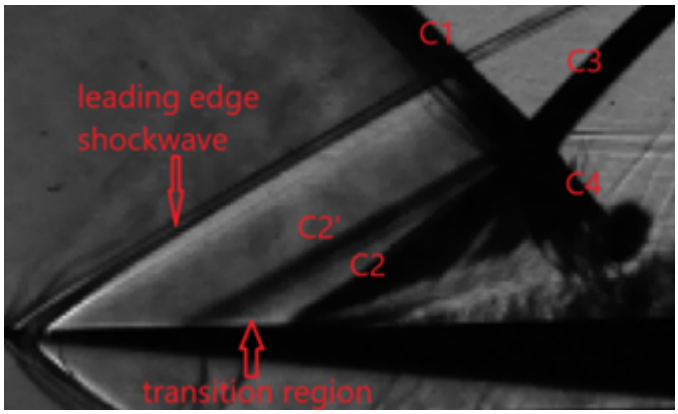

(a) high speed Schlieren frame

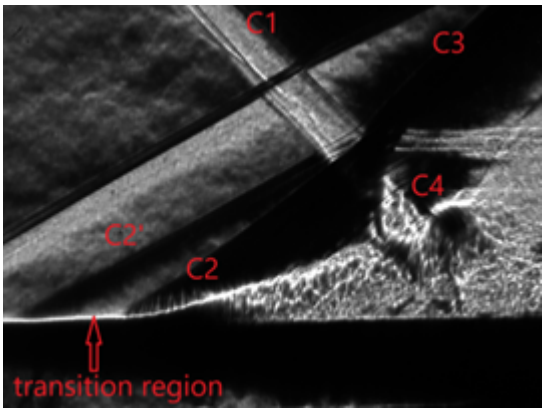

(b) spark light Schlieren frame

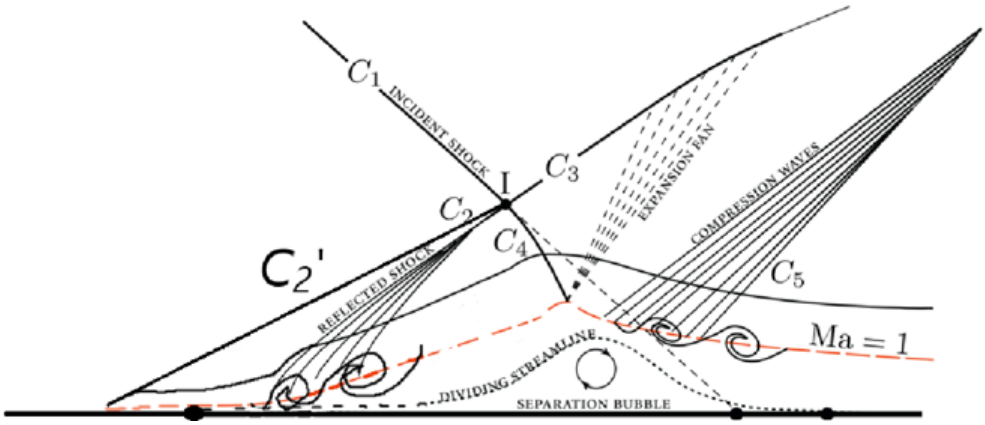

(c) sketch of the interaction, adaptem from Pasquariello et al. [36]

Figure 5.2: Topology of the components observed in the tests

The second case observed, which in Table 3.1 and Table 5.1 is referred to as a "low oscillation amplitude" is depicted in Figure 5.3. What this means more exactly is that, during the run, a clear shock movement upstream followed by its collapse was observed periodically, but the shock travel (amplitude) observed was lower than in the baseline case, where the shock traveled upstream with an amplitude of circa 12 mm, as shown in Nel et al. [9].

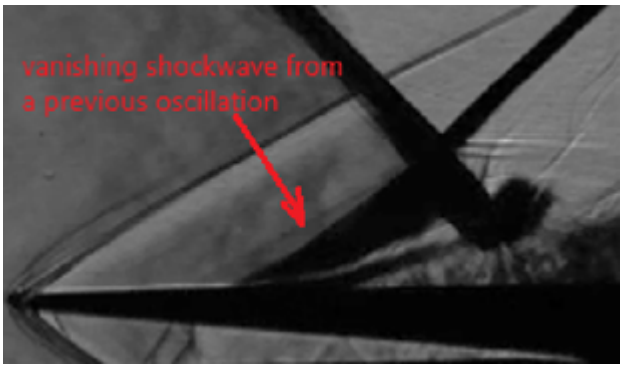

(a) beginning of the oscillation

(b) end of the oscillation

Figure 5.3: Example of a case with "low oscillation amplitude": Ma = 2.3, p_T = 4 bar, 19°shock generator

The third and final situation which was documented as an “observation” in the test matrix is the case where little to no shock travel was observed. Such an example is presented in Figure 5.4. As a note, the fact that no significant travel upstream of the shock was recorded does not necessarily mean that there was no oscillation of any component of the OSBLI (in fact, the reflected shockwave in Figure 5.4 was observed to oscillate in the high speed Schlieren visualization), but rather that this laminar separation shockwave is not developing within this mechanism (i.e., the interaction is not transitional, but turbulent/laminar).

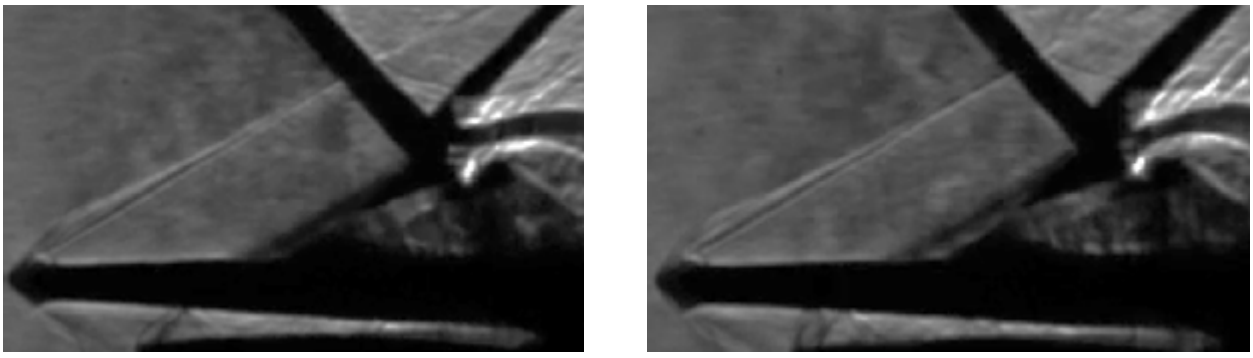

(a) beginning of the oscillation **(b)** end of the oscillation

Figure 5.4: Example of a case with "very low oscillation amplitude": Ma = 2.3, p_T = 4.2 bar, 19°shock generator

With the definitions of how the different physical mechanism cases were labeled, the next step is the angle analysis of the shockwaves which relates to the appearance and the disappearance of the Mach stem.

5.2.1 Analysis of the reference/baseline case

This case (described by the conditions Ma = 2.3, p_T = 2.8 bar, 19°shock generator), for which already a dominant frequency of circa 3728 Hz was recorded by Nel et al. [9], represents the starting point for the analysis. Aside from analyzing the frames and noticing the periodically appearing “laminar” separation shockwave before the flow transitions prematurely, leading ultimately to a turbulent separation shockwave (Figure 5.1), it is useful to also analyze the frequency content of the test.

While the visualization of the physical mechanism is useful in identifying and confirming the oscillation mechanism, the PSD analysis confirms this low-frequency unsteadiness. Recall Figure 4.5 with the locations where the FFT of the image sequence is performed. By taking the Power Spectral Density analysis (pwelch) of the selected locations, the frequency content depicted in Figure 5.5 is obtained.

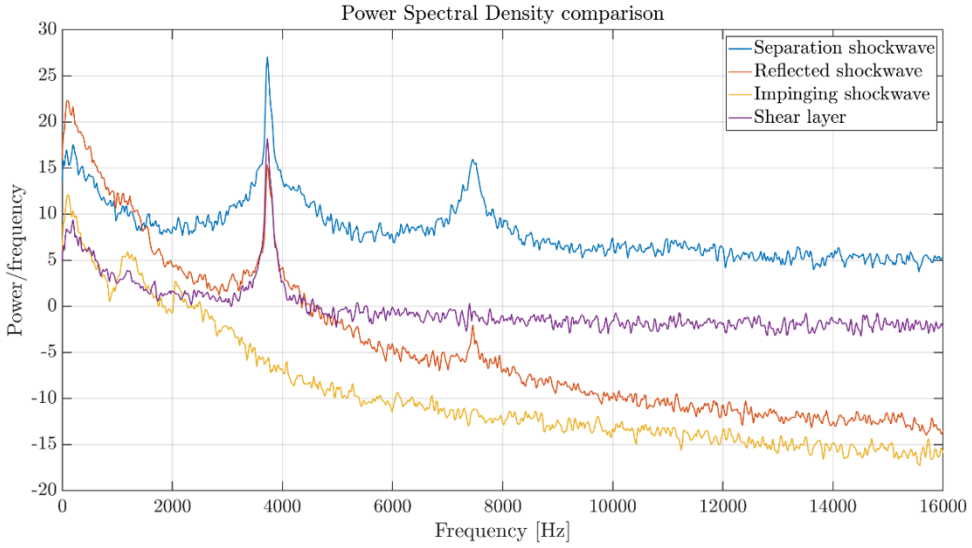

Figure 5.5: Power Spectral Density comparison between different regions of the flow for the baseline case

This figure confirms the results obtained by Nel et al. [9]. It shows that the system which includes the separation shockwave, the reflected shockwave and the movement of the shear layer oscillate at the same frequency, which in this case is also 3728 Hz. What is, however, also interesting to note is that the whole system is "wandering" at a low frequency of about 100 Hz. This also includes the impinging shockwave, as seen in Figure 5.5, which only shows this "peak".

A separate FFT/PSD analysis was performed in the freestream (outside of the interaction zone, in order not to have any "interference" from the frequencies of the SBLI mechanism) to try to identify whether this very low-frequency peak is caused by external parameters (such as the pulse-width modulation or "buzz" from the external lighting in the laboratory), however no such peak is recorded.

This low frequency was ultimately ascribed to an instability causing the impinging shockwave to oscillate (such as an oscillation of the shock generator due to the mounting and screws not being sufficiently tight). However, since the results obtained for the frequency peak of the mechanism itself are still the same as the reference papers, this low frequency peak was not considered to affect the investigated mechanism significantly.

The Reynolds number computed for this case is $Re_x = 2.056 \cdot 10^6$, which falls within the "transitional" range defined by Giepman [16]. The Reynolds number is calculated using point x4 from Figure 5.6 (at 65.21 mm from the leading edge) using the methodology described in Chapter 4.

The methodology of determining the points in Figure 5.6 is the following:

- point x1 is determined by calculating the maximum gradient in the laminar shock area close the flat plate wall (thus determining the mean most upstream travel position for the laminar shockwave);
- point x2 is determined by calculating the maximum gradient in the first part of the laminar separation shock travel, but is not used in the calculations;
- point x3 is determined by calculating the intersection point between the flat plate and the shadow of the turbulent compression wave fan. It is used as a mean "starting point" for the laminar separation shockwave
- point x4 is determined by calculating the intersection point between the flat plate and the impinging shockwave. It is relevant to calculate the Rex and determine if the interaction should be laminar/transitional/turbulent.

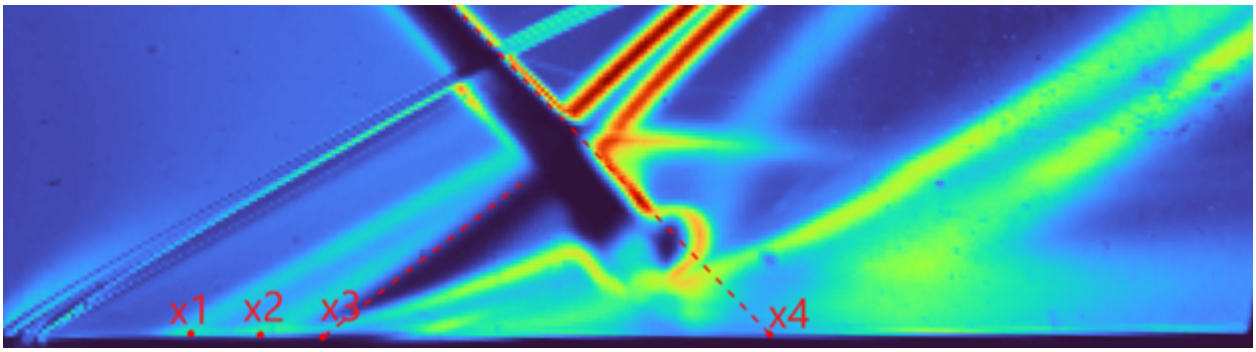

Figure 5.6: Computed distances for the baseline case for the Re_x calculation

There is an additional mention that, in the PhD thesis of Giepman [16], he also noted an acceleration of the transition even for the weak SBLI he investigated. It is expected that, for the cases investigated in this thesis, where very strong OSBLIs are tested, transitional and turbulent SBLIs will occur at even lower Reynolds number than predicted by Giepman.

After confirming that there is a clear oscillation (confirmed by the peaks in the PSD analysis), and that the Reynolds number defined previously falls within the transitional range, what was also observed during

the recordings was the appearance and the disappearance of the Mach stem. To confirm this, angle measurements for the turbulent separation shockwave were taken using the flow visualization program (as described in Chapter 4).

When a single slip line was observed (as is the case in Figure 5.7 and more clearly represented visually in the Spark light visualization of Figure 5.8a), the angle between the turbulent separation shockwave and the flat plate is measured in order to draw the shock polars (for which the incoming Mach number and the two wave angles – from the shock generator and from the separation bubble are needed).

One such measurement example is depicted in Figure 5.7. The measured angle between the turbulent separation shockwave and the flat plate is circa 34°(Figure 5.7a). This is easier to identify than by measuring the "turn" angle of the separation bubble, which is harder to identify in the frames. However, for comparison, the turn angle was also measured in Figure 5.7b to be 10°.

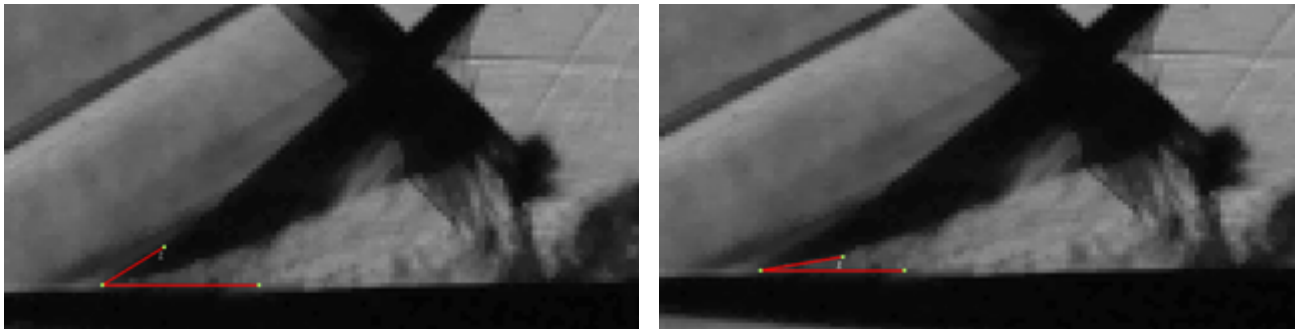

(a) measured angle of the wave: 34°

(b) measured angle of the separation bubble (the turn angle): 10°

Figure 5.7: Angle measurement in the baseline case with a regular reflection appearing

Using the oblique shock relationship between the shock angle β and the deflection/turn angle θ:

$$\cot(\theta) = \tan(\beta)\left[\frac{(\gamma+1)Ma^2}{2\left(Ma^2\sin^2(\beta)-1\right)}-1\right] \tag{5.1}$$

It was found that, for a turn angle of 10°and Ma = 2.3, the obtained wave angle is β=34.2°, which is in acceptable accordance with the measured wave angle in Figure 5.7a of 34°.

The shock polar can be drawn given these parameters and is depicted in Figure 5.8b, with Figure 5.8a defining the numbered regions in the flow. The intersection of the two shock polars originating from point 1 (corresponding to the shock generator at 19°) and point 2 (corresponding to the separation shockwave at 10°) confirms the existence of only a regular reflection.

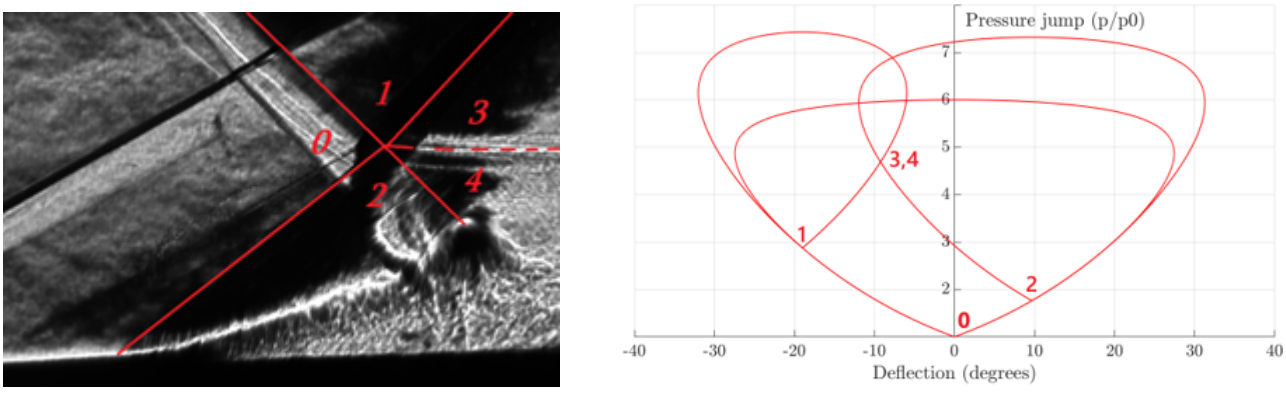

(a) spark light Schlieren visualization

(b) associated shock polar

Figure 5.8: Spark Light Schlieren visualization of the case with regular reflection and associated shock polar

For this same test case, throughout the recording, one could also notice a Mach reflection appearing; notice how this occurs with the laminar separation shockwave in the most upstream position (right before collapsing), this is usually the case throughout the recording.

Once again, to confirm this via the shock polars, the wave angle of the separation shockwave was measured (as seen in Figure 5.9) and is observed to be 37.88°. Once again, for the purpose of comparison and confirming that the two measurements are in agreement with Equation 5.1, the separation bubble angle was also attempted to be measured, with an obtained value of 13.3°. This value for the turn angle corresponds to a wave angle of 37.74°, which once again falls within an acceptable 0.1°range from the measurement of the wave angle in Figure 5.9a. A comprehensive explanation of all components in the figure and how the lines for the angle measurements are taken was provided in Chapter 4, Figure 4.7.

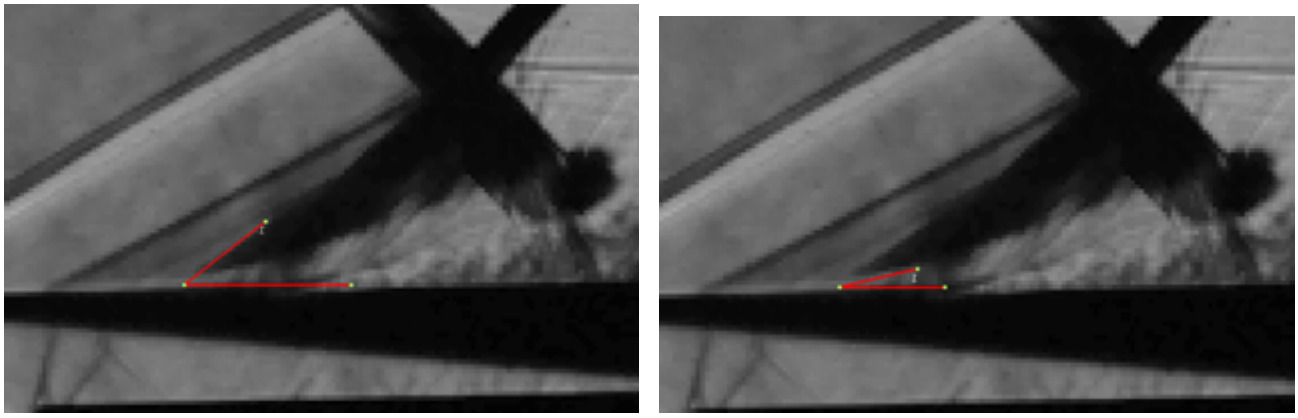

(a) measured angle of the wave: 37.88°

(b) measured angle of the separation bubble (the turn angle): 13.3°

Figure 5.9: Angle measurement in the baseline case with a Mach reflection appearing

As in the previous case, the shock polars were drawn (Figure 5.10b), and the respective regions obtained are depicted in Figure 5.10a. As can be seen both visually (through the two slip lines observed in the spark light visualization of Figure 5.10a between regions 3-5 and 4-6) and the non-intersection of the shock polars, the existence of a Mach stem is confirmed.

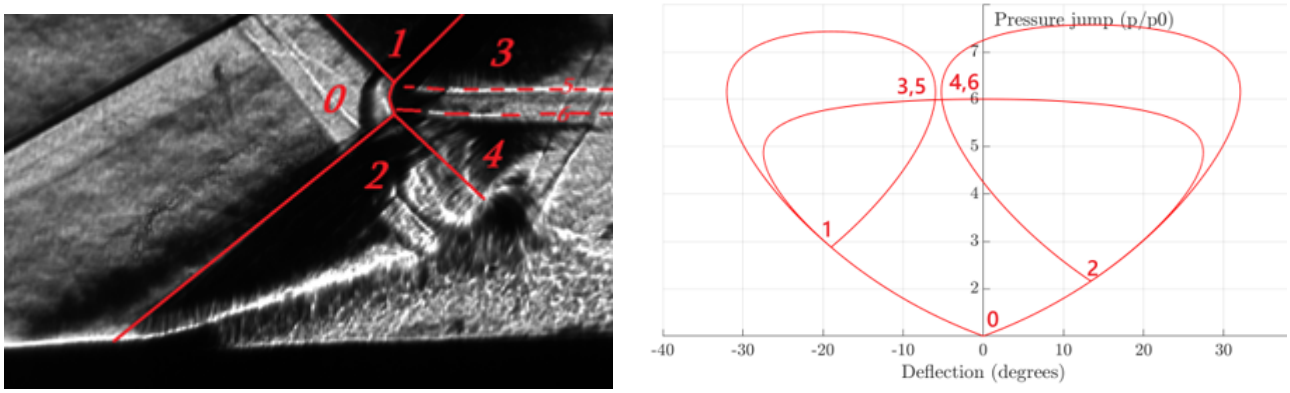

(a) spark light Schlieren visualization

(b) associated shock polar

Figure 5.10: Spark Light Schlieren visualization of the case with Mach reflection and associated shock polar

To conclude the analysis of this reference case, the following aspects were observed:

- The shock oscillation mechanism is present and visible both visually (through the frames) and in the frequency content (PSD analysis);
- The calculated Rex value falls within the transitional range found by Giepman [16] for the flat plate, justifying the transitional OSBLI;

- There is an appearing and disappearing Mach stem throughout the interaction; the Mach stem usually develops when the laminar separation shockwave is in the most upstream position.

5.2.2 Investigation of the Mach number effect on the interaction

Previously, an investigated "baseline" case running at Ma = 2.3, pT = 2.8 bar, 19°shock generator was thoroughly presented and analyzed, showing several features such as the appearance of the dual domain (Mach reflection – regular reflection transition occurring periodically). Since the parameters that can be changed during testing are the Mach number (and, consequently, the inviscid pressure jump of the interaction), and the Reynolds number (through both the Mach number and the change in the total pressure of the wind tunnel), the investigation focuses on how small changes in the Mach number (and pressure jump) and Reynolds number affect the physical phenomenon.

5.2.2.1 Mach number effect for the 19°shock generator

As such, the next case investigated is at Ma = 2.4, p_T = 2.8 bar, 19°shock generator, so only a 0.1 increase in Mach number compared to the baseline case.

Figure 5.11 shows the computed distances from the standard deviation image of this test case. Already, by visual comparison with the same figure of case I (Figure 5.6), the entire image appears more unsteady. However, by computing the Rex for this case, a value $Re_x = 2.183 \cdot 10^6$ is obtained, which, as before, is within the theoretical transitional range.

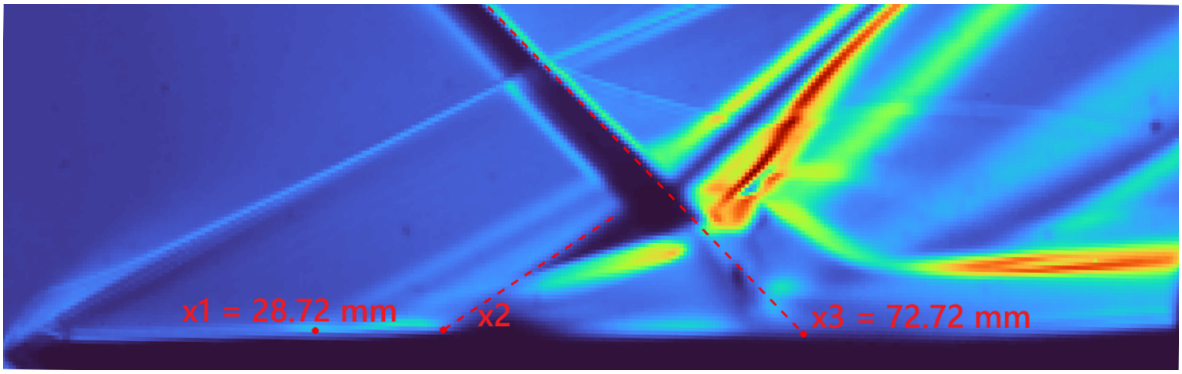

Figure 5.11: Computed distances for the Rex calculation of case II: Ma = 2.4, p_T = 2.8 bar, 19°s.g.

The same PSD analysis as before was performed and is presented in Figure 5.12, showing a direct comparison to the previously presented PSD analysis of the baseline case, where the peaks in the oscillation were very clear. Ignoring the very low-frequency peak coming from the impinging shockwave, it is clear peaks are not as prominent as for the reference case.

Furthermore, we cannot state anymore that the whole "system" comprising of the separation shockwave, the reflected shockwave, and the shear layer movement is oscillating at the same frequency (as, again, was very clear in Figure 5.5 for case I). However, there is a slight indication of a preferred oscillation frequency at 2451 Hz (more visible in the peak of the shear layer movement, the purple line in Figure 5.12b).

So far, we have noticed that, for a case with similar Re_x and a similar inviscid pressure jump, after only modifying one parameter slightly (Ma increased by 0.1), the entire oscillation mechanism seems to have modified almost completely; even though the laminar separation shockwave appears and vanishes as before, the preferred oscillation frequency is not as clear as in the reference case.

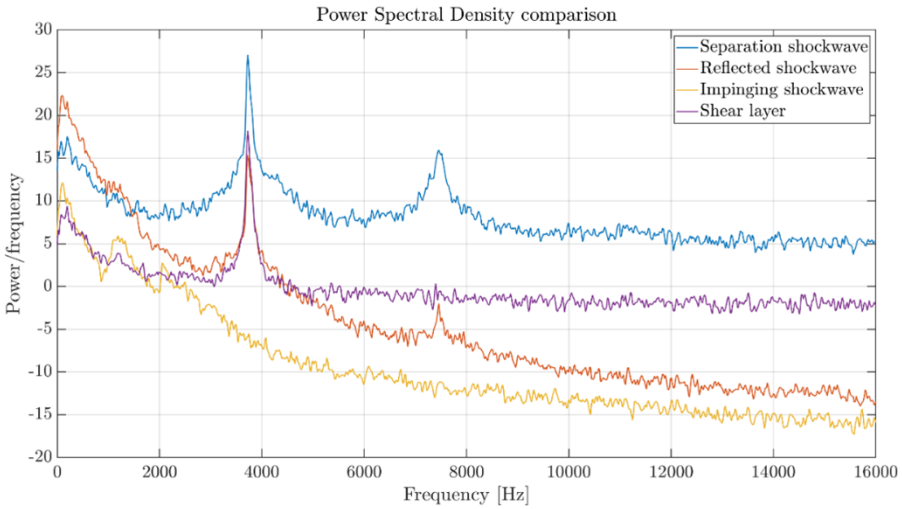

(a) frequency content for the baseline case Ma = 2.3, p_T = 2.8 bar, 19° shock generator

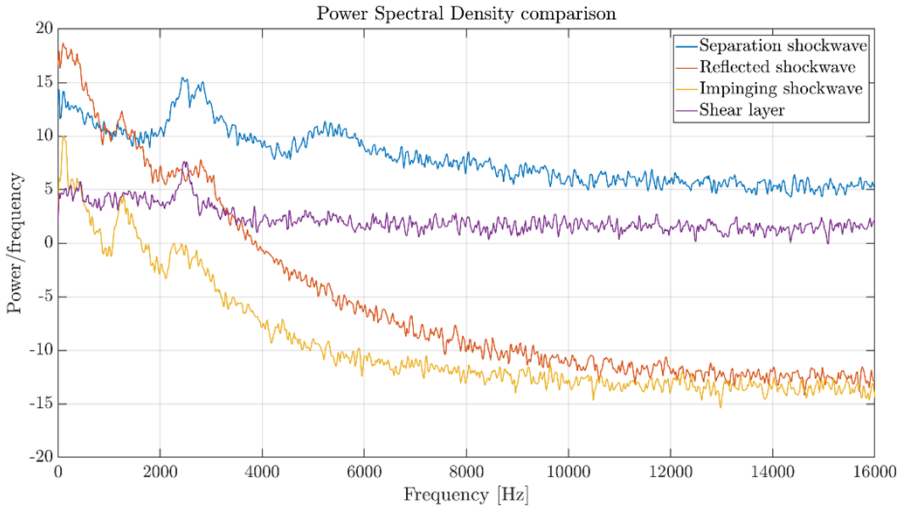

(b) frequency content for the case Ma = 2.4, p_T = 2.8 bar, 19° shock generator

Figure 5.12: Power spectral density comparison showing the effect of a slight change in Ma – 19°shock generator

The same angle measurement methodology was performed for this scenario and is presented in Figure 5.13. Although the images are more distorted than in the previous case, only one slip line could be clearly noticed throughout the development of the physical mechanism. However, at several points, two slip lines appeared for a very short time, suggesting that a Mach reflection does develop very briefly.

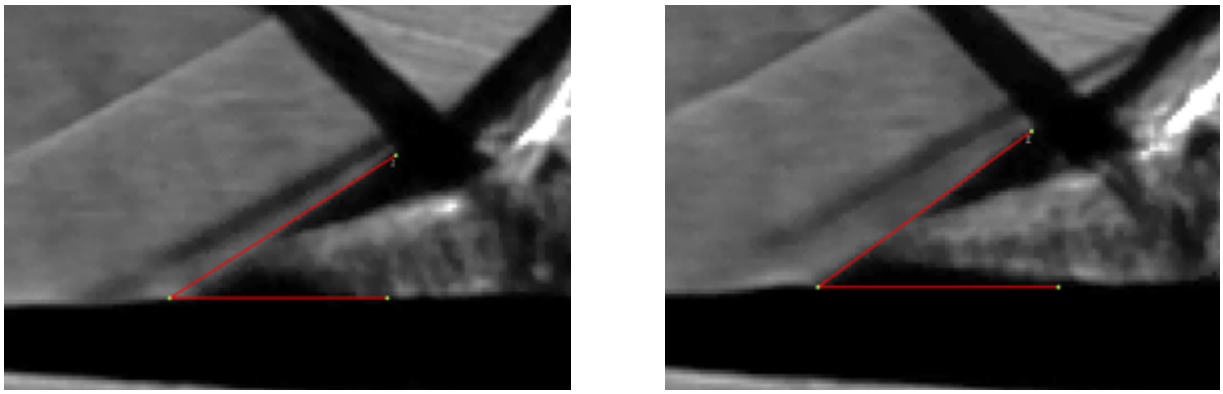

(a) min angle observed - 32.27°

(b) max angle observed - 35.02°

Figure 5.13: Min and Max angles observed for the second case analyzed: Ma = 2.4, p_T = 2.8 bar, 19°s.g.

This is confirmed by once again drawing the shock polars for these cases, as shown in Figure 5.14. Due to the lower angles observed in the separation shockwave, the turn angle is not enough to justify the appearance

of a Mach stem, although for the case where the max angle is observed, the intersecting polars might be close enough for a hysteresis effect to occur at which a Mach stem may still develop even though the curves are intersecting.

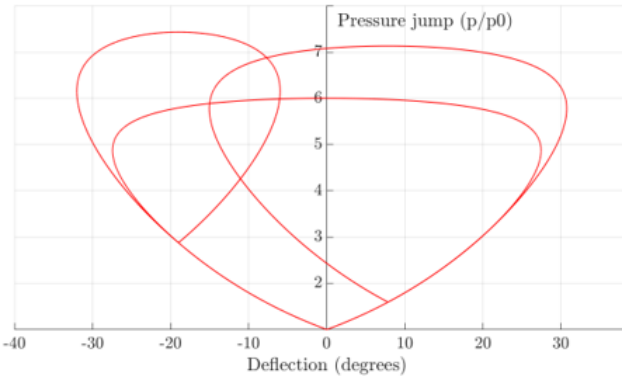

(a) min angle observed – Ma = 2.4, p_T = 2.8 bar

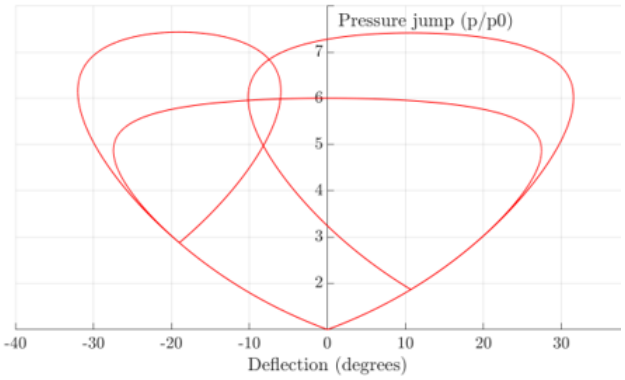

(b) max angle observed – Ma = 2.4, p_T = 2.8 bar

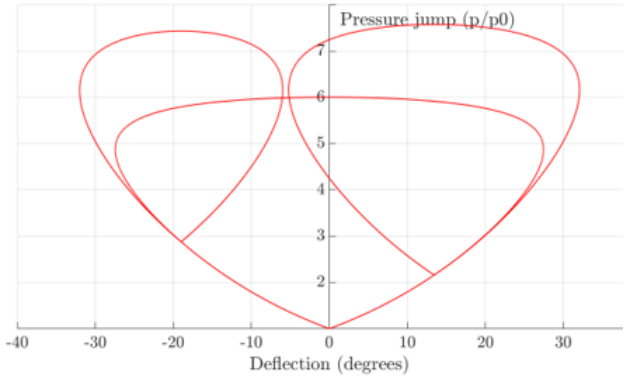

(c) min angle observed – Ma = 2.3, p_T = 2.8 bar (baseline case)

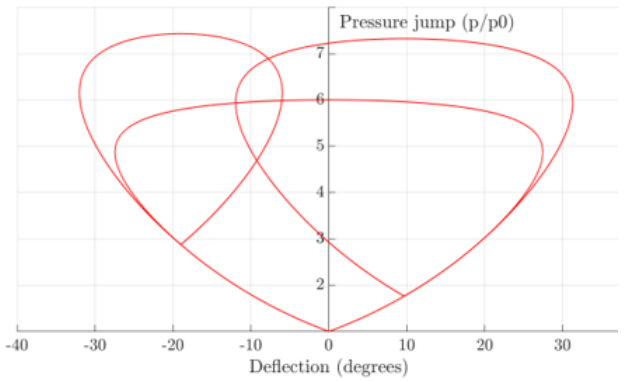

(d) max angle observed – Ma = 2.3, p_T = 2.8 bar (baseline case

Figure 5.14: Corresponding shock polars for the second case analyzed: Ma = 2.4, p_T = 2.8 bar, 19°s.g. and comparison with the reference case

The effect of the Mach number for this case is highlighted by the comparison of the Ma = 2.4 shock polars (Figure 5.14a and Figure 5.14b) with the baseline case, where the dual domain was observed both in the Schlieren recordings and the shock polars (Figure 5.14c and Figure 5.14d).

5.2.2.2 Mach number effect for the 17°shock generator

As observed in Table 5.1, for each shock generator angle investigated, one case where a “desired” oscillation (with its physical mechanisms described at the beginning of the chapter) was selected. Even though the “baseline” case which was recorded for the 19°shock generator had the clearest observed interaction, it is useful for direct comparisons – especially when looking at the effects of the different parameters like Mach number and Reynolds number – to be able to look at “desired oscillation” cases for each shock generator case.

As such, for the 17°shock generator (so a slightly weaker interaction), two particular cases are looked at, see Figure 5.15. In Table 5.1, it is mentioned that the case Ma = 2.3, p_T = 2.6 bar (Figure 5.15a) has a “desired oscillation” recorded, while the second case Ma = 2.4, p_T = 2.8 bar (Figure 5.15b) has a “lower oscillation amplitude”. From the rms images, it can also be seen that there are higher fluctuations for the first case around the area where the separation shockwave travels, confirming this higher unsteadiness. It is worth mentioning that, given the x2 value (theoretical impingement point) for both cases, the Re_x falls within the theoretical transitional range (Re_x = 2.22 million for Ma = 2.3, p_T = 2.6 bar and Re_x = 2.48 million for Ma = 2.4, p_T = 2.8 bar).

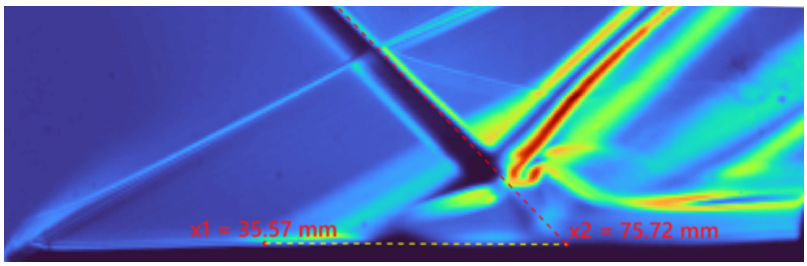

(a) Ma = 2.3, p_T = 2.6 bar (desired oscillation observed)

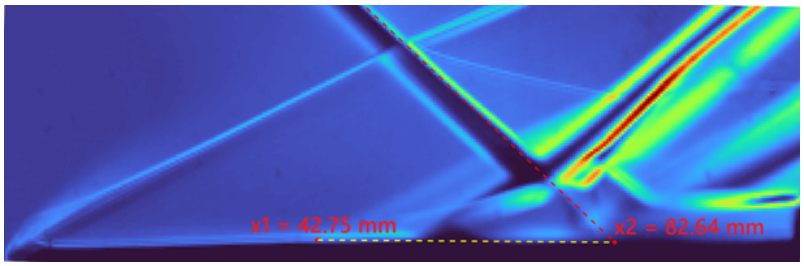

(b) Ma = 2.4, p_T = 2.8 bar (lower oscillation amplitude)

Figure 5.15: Mach number effect - 17°shock generator. Comparison of two cases

Once again, we are looking at very slight changes in Mach number (and inviscid pressure jump) leading to completely different interactions. Just as in the analysis done before for the 19°shock generator, it is useful to compare the frequency content recorded for the two cases, see Figure 5.16a for the 17°shock generator "desired oscillation" case and Figure 5.16b for the case with a lower oscillation amplitude. Similarly as before, there are clear peaks observed when looking at the phenomenon similar to the baseline (Figure 5.16a compared to Figure 5.12a), and these peaks appear to dampen or they disappear altogether at different Mach number (and shock strength through inviscid pressure rise) conditions.

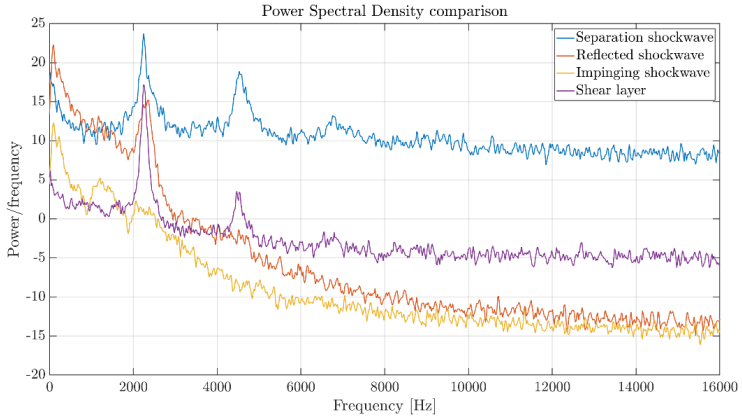

(a) frequency content for the case with desired oscillation: Ma = 2.3, p_T = 2.6 bar, 17°s.g.

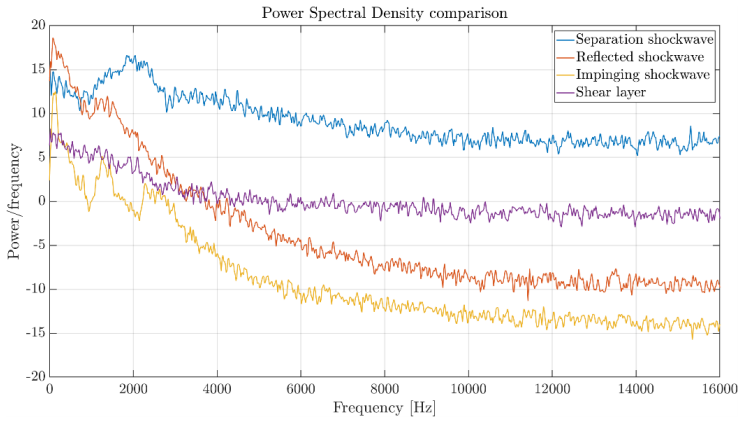

(b) frequency content for the case Ma = 2.4, p_T = 2.8 bar, 17°s.g.

Figure 5.16: Power spectral density comparison showing the effect of a slight change in Ma – 17°shock generator

To analyze the effect that the Mach number has on the appearance of the dual domain, the angles of the separation shockwave are analyzed. The minimum and maximum angles found for the two cases of the 17°shock generator are depicted in Figure 5.17 and show clear differences in the recorded maximum and minimum obtained. Furthermore, by analyzing Figure 5.17b (maximum angle case for the test with a desired oscillation), two shear layers indicative of a Mach reflection can be seen, proving once more that this dual domain appears present for cases with high unsteadiness.

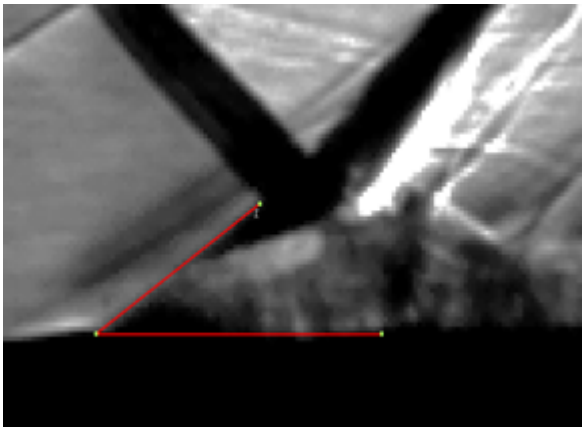

(a) min angle observed (Ma = 2.3, p_T = 2.6 bar): 34.7°

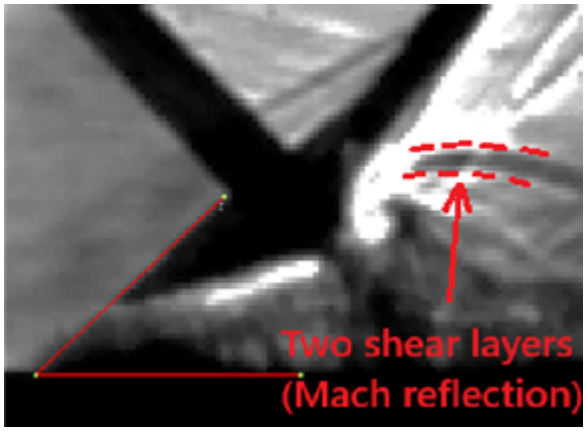

(b) max angle observed (Ma = 2.3, p_T = 2.6 bar): 40.8°

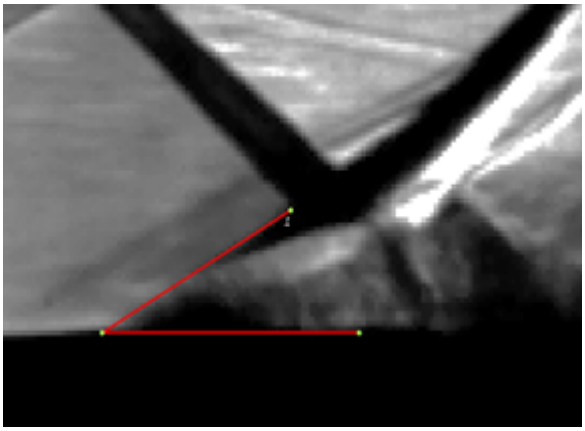

(c) min angle observed (Ma = 2.4, p_T = 2.8 bar): 30.5°

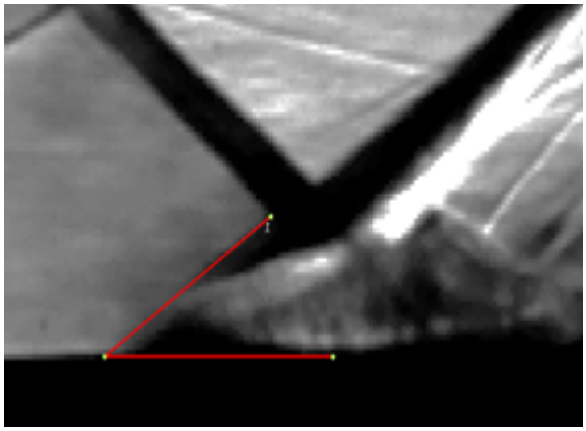

(d) max angle observed (Ma = 2.4, p_T = 2.8 bar): 35.9°

Figure 5.17: Shockwave angle comparison - 17°shock generator Mach number effect

Furthermore, as before, the shock polars for the maximum and minimum angles observed for this comparison are drawn and confirm the appearance of the dual domain for the case with desired oscillation, Figure 5.18a and Figure 5.18b. Moreover, for the second case where low oscillation amplitudes are recorded, only a regular reflection is identified, Figure 5.18c and Figure 5.18d.

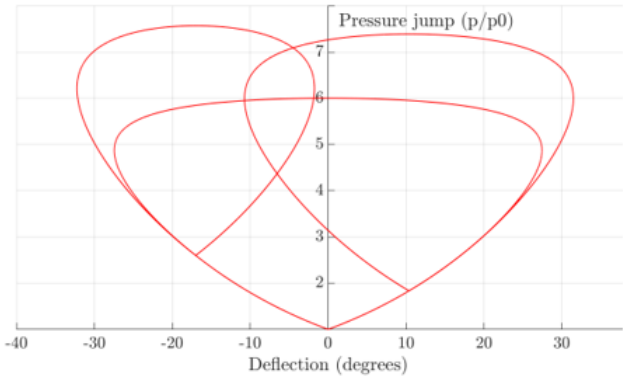

(a) min angle observed – Ma = 2.3, pT = 2.6 bar

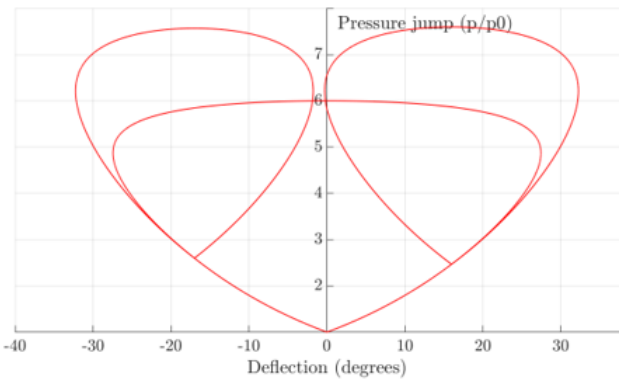

(b) max angle observed – Ma = 2.3, pT = 2.6 bar

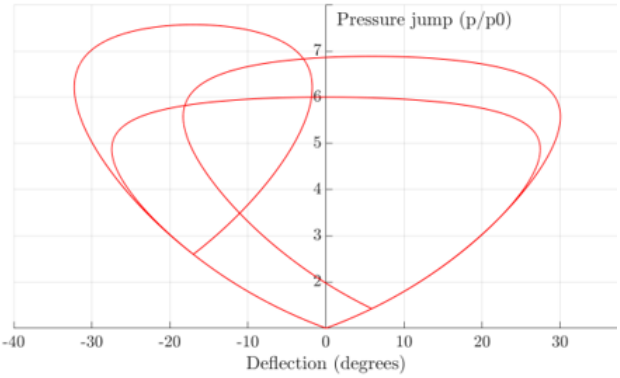

(c) min angle observed – Ma = 2.4, pT = 2.8 bar

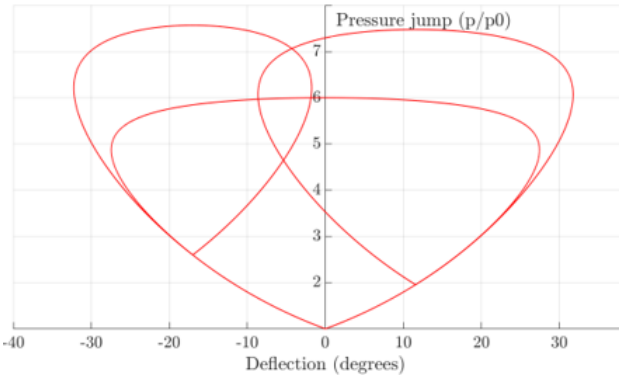

(d) max angle observed – Ma = 2.4, pT = 2.8 bar

Figure 5.18: Corresponding shock polars for the minimum and maximum angles for the two cases at the 17°shock generator – Mach number effect

To conclude this subpart where the effect of the Mach number is analyzed, it could be seen for two distinct cases analyzed that a slight modification in Mach number (consequently, in the inviscid pressure rise and Reynolds number) can lead to significantly different interactions, with a common denominator being that the change in Mach number also affected whether the dual domain appears or not.

5.2.3 Investigation of the Reynolds number effect on the interaction

When describing the experimental setup in Chapter 3, it was noteworthy that a blowdown wind tunnel such as the TST-27 allows the user to change the total pressure of the wind tunnel, and therefore the Reynolds number, while maintaining all other parameters such as Mach number and geometry the same. This makes it easier to perform an isolated Reynolds number effect analysis on the physical interaction, just as was done before for the Mach number.

For this purpose, several cases from the 19°shock generator tests are used and compared to the baseline case Ma = 2.3, p_T = 2.8 bar.

First, we selected a case where only one the total pressure (and hence the Rex) was slightly modified from the baseline; this time, the total pressure was slightly decreased from p_T = 2.8 bar to p_T = 2.6 bar. Therefore, the first case looked at is Ma = 2.3, p_T = 2.6 bar, with its rms visualization in Figure 5.19. The points x1 and x2, as explained, are used to calculate the distances or the Reynolds number.

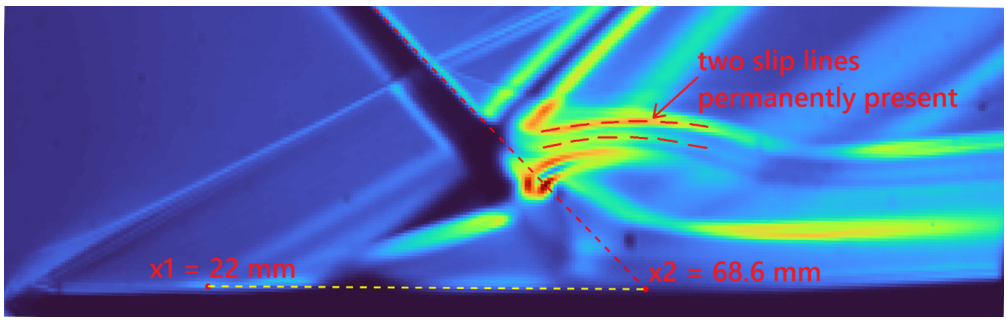

Figure 5.19: Computed distances for the Rex calculation of case III: Ma = 2.3, pT = 2.6 bar, 19°s.g.

Using the same procedure for the Reynolds number calculations, this was found to be Re_x = 2.01 million for the identified theoretical impingement point, which once again falls within the transitional range. Furthermore, in Figure 5.19, note that two slip lines (highlighted with red dashed lines) appear to have a shadow permanently present, which was not seen before. This could already be an indication that, during the interaction, there is no dual domain, but a permanent Mach reflection appearing, which can be confirmed through the shock polars.

An analysis of the frequency content in the image sequence is shown as before in Figure 5.20. The peaks observed do not have the same high amplitude and clarity as for the baseline, however they can be identified.

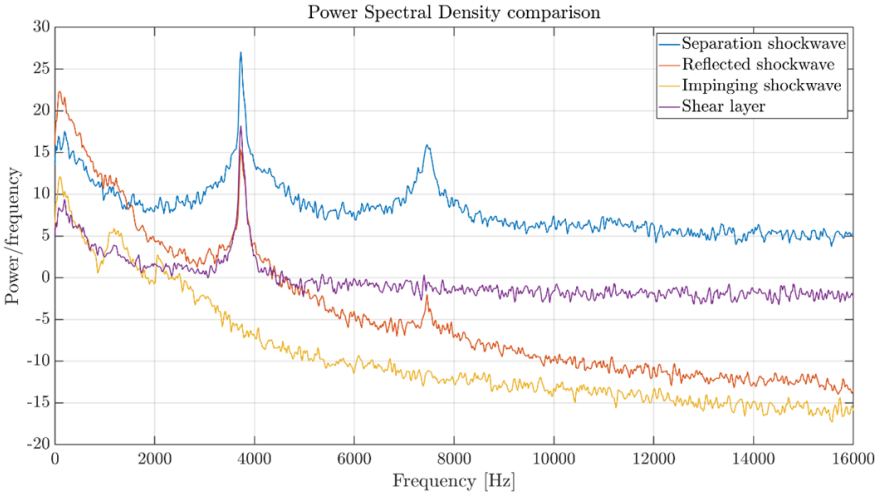

(a) frequency content for the baseline case Ma = 2.3, p_T = 2.8 bar, 19°shock generator

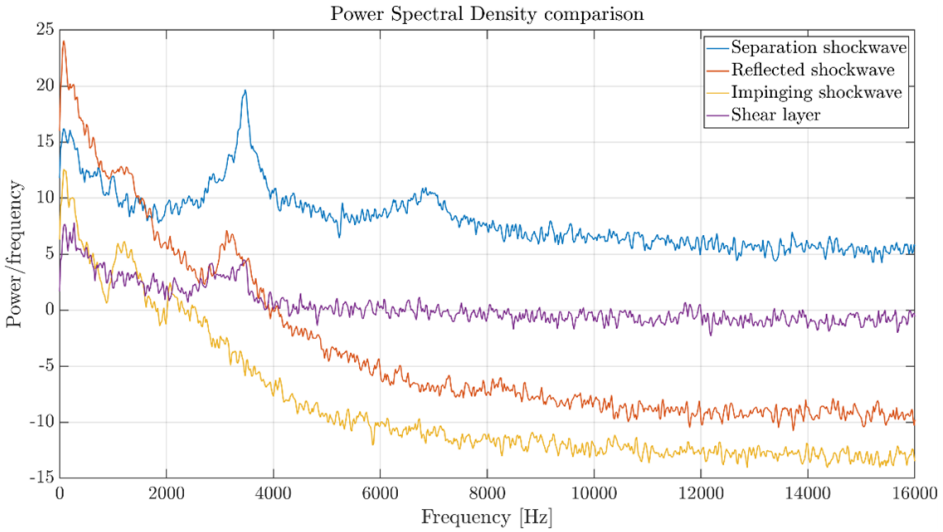

(b) frequency content for the case Ma = 2.3, p_T = 2.6 bar, 19°s.g.

Figure 5.20: Power spectral density comparison showing the effect of a slight change in Re_x – 19°shock generator

Therefore, in this test case, the Reynolds number is confirmed to be in the transitional range and the physical oscillation mechanism appears to be present, with a Mach reflection visible throughout the recording. As before, we confirm this constant Mach reflection presence by analyzing the wave angles, Figure 5.21.

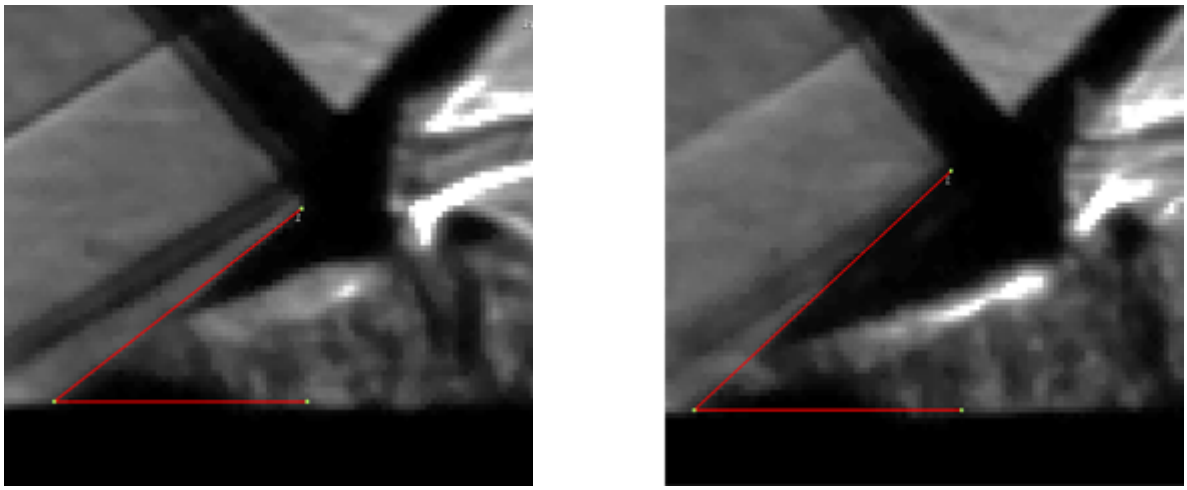

(a) min angle observed - 37.07° **(b)** max angle observed - 40.6°

Figure 5.21: Min and Max angles observed for the third case analyzed: Ma = 2.3, p_T = 2.6 bar, 19°s.g.

The observation that a Mach stem is present all throughout the interaction is confirmed by the shock polars drawn in Figure 5.22. While it is true that, in Figure 5.22a, there is an intersection between the shock polars of the shock generator and the separation bubble, they only narrowly meet; any hysteresis effect or unsteadiness of the interaction might mean that, even though theoretically this would correspond to a regular reflection, the intersection is so close that a Mach reflection may still develop.

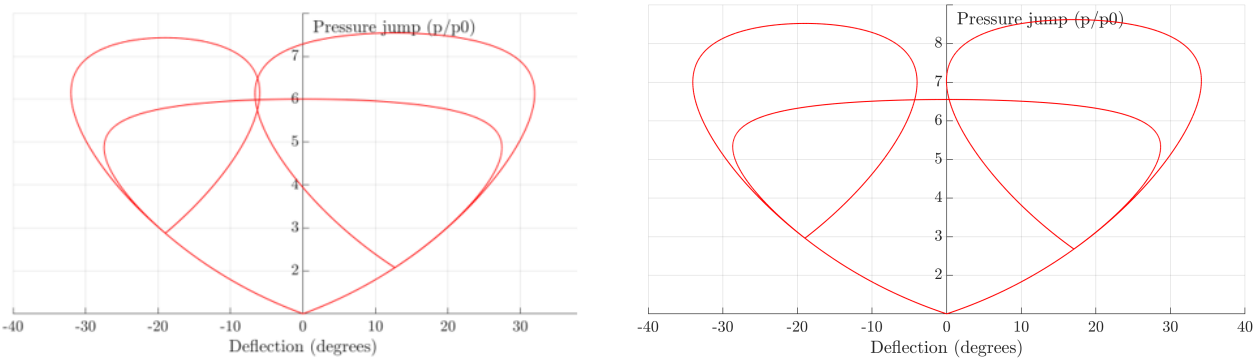

(a) min angle observed **(b)** max angle observed

Figure 5.22: Corresponding shock polars for the third case analyzed: Ma = 2.3, p_T = 2.6 bar, 19°s.g.

5.2.3.1 Exceeding the Re_x value for a transitional interaction

It can already be seen that modification in the Reynolds number can affect both the appearance of the dual domain and the physical mechanism that occurs. So far, for all cases investigated, the theoretical impingement Re_x value was presented and calculated, justifying that the interaction falls within the transitional range. In the following comparison, we take a look at two cases with high Re_x, one of which exceeds the theoretical values obtained from the PhD thesis of Giepman [16].

These two cases are Ma = 2.3, p_T = 4 bar, 19°shock generator (Figure 5.23a), with a calculated Re_x = 2.97 million (within the transitional range), and Ma = 2.3, p_T = 4.2 bar, 19°shock generator (Figure 5.23b), with a calculated Re_x = 3.3 million (very close to the turbulent range). It was previously mentioned that the values obtained by Giepman [16] for the natural flat plate can be affected by the strength of the interaction (so the interaction might stop being transitional at earlier than predicted Re_x).

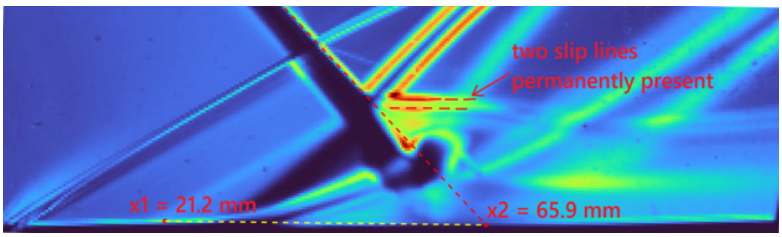

(a) Ma = 2.3, p_T = 4 bar (low oscillation observed)

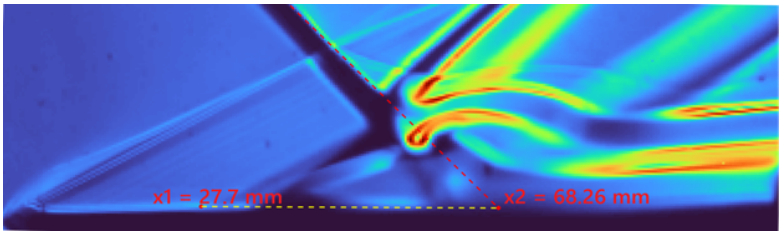

(b) Ma = 2.3, p_T = 4.2 bar (no oscillation observed)

Figure 5.23: Comparison of two cases at high Re_x - 19°shock generator

Already, from the rms figures, a shadow of the separation shockwave is seen more clearly for the case with lower Re_x (Figure 5.23a), and also, like in the previous case analyzed, two slip lines are once again highlighted, which might indicate again that there is a Mach reflection permanently present (not a dual domain). Although the point x1 was computed for the case Ma = 2.3, p_T = 4.2 by the algorithm, the appearance and the disappearance of the laminar separation shockwave is not observed as in the previous scenarios, and the upstream point that is computed might just belong to the oscillation of the turbulent separation shockwave.

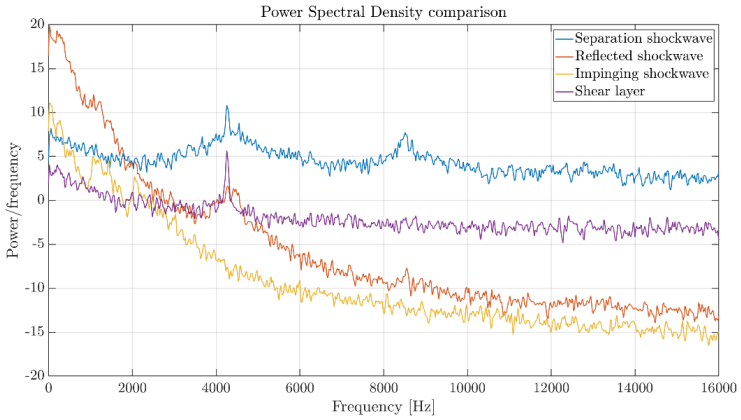

(a) frequency content for the case Ma = 2.3, p_T = 4 bar, 19°shock generator

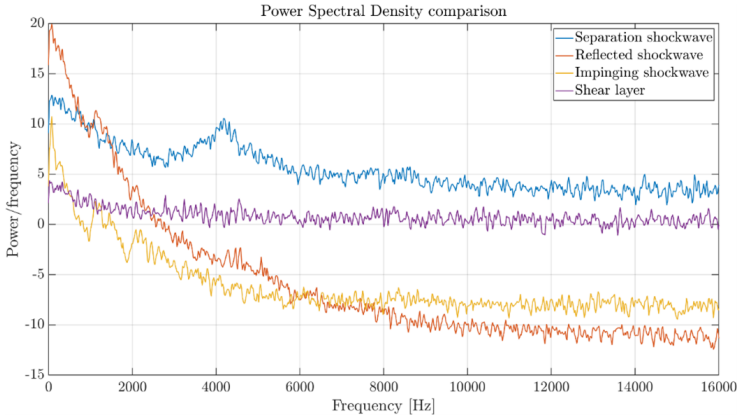

(b) frequency content for the case Ma = 2.3, p_T = 4.2 bar, 19°s.g.

Figure 5.24: Power spectral density comparison of two cases with high Re_x

In Figure 5.24, the same comparison in the frequency content which was done before is made between the two cases, showing that the test with slightly lower Re_x still shows the unsteady interaction occurring, with less clear but visible peaks (Figure 5.24a), while the test in which the Re_x appears to exceed the transitional range does not show any peaks, and especially not in the region of the separation shockwave (Figure 5.24b).

This investigation showed that the Reynolds number can influence the physical mechanism in two of the following ways: by altering the appearance of the dual domain (see the case Ma = 2.3, p_T = 2.6 bar), and by the interaction no longer being transitional in case the Reynolds number is too high (see the comparison above).

5.2.4 Influence of the dual domain appearing during the interaction

Throughout this chapter, we have discussed how various parameters influence the behavior of the interaction, classifying the observed phenomena based on several physical characteristics. The first classification, "desired oscillation", refers to cases where the laminar separation shockwave clearly travels upstream over a significant distance before collapsing, resulting in a well-defined oscillatory behavior confirmed by spectral analysis. The second category, "low oscillation amplitude", describes situations in which this oscillatory phenomenon is still present, though with reduced amplitude and less clearly defined frequency peaks. Finally, the "very low oscillation amplitude" classification covers cases in which the phenomenon is minimally observed or absent, characterized either by the lack of an upstream-traveling laminar shockwave or by negligible unsteadiness in the frequency spectrum.

In the previous subsections, when examining the effects of parameters such as Mach number, inviscid pressure jump, and Reynolds number, attention has frequently been drawn to the emergence of the so-called "dual domain"—a continuous between Mach reflection and regular reflection. Notably, it has been consistently observed that the cases which show this "desired oscillation" behavior with distinct spectral peaks include this dual domain phenomenon.

Just as in the previous cases with the 19°shock generator and the lower strength interaction at the 17°shock generator, this phenomenon of the dual domain appearing for a case with a clear unsteady oscillation is observed for a stronger interaction (shock generator) at 22°. More precisely, this is the case Ma = 2.4, p_T = 2.8 bar, 22°shock generator, depicted in Figure 5.25.

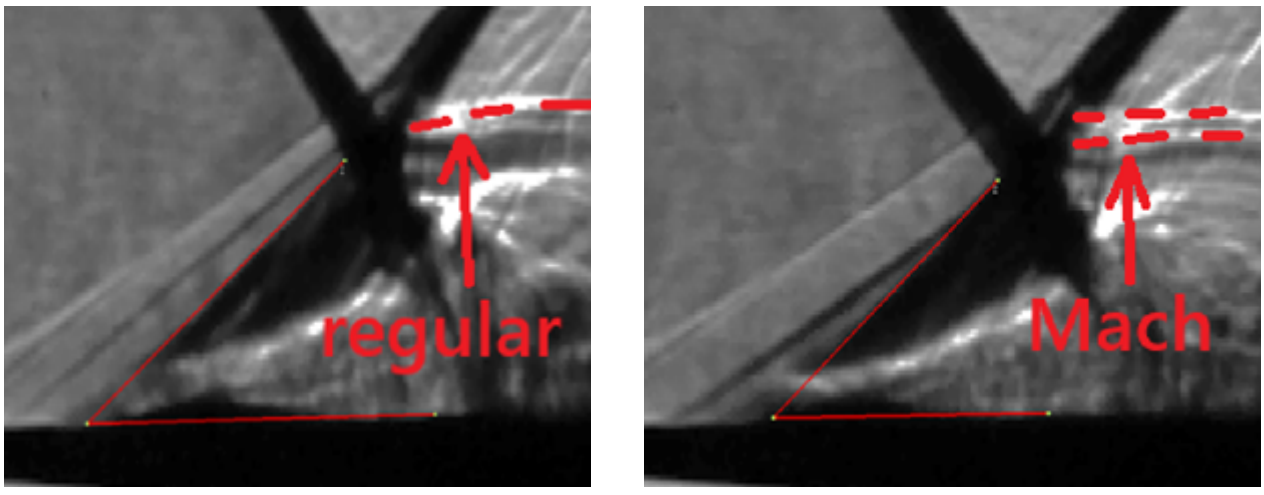

(a) min angle observed - 34.4° **(b)** max angle observed - 39.2°

Figure 5.25: Min angle and max angle showing the appearance of the dual domain for a strong interaction case – 22°shock generator

This is once again a case for which the Reynolds number falls within the transitional range, at Re_x = 1.9 million. The presence of the dual domain is once again confirmed by performing the shock polar analysis, and this is provided in Figure 5.26.

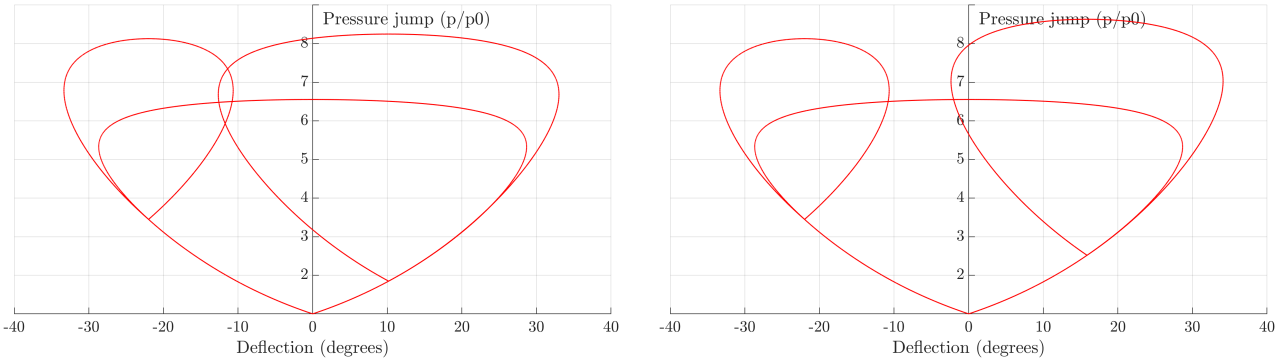

(a) min angle observed **(b)** max angle observed

Figure 5.26: Shock polar analysis for the case with a strong interaction at a 22°shock generator

This confirms the appearance of both the regular reflection through the intersection of the polars (Figure 5.26a) and the clear separation of the two (Figure 5.26a). Doing the same spectral analysis for different locations around the interaction, clear peaks show as in the previous "desired oscillation" cases at lower interaction strengths, and these peaks are observed in Figure 5.27, especially when looking at the separation shockwave, where the interaction is investigated.

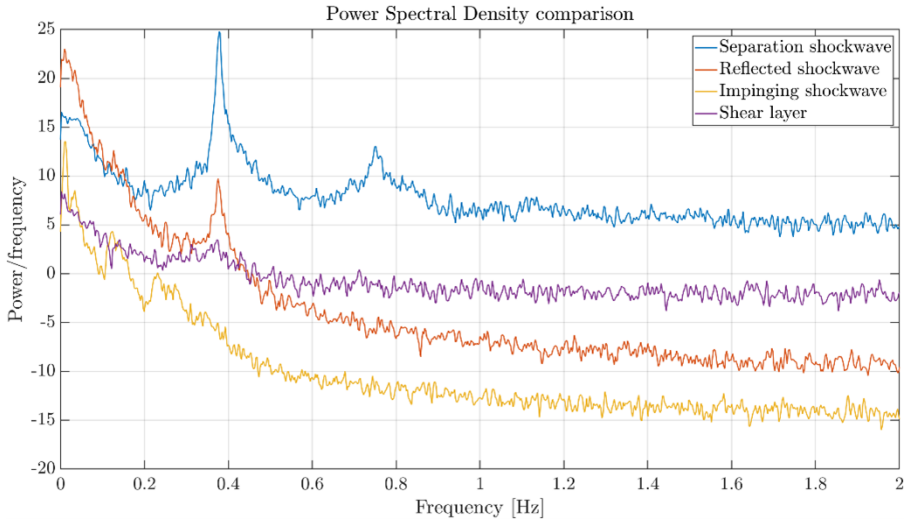

Figure 5.27: Frequency content in the interaction for a case with high shock strength - 22°shock generator

Some preliminary observations of the physical mechanism occurring can be made based on these findings:

- The appearance of the dual domain, with the continuous transition between the Mach reflection and the regular reflection, is associated with all of the cases where the desired oscillation is observed;
- When only the Mach reflection is present throughout the interaction (confirmed through the shock polars as well), there are still peaks in the frequency content showing an unsteady oscillation behavior, but their amplitude and the length of the oscillation appear less than in the cases where the dual domain is observed;
- When only a regular reflection is present throughout the interaction, the peaks in the frequency spectra do not appear clear, and the interaction does not occur as in the previous cases. All of the main aspects which were identified for the selected test cases, based on the descriptions above, are summarized in Table 5.2.

Nr.	S.G.	Ma	Re_x within transitional range (Giepman [16])?	Mach reflection observed?	Oscillation mechanism observed in the recordings and the frequency content?
1	19°	2.3	Yes	Appearing and disappearing	Desired oscillation
2	19°	2.3	Yes	Only Mach reflection	Desired oscillation faintly observed
3	19°	2.3	Yes	Only Mach reflection	Desired oscillation faintly observed
4	19°	2.3	No	Only Mach reflection	Desired oscillation not observed
5	19°	2.4	Yes	Regular reflection mostly observed	Desired oscillation very faintly observed
6	19°	2.6	Yes	Only regular reflection	Desired oscillation not observed
7	19°	2.6	Yes	Only regular reflection	Desired oscillation not observed
8	17°	2.3	Yes	Appearing and disappearing	Desired oscillation
9	17°	2.4	Yes	Regular reflection mostly observed	Desired oscillation very faintly observed
10	22°	2.4	Yes	Appearing and disappearing	Desired oscillation
11	22°	2.6	Yes	Only Mach reflection	Desired oscillation faintly observed
12	22°	2.7	Yes	Only regular reflection	Desired oscillation not observed
13	22°	2.7	Yes	Only regular reflection	Desired oscillation not observed

Table 5.2: Summary of the observations from the test cases analyzed

These observations can also be verified by analyzing all the PSD comparisons together, as in Figure 5.28 for the 19°shock generator.

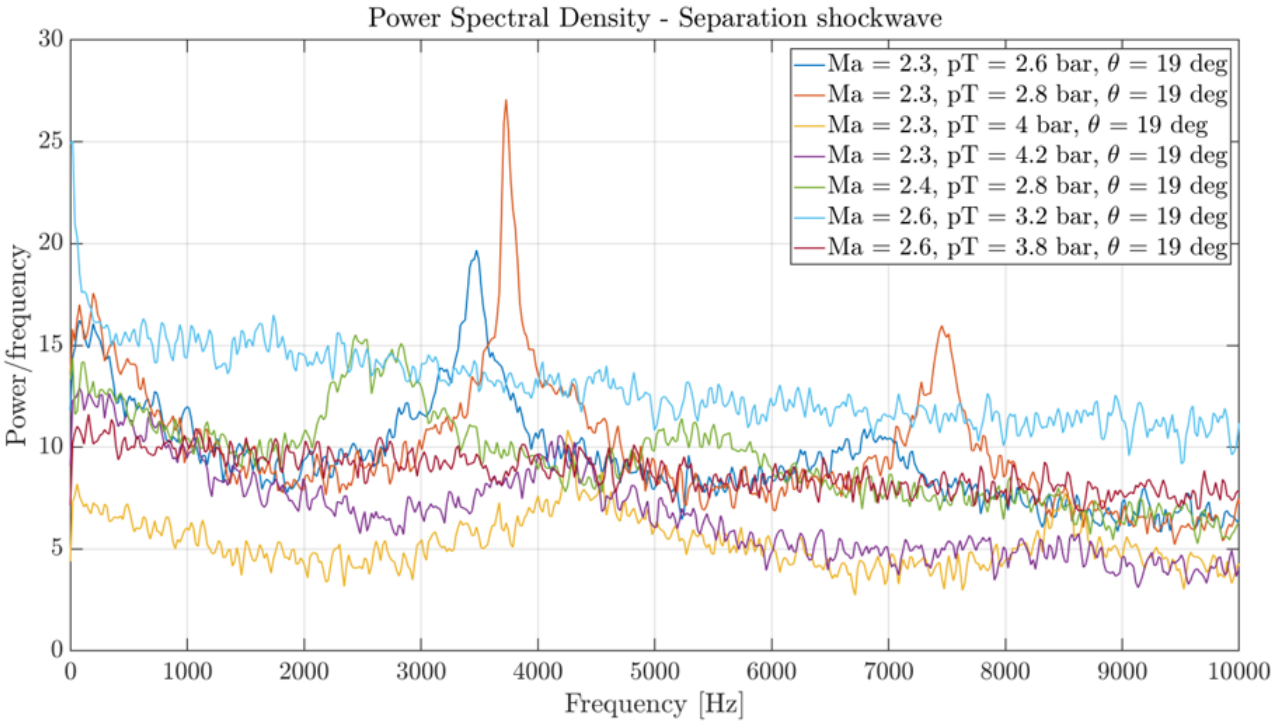

Figure 5.28: Frequency content for all test cases of the 19°shock generator

The only selected location for this comparison is the separation shockwave. By crosschecking with Table 5.2, it can be noticed that the cases with the clearest peaks correspond to the ones where we found the “desired oscillation”, the cases with lower, but still prominent peaks being the ones where the "desired oscillation is (more) faintly observed"). Finally, the cases with (almost) no peaks are the ones where the desired oscillation is “not observed”.

The same comparison can be done for the 17°shock generator test cases, Figure 5.29. Note how, by analyzing and comparing with Table 5.2, the case where the dual domain is observed (Ma = 2.3, pT = 2.6 bar) appears to have much clearer peaks and a much clearer oscillation mechanism occurring than the second case analyzed (Ma = 2.4, pT = 2.8 bar), where only a regular reflection is permanently present and where there is no distinct peak in the frequency content.

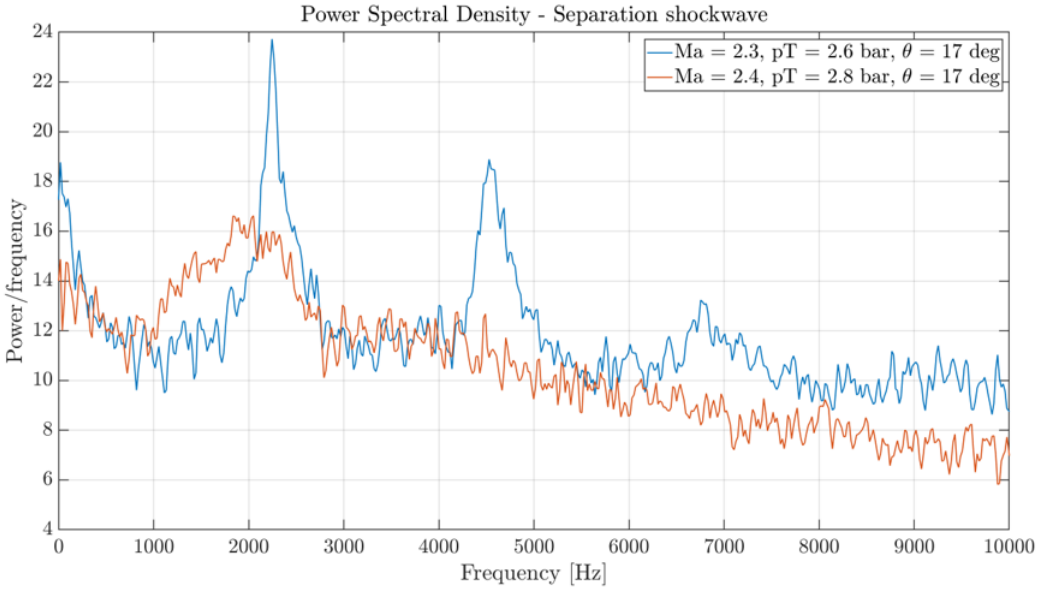

Figure 5.29: Frequency content for all test cases of the 19°shock generator

And, finally, Figure 5.30 presenting the 22°test case frequency results also shows the same conclusions: the unsteady interaction is visible for the case Ma = 2.4, p_T = 2.8 bar (for which the dual domain appears), the peaks have a lower amplitude where only a Mach reflection is permanently present (the case Ma = 2.6, p_T = 3.4 bar), and there is no distinct observation of the unsteady phenomenon for the remaining cases, where only the regular reflection appears.

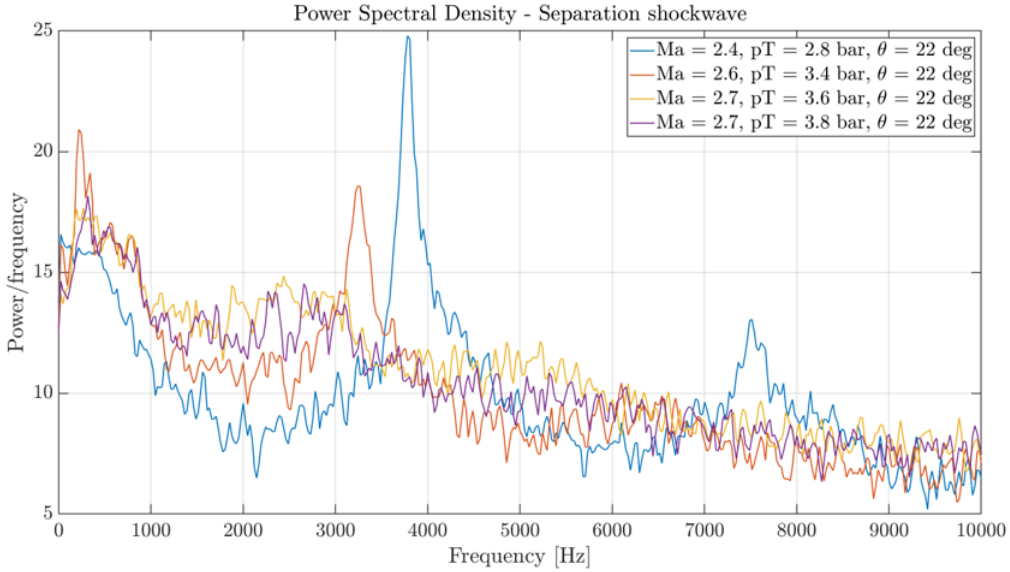

Figure 5.30: Frequency content for all test cases of the 22°shock generator

For a better visualization, the cases with no peaks are removed and the result is depicted in Figure 5.31, where the clearest peaks correspond to the cases where the Mach stem appears and disappears throughout the interaction.

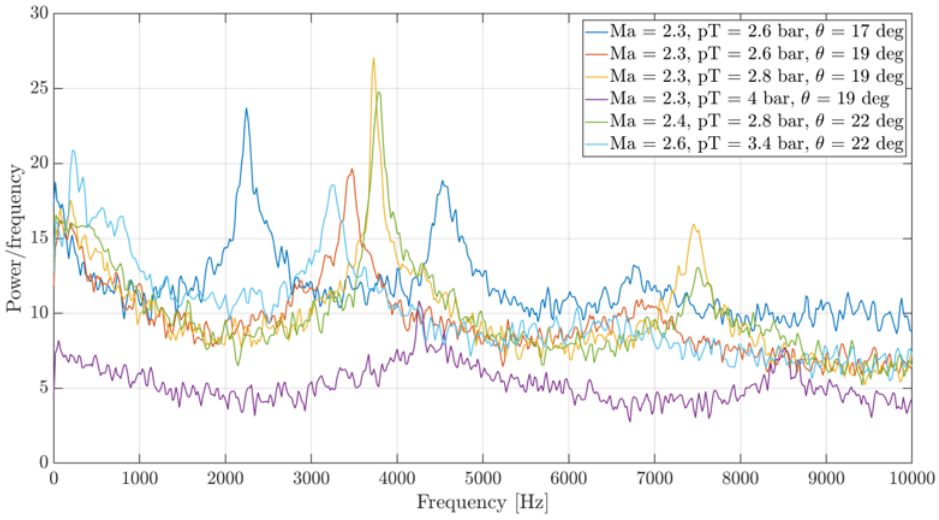

Figure 5.31: Frequency content for all "relevant" cases with no low oscillation amplitude

5.2.5 Addition of the 2D step

One of the popularly used flow control methods in aerodynamics is using an "artificial" 2D step, as described in the methodology section. The purpose of adding them was to notice how the interaction changes with different step heights and observe if- and to which extent the oscillation mechanism is dampened. In Figure 5.32, snapshots of the maximum upstream position of the laminar separation shockwave were taken (or just simply snapshots of the interaction if the laminar separation shockwave cannot be observed anymore).

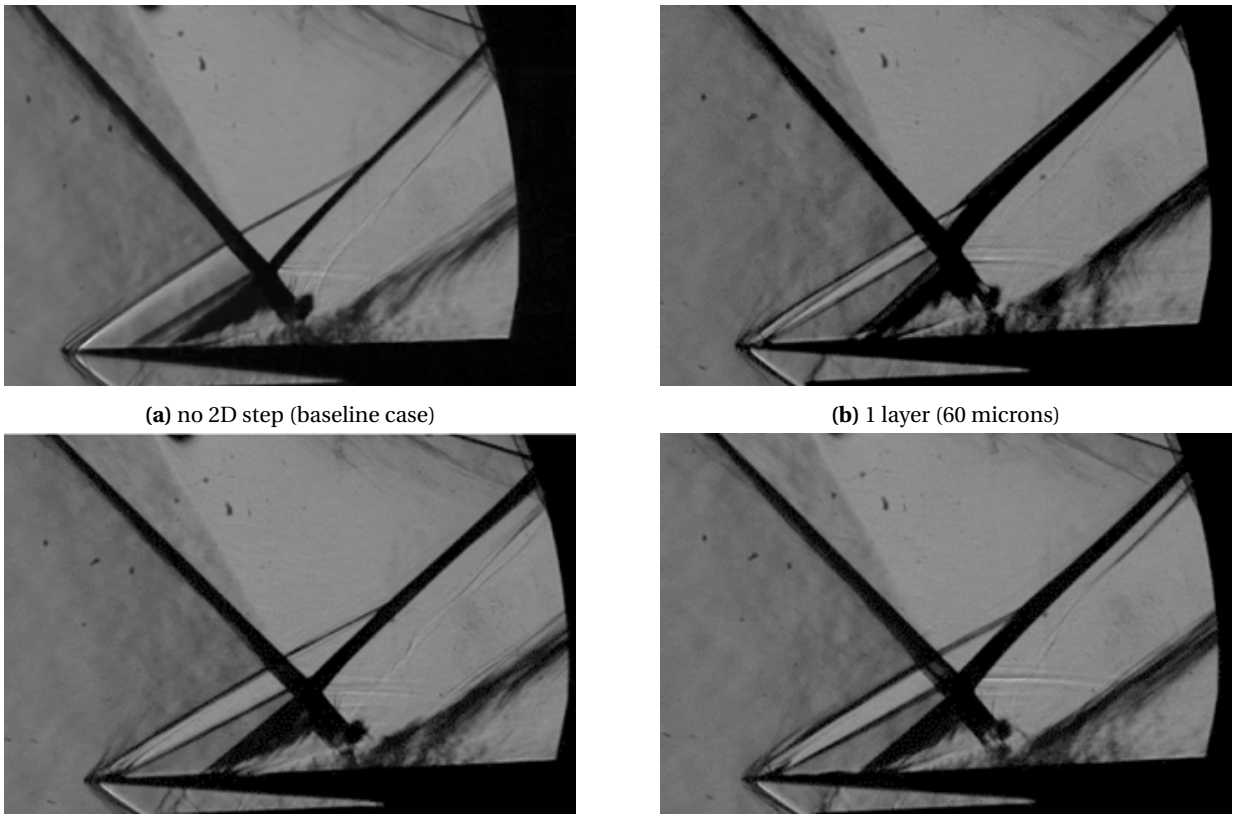

(a) no 2D step (baseline case)

(b) 1 layer (60 microns)

(c) 2 layers (120 microns)

(d) 3 layers (180 microns)

Figure 5.32: Shock travel comparison with 2D Step – reference case (Ma = 2.3, p_T = 2.8 bar, 19°s.g.)

Already, by analyzing Figure 5.32b in comparison with the case where no step is applied, it can be noticed that the interaction has significantly changed. The oscillation of the system (separation shockwave, reflected shockwave) is much less pronounced than for the "undisturbed" scenario, and there is very little travel amplitude for the separation shockwave.

As can be seen in Figure 5.32c and Figure 5.32d, this becomes even more exacerbated once more layers of the 2D step are added. It can be concluded that the addition of the 1 layer (60 microns) of 2D step was sufficient to dampen the oscillation system and deviate this phenomenon from a transitional OSBLI.

These findings are confirmed in the frequency analysis (Figure 5.33), where it can already be seen that no peaks of the oscillation frequency are noticed after adding even one layer of the 2D step.

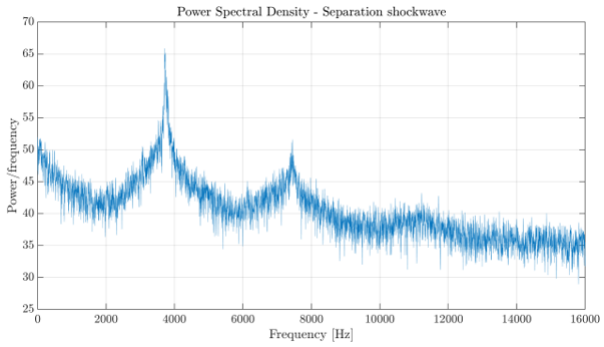

(a) no 2D step

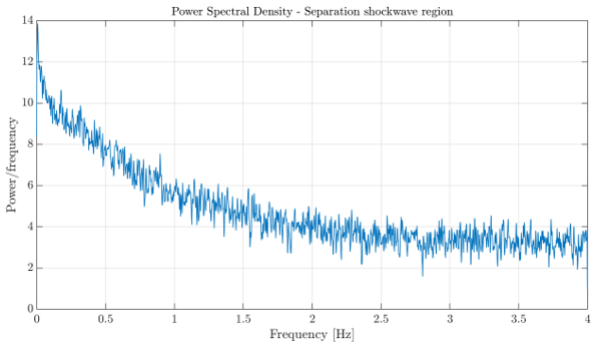

(b) 1 layer (60 microns)

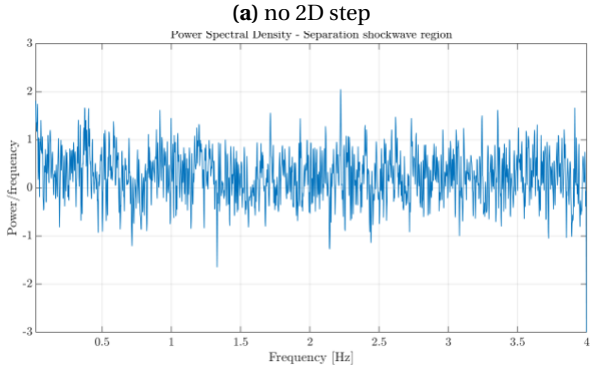

(c) 2 layers (120 microns)

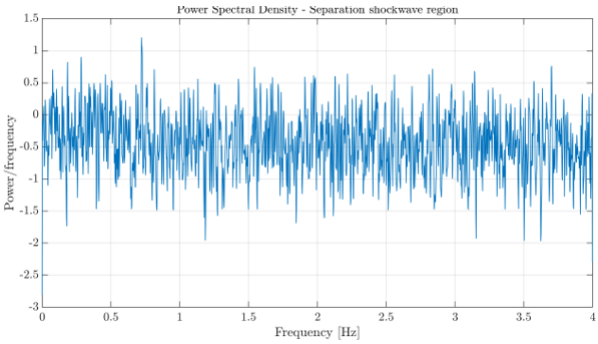

(d) 3 layers (180 microns)

Figure 5.33: Frequency content comparison with 2D Step – reference case (Ma = 2.3, p_T = 2.8 bar, 19°s.g.)

5.3 Conclusion for the analysis of the physical mechanism

After analyzing the main parameters that influence the investigated interaction, we have concluded the following:

- The parameters that can be changed during testing (the Mach number and the inviscid pressure jump, together with changing the shock generator angle which influences the strength of the interaction) can significantly change the phenomenon which occurs; even slight changes in Mach number or pressure jump altered both the how the appearance of the "dual domain" occurs and the type of oscillation that is encountered;

- The Reynolds number (through changes in the wind tunnel total pressure) also plays an important role in characterizing the state of the boundary layer, and therefore the type of interaction that occurs. It was noticed that changes in Reynolds number affect the interaction both through influencing the appearance of the dual domain, and through the fact that exceeding the calculated transitional boundary layer values led to the mechanism no longer being present (no transitional OSBLI);

- All of these parameters influence the appearance of the dual domain, which itself appears to be associated with cases where the "desired oscillation" is observed. Furthermore, for cases where only

a Mach reflection appears, the interaction still appears to happen, but not in the same clear manner as confirmed through the spectral analysis.

- Tripping the boundary layer changes the interaction completely at even low step heights (note how, even for one layer or 60 microns step height, the peaks in the interaction already appear dampened, and the amplitude of the separation shockwave is significantly affected, with almost no oscillations in the mechanism observed).

5.4 Non-dimensional analysis

The sections before focused mainly on comparing the "raw" frequency content between the different cases studied. While this is suitable in identifying some of the characteristics of the unsteadiness of the interaction and can be further used to analyze each specific case (using, for example, a PIV experiment), comparisons of raw frequency values between different experimental cases or flow conditions can be misleading due to variations in characteristic lengths and velocities.

Therefore, the use of dimensionless parameters such as the Strouhal number (St) provides a more generalized approach that can be used to compare with results from other scientific work. The Strouhal number is defined as:

$$St = \frac{fL}{U} \tag{5.2}$$

Where f is the frequency of the unsteady interaction, L is a characteristic length scale, and U is a reference velocity. Since the frequency is already identified from analyzing the Schlieren data, and the reference velocity can be extracted from the Mach number, which is known for each case, the only remaining matter is choosing the appropriate length scale.

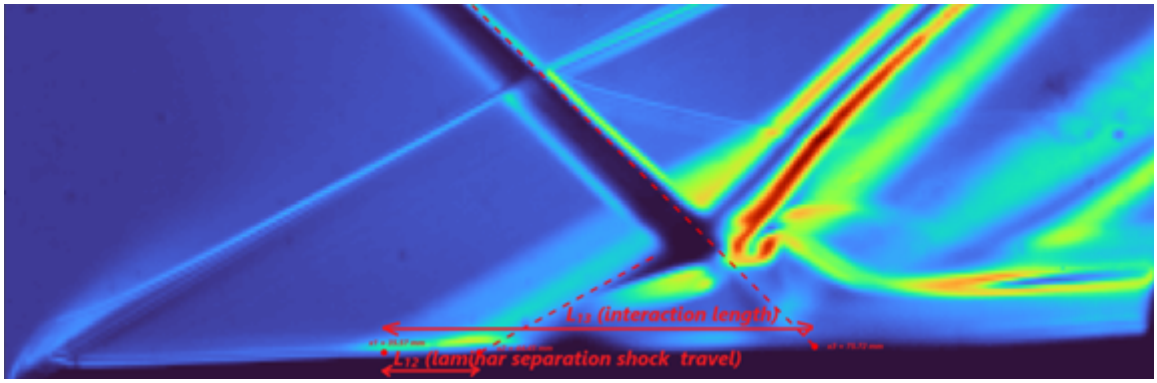

Figure 5.34: Length scales that can be used in the non-dimensional analysis

The choice of the length scales for the Strouhal comparison is depicted in Figure 5.34. There are two possible choices that were analyzed, and they represent the following:

- L_{12} – the "laminar separation shock travel", considered as the distance between the mean most upstream position of the laminar separation shockwave and the mean position from which this shockwave starts emanating
- L_{13} – the "interaction length", which is more commonly used as the reference length in the non-dimensional analysis [30], and represents the distance between the mean most upstream position of the separation shockwave and the theoretical inviscid impingement point of the oblique shockwave.

The former length was also considered to be a "relevant" length scale in the context of transitional OSBLIs in Nel et al. [9], and therefore, it is included in the analysis.

5.4.1 Non-dimensional analysis of the cases where the oscillation is observed

For the purpose of this analysis, only the cases in Table 5.2 where a so-called "desired oscillation" or cases with lower oscillation amplitudes (but still with the unsteady mechanism present) are selected for comparison. The idea is to notice whether there is a value for the Strouhal number for which these interaction collapse, even though the "raw" frequencies investigated do not match. For this comparison, the "classical" approach of using the interaction length (L_{13} in Figure 5.34) as the length variable is used. For the six cases where clear peaks are observed in the frequency content (so for which the transitional OSBLI which is investigated is noticed), Table 5.3 provides the relevant information for the nondimensional analysis, including the specific test cases, the calculated freestream velocities, lengths of the interaction, and the obtained Strouhal values.

Nr.	Total pressure [bar]	Ma	S.G.	Re_x [million]	L_{13} (length of the interaction) [mm]	U [m/s]	Dominant frequency [Hz]	St_{13} (based on the length of the interaction)
1	2.3	2.6	17°	2.22	40.15	545	4529	0.33
2	2.3	2.6	19°	2.01	46.6	545	3475	0.3
3	2.3	2.8	19°	2.06	48.45	545	3728	0.33
4	2.3	4	19°	2.97	44.7	545	4256	0.35
5	2.4	2.8	22°	1.90	50	557	3800	0.33
6	2.6	3.4	22°	2.41	58	577	3270	0.32

Table 5.3: Nondimensional comparison of all cases where the oscillation is observed

Interestingly, although the "dominant frequency" of the separation shockwave is different across the test cases, the Strouhal number comparison shows a collapse around the value of 0.33.

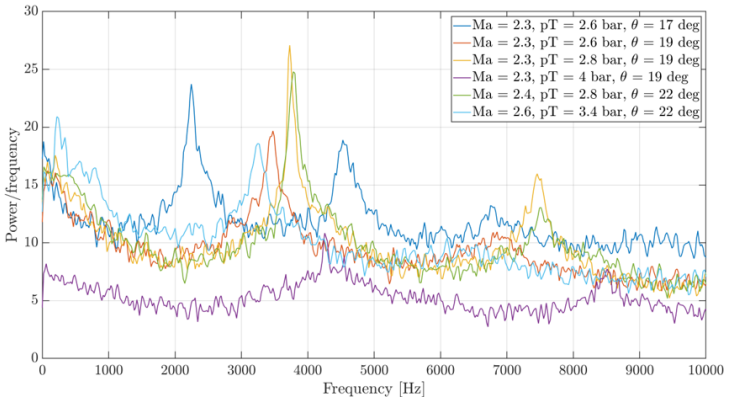

(a) "raw" frequencies depicted

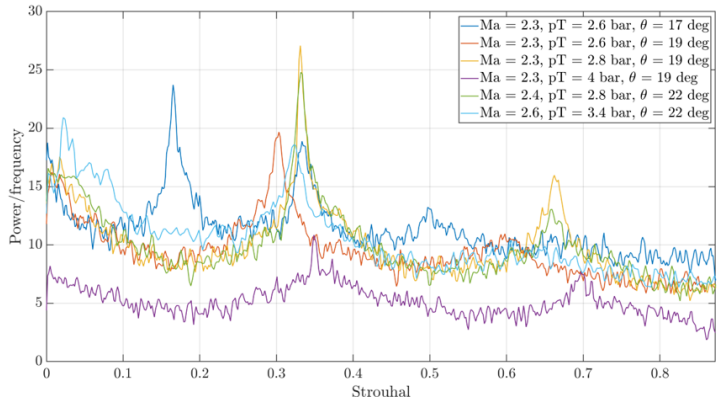

(b) Strouhal number comparison

Figure 5.35: Comparison between the raw frequency results and the nondimensional analysis for the cases where the oscillation is observed

What is even more noteworthy is that it is precisely the three test cases where the "desired oscillation", with the higher amplitude and unsteadiness, which have the exact same Strouhal number of 0.33. This comparison is visually observed in Figure 5.35: while the raw frequencies for the cases are more "scattered", the figure for the Strouhal number comparison (Figure 5.35b) shows the peaks in the graphs for the selected cases to collapse around the value of 0.33.

This provides a strong starting point for further investigation into how transitional OSBLIs of this unsteady nature behave. Future work should explore whether this phenomenon persists across a broader range of test conditions and configurations, potentially establishing a fundamental scaling parameter for characterizing the unsteady shockwave dynamics in laminar-to-turbulent transitional regimes. Additionally, validating whether other configurations and geometries exhibit similar collapses around this Strouhal number could significantly enhance predictive models, aiding in the design of systems sensitive to shockwave-induced instabilities.

5.4.2 Reynolds number effect on the interaction geometry and unsteadiness

For this comparison, only the cases where a "clear oscillation mechanism" was present and where only one parameter changed, so that its influence could be analyzed. The selected test matrix and results (Table 5.1) allowed for a Reynolds number analysis. These were cases where the inviscid pressure jump remained the same (Mach number and shock generator angle identical), but where the total pressure (and hence the Reynolds number) varied.

The selected test cases are presented in Table 5.4. They all correspond to the same Mach number (Ma = 2.3), shock generator angle (19°), and inviscid pressure jump ($p2/p1$ = 2.878), and they are presented in increasing Reynolds number value.

Nr.	p_T **[bar]**	Re_x **[million]**	L_{13} **(interaction length) [mm]**	L_{12} **(laminar sep. bubble length) [mm]**	**U [m/s]**	**Dominant frequency [Hz]**	St_{13}	St_{12}
1	2.6	2.01	46.6	11.4	545	3475	0.3	0.073
2	2.8	2.06	48.45	10.34	545	3728	0.33	0.07
3	4.0	2.97	44.7	8.54	545	4256	0.35	0.067

Table 5.4: Strouhal number comparison

The hypothesis made was that, for cases where the oscillation mechanism of interest was present, an increase in Reynolds number would also lead to an increase in the frequency of the oscillation and a decrease of the laminar separation bubble amplitude. This assumption was made based on the fact that a higher Reynolds number would mean that the boundary layer would transition quicker at the same Mach and shock strength conditions, and therefore the amplitude over which the shock travels would decrease, and the frequency over which it would pass would consequently increase.

This is confirmed in Table 5.4, as the length of the laminar separation bubble decreases with Reynolds number, and the dominant frequency identified increases. Interestingly, however, the length of the interaction (L_{13}) is the highest for the "baseline" case, but this is also where the "clearest" peaks of the unsteadiness were observed. These findings are depicted in Figure 5.36, graphically showing an increase in the interaction length when the oscillation becomes more unsteady (the middle point corresponds to the scenario of the "desired oscillation", with the clearer frequency peaks), while the general effect of the Reynolds number is to lead to a lower amplitude length of the separation shockwave and the interaction once the unsteady OSBLI is no longer observed.

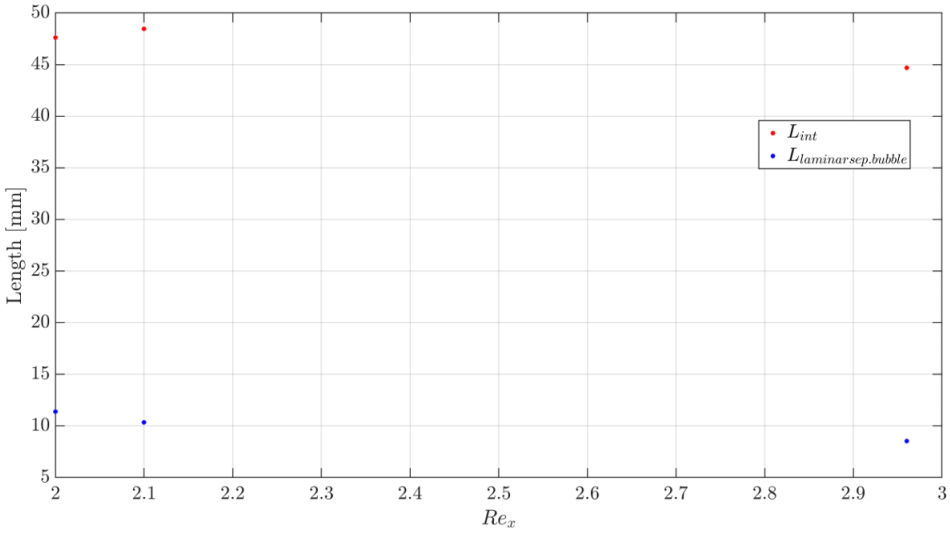

Figure 5.36: Changes in lengths with Re_x

The results in Table 5.4 are also confirmed by the Strouhal number comparison, which is depicted in Figure 5.37 for the nondimensionalization done with the "classical" length of the interaction, L_{13}. With an increase in Reynolds number, the Strouhal number for the interaction also increases, just as in the case of the "raw" frequency, which again indicates that the interaction is dominated by higher-frequency fluctuations relative to the characteristic flow velocity and geometry.

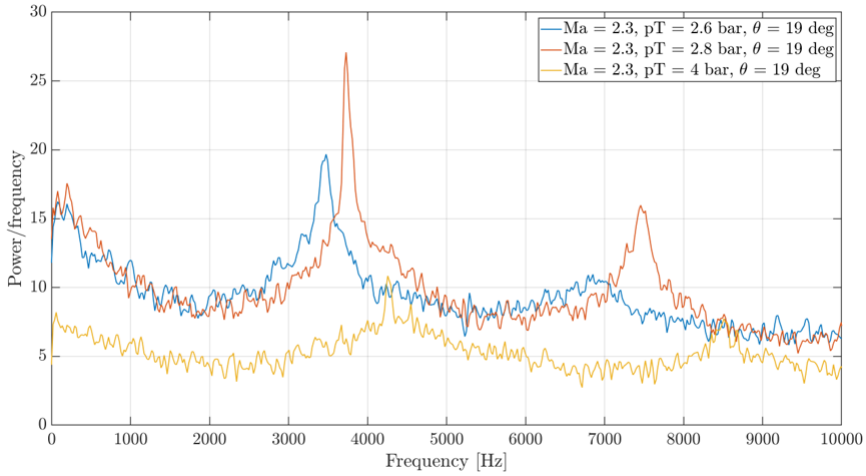

(a) "raw" frequencies depicted

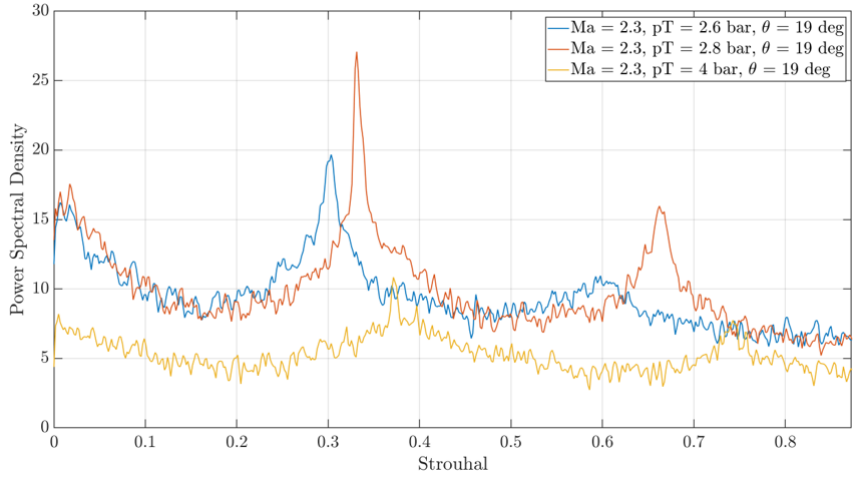

(b) Strouhal number comparison

Figure 5.37: Comparison between the raw frequency results and the nondimensional analysis – Reynolds number effect

When observing the increasing Strouhal numbers, one can interpret these findings as the interaction evolving faster in time, which is the assumption that was made based on the increase in Reynolds number being associated with a faster transition and collapse of the laminar separation bubble.

5.4.3 Conclusions of the non-dimensional analysis

A nondimensional analysis was conducted by comparing the Strouhal numbers of cases where the transitional OSBLI mechanism was most prominently observed (classification explained in Table 5.1 and Table 5.2). Cases characterized by low oscillation amplitudes or unclear frequency peaks were excluded to ensure the analysis focused solely on the relevant tests. The analysis of the selected cases revealed that, despite variations in the raw frequencies measured across different conditions, nondimensionalization using the interaction length—previously established as an appropriate scaling parameter for OSBLI phenomena—resulted in a collapse around a preferred Strouhal number of approximately 0.33. Particularly noteworthy was the consistency of Strouhal numbers among cases exhibiting the "desired oscillation" phenomenon, characterized by pronounced frequency peaks and clearly identifiable mechanisms during the experiments. Furthermore, these cases consistently featured the dual-domain behavior described earlier. Although slight deviations were observed in the other cases, the Strouhal numbers also showed a deviation towards this value.

In examining the influence of Reynolds number, we revealed clear trends, including an increase in both the raw frequency and the corresponding Strouhal number. Furthermore, a reduction in the amplitude of the laminar separation shockwave traveling upstream was observed. These observations align well with theoretical expectations, confirming the hypothesis that higher Reynolds numbers promote faster transition, resulting in reduced upstream travel distances before the shockwave collapses and, consequently, higher frequencies at specific positions within the interaction region.

Chapter 6

Conclusions and Recommendations

6.1 Conclusions

The present Master's thesis successfully addressed the primary and sub-research questions outlined at the conclusion of Chapter 2. The primary research question asked: *"What are the main parameters that can be changed which drive the low-frequency unsteadiness in the massively separated transitional oblique shock boundary layer interaction (OSBLI)?"* The investigation clearly demonstrated that the Mach number (Ma), Reynolds number (Re_x), inviscid pressure jump, and the interdependent dual domain which appeared dictate the low-frequency shock oscillation mechanism. This conclusion is strongly supported by frequency analyses and shock polar interpretations presented throughout the thesis.

Regarding the sub-questions, the results were as follows:

Firstly, the experiments examined whether the formation and periodic disappearance of a Mach stem constitutes a necessary condition for unsteadiness. The findings revealed that the presence and intermittent disappearance of the Mach stem were indeed strongly correlated with the observed low-frequency instabilities. However, while the correlation was clear, this research did not conclusively prove that the Mach stem dynamics alone were both necessary and sufficient conditions to induce unsteadiness. Future studies must further investigate this correlation to establish a more definitive theoretical understanding.

Secondly, the Reynolds number range calculated at the theoretical shock impingement point under "natural boundary layer" scenarios was validated against the transitional regime identified by Giepman [16]. The results confirmed that this specific Reynolds number regime accurately indicates laminar separation followed by rapid transition, and also influences the observed unsteadiness through significant changes in the oscillation amplitude and frequency.

Thirdly, the effect of flow control methods (more specifically, the implementation of 2D steps to artificially trip the boundary layer) was examined. The results demonstrated that these control measures substantially reduce the shock oscillation amplitude, even at very low step heights (as small as 60 microns). This outcome was supported by both Schlieren visualization techniques and the frequency analyses.

Finally, variations in relevant parameters such as the impingement point Reynolds number (Re_x), the Mach number (Ma), and the inviscid pressure jump were analyzed to determine their impact on the frequency content and the spatial extent of the SBLI. The non-dimensional analysis revealed that the Strouhal number (St) consistently converged around a value of approximately 0.33, indicating a unified scaling behavior across the investigated cases. Moreover, increasing the Reynolds number under similar conditions consistently resulted in lower amplitudes of the laminar separation shock and increased oscillation frequencies, as was expected. Although isolating one single parameter proved challenging due to their mutual dependence, each parameter's influence was delineated and quantified.

In conclusion, this Master's thesis strongly confirms the assumptions underlying this thesis, having used robust and carefully analyzed experimental data. It establishes a solid foundational understanding of transitional, highly separated OSBLIs and provides valuable insights into flow control methodologies.

Nonetheless, further theoretical and experimental research is essential to verify the broader applicability of these findings, particularly in transonic OSBLI scenarios.

6.2 Recommendations

Based on this, several recommendations for future research have emerged from this study. Firstly, overcoming physical and aerodynamic constraints (such as wind tunnel unstart) would enable comparisons at similar Reynolds numbers to also thoroughly examine the effects of shock strength and associated inviscid pressure rise. Additionally, developing an automated shock tracking algorithm would streamline the process, significantly reducing the time and potential errors associated with manual angle measurements.

Given that small variations in the testing conditions sometimes resulted in very different interactions, predictive methods or models of the interaction type and separation bubble characteristics would greatly improve the experimental planning and interpretation.

Addressing the three-dimensional interference effects, particularly those arising from expansion waves generated at the shoulder of the shock generator, would further refine the experimental accuracy. Performing Particle Image Velocimetry (PIV) and oil flow visualizations could complement existing Schlieren imaging techniques by precisely characterizing boundary layer thickness and accurately identifying the separation and the reattachment locations of the boundary layer.

It is also advisable to investigate even lower two-dimensional step heights, considering their effectiveness in dampening interactions observed in the current thesis. Lastly, complementary Computational Fluid Dynamics (CFD) simulations would provide valuable insights, enabling a more comprehensive understanding of the underlying physical mechanisms and validating the experimental results.

References

[1] H. Babinsky and J. Harvey, *Shock Wave-Boundary-Layer Interactions*. Cambridge University Press, 2011.

[2] J. D. Watts, "Flight experience with shock impingement and interference heating on the x-15-2 research airplane," NASA, Tech. Rep. TM X-1669, 1968.

[3] P. Doerffer, P. Flaszynski, J.-P. Dussauge, *et al.*, *Transition Location Effect on Shock Wave Boundary Layer Interaction. Experimental and Numerical Findings from the TFAST Project*. Springer, 2021.

[4] L. Surber and J. Tinapple, "Inlet flow control technology: Learning from history, reinventing the future," in *50th AIAA Aerospace Sciences Meeting*, 2012, p. 12. DOI: https://doi.org/10.2514/6.2012-12.

[5] N. Webb, C. Clifford, and M. Samimy, "Control of oblique shock wave-boundary layer interactions using plasma actuators," *Experimental Fluids*, vol. 54, p. 1545, 2013. DOI: https://doi.org/10.1007/s00348-013-1545-z.

[6] N. Cumpsty, *Compressor Aerodynamics, Volume 10*. Krieger Publishing Company, 2004.

[7] P. Nel, A.-M. Schreyer, F. Schrijer, B. van Oudheusden, C. Janke, and M. Swoboda, "Research configuration to study shock oscillation mechanisms," Manuscript submitted for publication, 2024.

[8] J. Denton, "The effects of lean and sweep on transonic fan performance: A computational study," Cambridge University Engineering Department, Cambridge, Tech. Rep., 2002.

[9] P. L. Nel, A.-M. Schreyer, F. F. Schrijer, *et al.*, "Shock oscillation mechanism of highly separated transitional shock-wave/boundary-layer interactions," Manuscript submitted for publication, 2024.

[10] P. L. Nel, C. Janke, I. Vasilopoulos, *et al.*, "Effect of transition on self-sustained shock oscillations in highly loaded transonic rotors," *AIAA Journal*, 2024. DOI: https://doi.org/10.2514/1.J063378.

[11] J. Poggie, N. J. Bisek, R. L. Kimmel, and S. Stanfield, "Spectral characteristics of separation shock unsteadiness," *AIAA Journal*, vol. 53, no. 1, pp. 200–214, 2015. DOI: https://doi.org/10.2514/1.J053029.

[12] M. Waindim, L. Agostini, L. Larchêveque, and M. Adler, "Dynamics of separation bubble dilation and collapse in shock wave/turbulent boundary layer interactions," *Shock Waves*, vol. 30, no. 1, pp. 63–75, 2020. DOI: https://doi.org/10.1007/S00193-019-00918-Y.

[13] H. Schlichting and K. Gersten, *Boundary-Layer Theory, 9th edition*. Springer-Verlag Berlin Heidelberg, 2017.

[14] F. White, *Viscous Fluid Flow, 2nd Edition*. McGraw Hill Inc., 1991.

[15] R. Vos and S. Farokhi, *Introduction to Transonic Aerodynamics. Fluid Mechanics and Its Applications*. Dordrecht: Springer, 2015.

[16] R. Giepman, "Flow control for oblique shock wave reflections," Ph.D. dissertation, Technical University of Delft, 2016.

[17] D. Chapman, D. Kuehn, and H. Larson, "Investigation of separated flows in supersonic and subsonic streams with emphasis on the effect of transition," NACA, Tech. Rep. Report No. 1356, 1957.

[18] J. Erdos and A. Pallone, "Shock-boundary layer interaction and flow separations," in *Proceedings of the 1962 Heat Transfer and Fluid Mechanics Institute*, 1963.

[19] D. Dolling, "Fifty years of shock-wave/boundary-layer interaction research: What next?" *AIAA Journal*, vol. 39, no. 8, 2001. DOI: https://doi.org/10.2514/2.1476.

[20] J. Andreopoulos and K. Muck, "Some new aspects of the shock-wave/boundary-layer interaction in compression-ramp flows," *Journal of Fluid Mechanics*, pp. 405–428, 1987. DOI: https://doi.org/10.1017/S0022112087001873.

[21] B. Ganapathisubramani, N. Clemens, and D. Dolling, "Low-frequency dynamics of shock-induced separation in a compression ramp interaction," *Journal of Fluid Mechanics*, vol. 636, pp. 397–425, 2009. DOI: https://doi.org/10.1017/S0022112009007952.

[22] S. Beresh, J. Henfling, R. Spillers, and B. O. M. Pruett, "Very-large-scale coherent structures in the wall pressure field beneath a supersonic turbulent boundary layer," in *49th AIAA Aerospace Sciences Meeting*, vol. 25, 2013. DOI: https://doi.org/10.1063/1.4820818.

[23] S. Piponniau, J. Dussauge, J. Debieve, and P. Dupont, "A simple model for low-frequency unsteadiness in shock-induced separation," *Journal of Fluid Mechanics*, vol. 629, pp. 87–108, 2009. DOI: https://doi.org/10.1017/S0022112009006417.

[24] N. Sandham, E. Schülein, A. Wagner, S. Willems, and J. Steelant, "Transitional shock-wave/boundary-layer interactions in hypersonic flow," *Journal of Fluid Mechanics*, vol. 752, pp. 349–382, 2014. DOI: 10.1017.

[25] Z. Murphree, K. Yuceil, N. Clemens, and D. Dolling, "Experimental studies of transitional boundary layer shock wave interactions," in *45th AIAA Aerospace Sciences Meeting and Exhibit*, 2006. DOI: https://doi.org/10.2514/6.2007-1139.

[26] V. Shinde, J. McNamara, and D. Gaitonde, "Control of transitional shock wave boundary layer interaction using structurally constrained surface morphing," *Aerospace Science and Technology*, vol. 96, 2020. DOI: https://doi.org/10.1016/j.ast.2019.105545.

[27] V. Shinde, J. McNamara, D. Gaitonde, and C. Barnes, "Transitional shock wave boundary layer interaction over a flexible panel," *Journal of Fluids and Structures*, vol. 90, pp. 263–285, 2019. DOI: https://doi.org/10.1016/j.jfluidstructs.2019.07.007.

[28] V. Pasquariello, S. Hickel, and N. Adams, "Unsteady effects of strong shock-wave/boundary-layer interaction at high reynolds number," *Journal of Fluid Mechanics*, vol. 823, pp. 617–657, 2017. DOI: https://doi.org/10.1017/jfm.2017.308.

[29] Y. Zhuang, H.-J. Tan, X. Li, F.-J. Sheng, and Y.-C. Zhang, "Görtler-like vortices in an impinging shock wave/turbulent boundary layer interaction flow," *Physics of Fluids*, vol. 30, no. 6, 2018. DOI: https://doi.org/10.1063/1.5034242.

[30] J.-P. Dussauge, P. Dupont, and J.-F. Debieve, "Unsteadiness in shock wave boundary layer interactions with separation," *Aerospace Science and Technology*, vol. 10, pp. 85–91, 2006. DOI: https://doi.org/10.1016/j.ast.2005.09.006.

[31] P. Dupont, C. Haddad, and J. Debieve, "Space and time organization in a shock-induced separated boundary layer," *Journal of Fluid Mechanics*, pp. 255–277, 2006. DOI: https://doi.org/10.1017/S0022112006000267.

[32] H. Babinsky, Y. Li, and C. Ford, "Microramp control of supersonic oblique shock-wave/boundary-layer interactions," *AIAA Journal*, vol. 47, no. 3, pp. 668–675, 2009. DOI: https://doi.org/10.2514/1.38022.

[33] B. H. Anderson, J. Tinapple, and L. Surber, "Optimal control of shock wave turbulent boundary layer interactions using micro-array actuation," in *3rd Flow Control Conference AIAA*, 2006. DOI: https://doi.org/10.2514/6.2006-3197.

[34] G. Ben-Dor, O. Igra, and T. Elperin, *Handbook of Shock Waves, Three Volume Set*. Beer Sheva: Elsevier Science, 2001.

[35] J. D. Anderson, *Fundamentals of Aerodynamics*. New York: McGraw Hill Education, 2017.

[36] V. Pasquariello, M. Grilli, S. Hickel, and N. Adams, "Large-eddy simulation of passive shock-wave/boundary-layer interaction control," *International Journal of Heat and Fluid Flow*, vol. 49, pp. 116–127, 2014. DOI: http://dx.doi.org/10.1016/j.ijheatfluidflow.2014.04.005.

[37] A. Joseph, P. Flaszynski, P. Doerffer, and M. Piotrowwicz, "Low reynolds number effect on highly loaded compressor stator cascade," in *15th European Conference on Turbomachinery Fluid Dynamics Thermodynamics*, 2023. DOI: https://doi.org/10.29008/ETC2023-239.

[38] M. Lugrin, S. Beneddine, E. Garnier, and R. Bur, "Multi-scale study of the transitional shock-wave boundary layer interaction in hypersonic flow," *Theoretical and Computational Fluid Dynamics*, vol. 36, pp. 277–302, 2021. DOI: https://doi.org/10.1007/S00162-021-00595-7.

[39] J. Bibin, V. Kulkarni, and G. Natarajan, "Shock wave boundary layer interactions in hypersonic flows," *International Journal of Heat and Mass Transfer*, vol. 70, pp. 81–90, 2014. DOI: https://doi.org/10.1016/j.ijheatmasstransfer.2013.10.072.

[40] F. Schrijer, "Experimental investigation of re-entry aerodynamic phenomena," Ph.D. dissertation, Delft University of Technology, 2010.

[41] J. S. Patterson, "Experimental study of shock-shock interactions with variable inflow mach number," M.S. thesis, Delft University of Technology, 2019.

[42] A. Pope and L. Kennith, *High-speed wind tunnel testing*. John Wiley
Sons Inc., 1965.

[43] T. Missing and H. Babinsky, "Corner effects on oblique shock wave boundary layer interactions in rectangular channels," in *AIAA SCITECH 2023 Forum*, 2023. DOI: https://doi.org/10.2514/6.2023-0650.

[44] G. Settles, *Schlieren and Shadowgraph Techniques: Visualizing Phenomena in Transparent Media*. Berlin: Springer, 2001.

[45] G. Eslinga, B. van Oudheusden, F. Scarano, and D. Watt, "Assessment and application of quantitative schlieren methods: Calibrated color schlieren and background oriented schlieren," *Experiments in Fluids*, vol. 36, pp. 309–325, 2004. DOI: https://doi.org/10.1007/s00348-003-0724-8.

[46] S. W. Smith, *The scientist and engineer's guide to digital signal processing*. California Technical Publishing, 1997, [Online]. Available: https://www.dspguide.com/.

[47] P. Welch, "The use of fast fourier transforms for the estimation of power spectra: A method based on time averaging over short modified periodograms," *IEEE*, vol. 15, no. 2, pp. 70–73, 1967. DOI: https://doi.org/10.1109/TAU.1967.1161901.